Universidade Federal de Juiz de Fora

Programa de Pós-Graduação em Engenharia Elétrica

Vinicius Athouguia Gama

IMPROVING STATE-OF-HEALTH PREDICTION OF LI-ION BATTERIES: A HYBRID SEMI-EMPIRICAL GAUSSIAN PROCESS REGRESSION APPROACH

Master's Dissertation

Juiz de Fora

2026

Vinicius Athouguia Gama

IMPROVING STATE-OF-HEALTH PREDICTION OF LI-ION BATTERIES: A HYBRID SEMI-EMPIRICAL GAUSSIAN PROCESS REGRESSION APPROACH

Master's dissertation submitted to the Graduate Program in Electrical Engineering, concentration area: Electronic Systems, of the Faculty of Engineering, Federal University of Juiz de Fora, as partial fulfillment of the requirements for the degree of Master.

Advisor: Janaína Gonçalves de Oliveira, Ph.D.

Co-advisor: Leonardo Willer de Oliveira, D.Sc.

Juiz de Fora

2026

Ficha catalográfica elaborada através do programa de geração automática da Biblioteca Universitária da UFJF, com os dados fornecidos pelo(a) autor(a)

Gama, Vinicius Athouguia.
IMPROVING STATE-OF-HEALTH PREDICTION OF LI-ION BATTERIES: A HYBRID SEMI-EMPIRICAL GAUSSIAN PROCESS REGRESSION APPROACH / Vinicius Athouguia Gama. – 2026.
97 f. : il.

Advisor: Janaína Gonçalves de Oliveira, Ph.D.
Co-advisor: Leonardo Willer de Oliveira, D.Sc.
Master's Dissertation – Universidade Federal de Juiz de Fora, Programa de Pós-Graduação em Engenharia Elétrica, 2026.

1. Lithium-ion Battery. 2. Battery Energy Storage Systems. 3. Aging-Aware Operation. 4. Degradation Modeling. 5. Gaussian Process Regression. 6. Machine Learning. 7. Semi-Empirical Model. de Oliveira, Janaína Gonçalves, advisor. II. de Oliveira, Leonardo Willer, co-advisor. III. Title.

Vinicius Athouguia Gama

Improving State-of-Health Prediction of Li-Ion Batteries: A Hybrid Semi-Empirical Gaussian Process Regression Approach

Dissertation submitted to the Graduate Program in Electrical Engineering of the Federal University of Juiz de Fora as a partial requirement for obtaining a Master's degree in Electrical Engineering.
Concentration area: Electronic Systems

Approved on 29 of April of 2026.

EXAMINING BOARD

Profa. Dra. Janaína Gonçalves de Oliveira – Academic Advisor
Federal University of Juiz de Fora

Prof. Dr. Leonardo Willer de Oliveira – Academic Co-Advisor
Federal University of Juiz de Fora

Prof. Dr. João Alberto Passos Filho
Federal University of Juiz de Fora

Prof. Dr. Rodrigo Cassio de Barros
Federal University of Ouro Preto

Juiz de Fora, 04/29/2026.

de 2020.

A autenticidade deste documento pode ser conferida no Portal do SEI-Ufjf (www2.ufjf.br/SEI) através do ícone Conferência de Documentos, informando o código verificador **2942699** e o código CRC **7BE047A6**.

To my family and my girlfriend, Laís,
whose love, patience, and support
made this journey possible.
This is for you.

ACKNOWLEDGMENTS

First and foremost, I would like to express my deepest gratitude to my advisor, Prof. Dr. Janaína Gonçalves de Oliveira, and my co-advisor, Prof. Dr. Leonardo Willer de Oliveira. Their guidance, continuous support, patience, and invaluable insights were fundamental not only to the development of this research but also to my growth as a researcher.

I also extend my sincere thanks to all the professors of the Graduate Program in Electrical Engineering for their dedication to teaching and for providing a solid academic foundation throughout my master's studies. The knowledge shared in the classroom was instrumental in shaping the theoretical framework of this dissertation.

Furthermore, I am highly indebted to the Graduate Program in Electrical Engineering (Programa de Pós-Graduação em Engenharia Elétrica - PPEE) and the Federal University of Juiz de Fora (Universidade Federal de Juiz de Fora - UFJF) for providing the excellent institutional support and the necessary infrastructure to conduct this work.

"Nothing in life is to be feared; it is only to be understood."

(Marie Curie)

RESUMO

A modelagem precisa da degradação de baterias é um pré-requisito para a operação economicamente viável de Sistemas de Armazenamento de Energia em Baterias (BESS - Battery Energy Storage Systems). No entanto, as abordagens existentes frequentemente enfrentam um compromisso entre a robustez extrapolativa das equações semi-empíricas e a flexibilidade dos métodos baseados em dados. Este trabalho propõe uma estrutura de Regressão de Processo Gaussiano (GPR - Gaussian Process Regression) Híbrida Exponencial guiada pela física para prever a perda de capacidade de células de íons de lítio Samsung INR21700-50E. Aproveitando um conjunto de dados abrangente que engloba 71 condições distintas de envelhecimento, três estratégias de modelagem são avaliadas: um Modelo Semi-Empírico de referência (baseline), um modelo GPR Híbrido e um modelo GPR Híbrido Exponencial. Os resultados revelam que o envelhecimento calendário exibe flutuações complexas e não monotônicas com o Estado de Carga (SoC - State of Charge) que os modelos semi-empíricos tradicionais falham em capturar. Embora os métodos padrão baseados em dados resolvam essa não linearidade local, eles são propensos a inconsistências físicas, como a previsão de recuperação de capacidade em regiões não treinadas. O GPR Híbrido Exponencial proposto supera essas limitações empregando uma arquitetura de kernel composto — combinando os kernels Dot-Product e Matérn — para impor consistência física ao mesmo tempo em que retém a flexibilidade dos métodos baseados em dados. O modelo confirma estatisticamente o impacto insignificante da taxa de carga/descarga (C-rate) para a química desta célula e demonstra uma capacidade de generalização superior, reduzindo a Raiz do Erro Quadrático Médio Normalizado (nRMSE) global de 14,78% (baseline) para 2,45%. Essas descobertas ressaltam o potencial do aprendizado de máquina guiado pela física para a previsão confiável da vida útil em espaços operacionais esparsos e multidimensionais.

Palavras-chave: Bateria de íons de lítio. Sistemas de Armazenamento de Energia em Baterias. Operação Ciente do Envelhecimento. Modelagem de Degradação. Regressão de Processo Gaussiano. Aprendizado de Máquina. Modelo Semi-Empírico.

ABSTRACT

Accurate battery degradation modeling is a prerequisite for the cost-effective operation of Battery Energy Storage Systems (BESS). However, existing approaches often face a trade-off between the extrapolative robustness of semi-empirical equations and the flexibility of data-driven methods. This paper proposes a physics-guided Hybrid Exponential-Gaussian Process Regression (GPR) framework to predict the capacity fade of Samsung INR21700-50E lithium-ion cells. Leveraging a comprehensive dataset encompassing 71 distinct aging conditions, three modeling strategies are evaluated: a baseline Semi-Empirical Model, a Hybrid GPR, and Hybrid Exponential-GPR model. The results reveal that calendar aging exhibits complex, non-monotonic fluctuations with State of Charge (SoC) that traditional semi-empirical models fail to capture. While standard data-driven methods resolve this local nonlinearity, they are prone to physical inconsistencies, such as predicting capacity recovery in untrained regions. The proposed Hybrid Exponential-GPR overcomes these limitations by employing a composite kernel architecture—combining Dot-Product and Matérn kernels—to enforce physical consistency while retaining data-driven flexibility. The model statistically confirms the negligible impact of C-rate for this cell chemistry and demonstrates superior generalization capability, reducing the global Normalized Root Mean Square Error (nRMSE) from 14.78% (baseline) to 2.45%. These findings underscore the potential of physics-guided machine learning for reliable lifetime prediction in sparse, multi-dimensional operational spaces.

Key-words: Lithium-ion Battery, Battery Energy Storage Systems, Aging-Aware Operation, Degradation Modeling, Gaussian Process Regression, Machine Learning, Semi-Empirical Model.

List of Figures

List of Tables

LIST OF ABBREVIATIONS AND ACRONYMS

AI	Artificial Intelligence
ANN	Artificial Neural Networks
ARD	Automatic Relevance Determination
BESS	Battery Energy Storage Systems
BMS	Battery Management System
CI	Confidence Interval
cLH	Conditioned Latin Hypercube
DoD	Depth of Discharge
DoE	Design of Experiments
DVA	Differential Voltage Analysis
ECM	Equivalent Circuit Models
EIS	Electrochemical Impedance Spectroscopy
EKF	Extended Kalman Filter
EOL	End-of-Life
EV	Electric Vehicle
FF	Full Factorial
GP	Gaussian Process
GPR	Gaussian Process Regression
ICA	Incremental Capacity Analysis
LAM	Loss of Active Material
LFP	Lithium Iron Phosphate
LLI	Loss of Lithium Inventory
LLM	Large Language Model
LSTM	Long Short-Term Memory
MILP	Mixed Integer Linear Programming

ML	Machine Learning
MLE	Maximum Likelihood Estimation
NMC	Lithium Nickel Manganese Cobalt Oxide
nRMSE	Normalized Root Mean Square Error
PDE	Partial Differential Equation
pi-OED	Parameter Individual Optimal Experimental Design
RBF	Radial Basis Function
RI	Resistance Increase
RMSE	Root Mean Square Error
RNN	Recurrent Neural Networks
RPT	Reference Performance Test
RUL	Remaining Useful Life
SEI	Solid Electrolyte Interphase
SoC	State of Charge
SoH	State of Health
SVM	Support Vector Machines
TP	Test Point
UKF	Unscented Kalman Filter

Contents

1 INTRODUCTION

This chapter introduces the fundamental motivation and scope of this dissertation. It begins by establishing the context of lithium-ion battery degradation in energy storage systems and outlining the main challenges in current modeling approaches. Subsequently, it defines the general and specific objectives of this research, highlights the scientific contributions of the proposed hybrid frameworks, and provides a formal declaration regarding the use of artificial intelligence tools. Finally, it outlines the structural organization of the remaining chapters.

1.1 CONTEXT AND MOTIVATION

The transition towards renewable energy systems has driven the massive deployment of Battery Energy Storage Systems (BESS) for applications ranging from self-consumption and peak shaving to ancillary grid support. While lithium-ion batteries are currently the technology of choice due to their high energy density and cycle life, their performance is not static; it degrades over time. This degradation directly impacts system reliability, safety, and long-term profitability.

As demonstrated in [1], operating a BESS without explicitly accounting for aging effects can lead to accelerated capacity fade. This is particularly critical in long-duration or high-frequency cycling applications, where neglecting degradation results in reduced economic returns. Conversely, incorporating aging-aware models into BESS operation improves lifetime utilization and enables more cost-effective scheduling and maintenance planning [2]. Therefore, accurate degradation modeling is not merely a technical requirement but a fundamental aspect of the economic design and control of energy storage systems.

Beyond understanding the electrochemical aging mechanisms at the cell level, the ultimate goal of this research is to translate these complex behaviors into practical, computational models that can be embedded into a Battery Management System (BMS). By reliably predicting the State of Health (SoH), these models empower intelligent, aging-aware control strategies that optimize power dispatch, ensure safe operation, and extend the operational lifespan of the battery asset.

However, modeling lithium-ion battery degradation is challenging due to the complexity of the underlying electrochemical and mechanical mechanisms. Traditional approaches often rely on rigid parametric functions that may oversimplify these behaviors, or pure data-driven methods that lack physical consistency.

1.2 OBJECTIVES

1.2.1 General Objective

The general objective of this dissertation is to develop and evaluate a comprehensive, physics-guided modeling framework to predict the capacity fade of lithium-ion batteries, specifically the Samsung INR21700-50E. This work aims to overcome the limitations of rigid parametric equations by integrating data-driven techniques, specifically Gaussian Process Regression (GPR).

1.2.2 Specific Objectives

To achieve the general objective, the following specific steps have been defined:

- Establish a baseline Semi-Empirical Model to determine the physics-based parameters governing degradation.
- Develop a novel Hybrid GPR Model that replaces deterministic stress functions with Gaussian Processes (GP) to capture complex, multi-dimensional aging dependencies.
- Create a novel Hybrid Exponential-GPR Model incorporating an exponential structure and a composite kernel architecture to resolve common data-driven issues, such as non-physical predictions in untrained regions.
- Implement and validate these models using a comprehensive aging dataset encompassing distinct calendar and cycling conditions.
- Evaluate and compare the performance of the proposed frameworks in terms of physical consistency (extrapolation capabilities) and data fitting accuracy.

1.3 CONTRIBUTION

A detailed literature review regarding battery degradation and modeling strategies will be presented in Chapter 2. However, it can be anticipated that while traditional physicochemical and semi-empirical models offer stability, they often struggle to perfectly fit complex, nonlinear aging trajectories. On the other hand, purely data-driven methods lack physical meaning and may predict impossible behaviors when extrapolating data.

Therefore, this work addresses this gap by proposing a hybrid approach. It introduces a modeling framework that mathematically links physical stress factors to degradation, allowing the GPR to learn the nonlinearities and complex relationships directly from experimental data. By incorporating an exponential structure and a composite kernel architecture, the Hybrid Exponential-GPR Model proposed in this work acts as a physics-guided framework. It inherently aligns the data-driven learning process with the dynamic behaviors expected from traditional semi-empirical functions, guaranteeing physical consistency while providing highly accurate predictions of capacity fade under dynamic usage profiles. Ultimately, this yields a robust tool ready for integration into advanced BMS architectures, directly supporting the practical objective of safely and economically managing large-scale energy storage systems.

1.4 DECLARATION OF GENERATIVE AI USE

During the preparation of this dissertation, the author utilized Artificial Intelligence (AI) tools, specifically Large Language Models (LLMs), to assist in the research and writing process. AI assistance was primarily employed for language translation, text revision, and structural refinement to ensure the clarity and fluency of the English manuscript. Additionally, these tools were used as supplementary aids during the development and debugging of the Python code for the proposed regression models. Following the use of these generative AI tools, the author carefully reviewed, verified, and edited all outputs, assuming full responsibility for the final integrity, accuracy, and scientific content of this document.

1.5 DOCUMENT STRUCTURE

The remainder of this document is organized as follows. Chapter 2 reviews the theoretical foundations of battery degradation, state-of-the-art modeling, and aging-aware operation strategies. Chapter 3 describes the methodology, detailing the mathematical formulation of the semi-empirical baseline and the kernel structures of the proposed hybrid frameworks. Chapter 4 presents the results, including the parameterization of stress factors and a comparative validation against aging datasets. Finally, Chapter 5 concludes the work, highlighting the superior generalization capability of the physics-guided hybrid approach.

2 LITERATURE REVIEW

This chapter establishes the comprehensive theoretical foundation required for the advanced management and modeling of lithium-ion battery systems. It systematically reviews the fundamental mechanisms of battery degradation, the stress factors that accelerate these complex processes, the state-of-the-art modeling strategies (ranging from physicochemical to data-driven approaches), and the critical transition from SoH diagnostics to predictive prognostics. Finally, it addresses the integration of these degradation models into aging-aware operational planning and optimization frameworks.

2.1 BATTERY DEGRADATION FUNDAMENTALS

The rapid adoption of lithium-ion batteries in electric vehicles (EVs) and stationary BESS is driven by their high energy density, power capability, and decreasing costs [1, 3]. However, battery degradation remains a primary bottleneck, manifesting as capacity fade, power fade, and resistance increase over the system's lifetime [1, 4]. Battery aging is a highly nonlinear and multi-physics phenomenon that occurs continuously, regardless of whether the battery is actively used or resting [4, 5].

2.1.1 Calendar and Cycle Aging

In the literature, battery degradation is fundamentally divided into two operational regimes: calendar aging and cycle aging [1, 6]. Calendar aging encompasses all degradation processes that occur while the battery is at rest or in storage [7, 8]. It is primarily governed by the ambient temperature and the State of Charge (SoC) at which the battery is maintained [1, 9]. Cycle aging, conversely, describes the deterioration induced by the active charging and discharging of the cell [1, 9]. Cycle aging introduces additional stress factors, most notably the Depth of Discharge (DoD), and the charge/discharge current rate (C-rate) [10, 11].

In real-world applications, such as EVs or grid frequency regulation, batteries experience a dynamic combination of both calendar and cycle aging, requiring models capable of superposition or coupled analysis to accurately reflect total capacity fade [1, 12].

2.1.2 Microscopic Degradation Mechanisms

The macroscopic effects of capacity fade and resistance increase are driven by several overlapping internal microscopic mechanisms [13]. The literature generally classifies these phenomena into specific degradation modes, prominently the Loss of Lithium Inventory (LLI), Loss of Active Material (LAM), and Resistance Increase (RI) [1]. These phenomenological modes are the direct consequence of specific physical and chemical mechanisms occurring within the cell. The most critical mechanisms include:

- **Solid Electrolyte Interphase (SEI) Growth:** The formation and continuous thickening of the SEI layer on the graphite anode is universally recognized as the dominant degradation mechanism in lithium-ion batteries [1, 12]. The SEI layer forms as a result of electrolyte decomposition and irreversibly consumes cyclable lithium ions, leading directly to LLI [1, 5]. Furthermore, as the SEI layer thickens, it impedes ion transport, contributing significantly to the cell's overall RI [1, 4].
- **Structural Degradation and Particle Isolation:** Microscopic mechanical and chemical mechanisms—such as transition metal dissolution (e.g., manganese at high temperatures) and particle cracking due to stress during volume expansion and contraction—occur on both electrodes [1, 14]. These mechanisms lead to the detachment and isolation of electrode materials, resulting in LAM. This effectively reduces the surface area available for lithium insertion, directly impairing battery capacity and power capability [1, 5].
- **Lithium Plating:** Under specific extreme conditions—such as low operating temperatures or excessively high charging currents—lithium ions cannot intercalate into the graphite lattice fast enough. Instead, they deposit as metallic lithium on the anode surface [1, 14]. This lithium plating not only causes severe capacity fade through rapid LLI but also poses severe safety risks due to potential dendrite formation and internal short circuits [14, 15].

2.1.3 Stress Factors

The rate at which these degradation mechanisms progress is governed by multiple external and internal stress factors. High temperatures exponentially accelerate parasitic side reactions like SEI growth and transition metal dissolution [14]. This temperature dependency is typically modeled using the Arrhenius equation [1, 9]. Conversely, very low temperatures trigger lithium plating [14].

Operating at high SoC levels accelerates calendar aging due to high electrode potentials, while deep cycling (high DoD) and high C-rates cause severe mechanical stress, leading to LAM and accelerated cycle aging [1, 9, 16].

Consequently, because tracking the exact evolution of internal microscopic mechanisms is highly complex, macroscopic stress factors—such as temperature, SoC, DoD, and C-rate—serve as effective proxy variables to understand and predict overall battery degradation.

2.2 DEGRADATION MODELING STRATEGIES

To effectively translate these complex physical phenomena into applicable mathematical tools, the literature presents a spectrum of modeling strategies. These can be broadly categorized into physicochemical, empirical, semi-empirical, and data-driven models [1, 5]

2.2.1 Physicochemical Models

Physicochemical models, or electrochemical models, provide the highest level of physical fidelity by simulating internal mass transport, charge transfer kinetics, and thermodynamic processes [10, 17]. These models solve complex partial differential equations (PDEs), offering deep insights into internal states such as lithium concentration and potential gradients [18, 19]. However, their immense computational burden, coupled with the difficulty of parameterizing numerous unmeasurable internal variables, often makes them unsuitable for real-time onboard BMS applications or large-scale optimization loops [18, 19].

2.2.2 Empirical Models

At the opposite end of the spectrum, purely empirical models rely entirely on mapping stress factors to capacity fade using mathematical functions like polynomials, power laws, or exponential decays. While computationally highly efficient and easy to implement, empirical models lack physical meaning [19]. Consequently, they possess poor generalization capabilities and cannot accurately extrapolate degradation behavior when the battery is subjected to operating conditions outside the original training dataset [19, 20].

2.2.3 Semi-Empirical Models

A robust and widely adopted compromise in current engineering applications is the semi-empirical model. These models combine physical intuition—such as using the Arrhenius law for temperature dependence and square-root-of-time functions for SEI diffusion—with parameters fitted from accelerated aging data [1].

For instance, the framework developed by [6] decouples degradation into a nonlinear SEI formation component and a linearized aging component dependent on stress factors, utilizing Rainflow cycle-counting algorithms to process irregular operational profiles. Similarly, comprehensive semi-empirical models developed by [21] for NMC cells and [12] for LFP cells demonstrate high accuracy in predicting both capacity fade and resistance increases under dynamic profiles. The formulation of multi-factor models, as shown by [9], integrates temperature, SoC, and DoD to predict total capacity fade in real-time verifications.

However, the efficacy of these models relies heavily on the availability of high-quality, comprehensive experimental data. Public datasets employing advanced Design of

Experiments (DoE) on commercial cells, such as the multi-stage aging study presented by [22], are critical for accurately calibrating these semi-empirical equations.

To summarize the landscape of degradation modeling, Table 1 presents a comparative overview of the physicochemical, empirical, and semi-empirical strategies discussed, highlighting their respective advantages and limitations within the context of battery management systems.

Table 1 – Comparison of Degradation Modeling Strategies: Advantages and Limitations.

Modeling Strategy	**Advantages (Pros)**	**Limitations (Cons)**
Physicochemical	Highest physical fidelity; provides deep insights into internal states (e.g., lithium concentration).	Immense computational burden; highly difficult to parameterize unmeasurable variables; unsuitable for real-time BMS.
Empirical	Highly computationally efficient; straightforward mathematical formulation; extremely easy to implement.	Lacks physical meaning; poor generalization; cannot reliably extrapolate outside the original training dataset.
Semi-Empirical	Robust compromise between physical intuition and efficiency; highly accurate for dynamic operational profiles.	Relies heavily on the availability of high-quality, comprehensive experimental data and advanced DoE for calibration.

Source: Elaborated by the author.

2.3 ADVANCED STATE ESTIMATION AND HEALTH DIAGNOSTICS

The continuous estimation of the battery's current conditions is a core function of the BMS, essential for safety, efficiency, and longevity [23]. The SoH acts as a macroscopic indicator of the battery's current maximum capacity relative to its fresh state [4, 20].

2.3.1 Direct Assessment and Analytical Techniques

SoH estimation can be approached through direct measurements or advanced analytical techniques [17, 24]. While simple methods like Coulomb counting are computationally light, they are prone to cumulative sensor errors over time [24, 25]. Electrochemical Impedance Spectroscopy (EIS) provides a wealth of information regarding internal resistance and charge transfer kinetics, but requires specialized onboard hardware, limiting its widespread application [17, 19]. Alternatively, Incremental Capacity Analysis (ICA) and Differential Voltage Analysis (DVA) have emerged as powerful diagnostic tools [18, 19]. By differentiating the voltage curve with respect to capacity (dQ/dV or dV/dQ), these methods convert flat voltage plateaus into distinct peaks. Analyzing the shifts, area, and amplitude of these peaks allows researchers to non-destructively isolate and identify underlying degradation mechanisms, such as distinguishing between LLI and LAM [19].

2.3.2 Model-Based Observers

For real-time execution, model-based observers coupled with Equivalent Circuit Models (ECM) are highly prevalent [4, 25]. Observers such as the Extended Kalman Filter (EKF), Unscented Kalman Filter (UKF), and Sliding Mode Observers continuously correct the battery's internal state estimates by minimizing the error between measured and model-predicted terminal voltages [4, 17, 23].

These adaptive filtering techniques provide high precision and can effectively track nonlinear degradation dynamics, although they require careful tuning to ensure robustness against sensor noise and temperature fluctuations [20, 23].

2.4 PREDICTIVE PROGNOSTICS AND DATA-DRIVEN APPROACHES

While SoH estimation (diagnostics) answers the question of current capacity, predictive prognostics answers a more complex question: how much longer can the battery operate safely [20]? Remaining Useful Life (RUL) prediction forecasts the future degradation trajectory until the battery reaches its End-of-Life (EOL) threshold, typically defined as 80% or 70% of initial capacity [19, 20]. Accurately determining this operational horizon is essential to prevent unexpected failures, ensure operational safety, and optimize replacement schedules across both mobility and stationary applications.

2.4.1 Machine Learning and Data Science

The sheer complexity of battery aging has catalyzed a shift towards data-driven approaches and Machine Learning (ML) techniques [5, 20]. These model-free approaches learn the nonlinear degradation patterns directly from historical datasets without requiring explicit prior knowledge of electrochemical mechanisms [20]. Filtering and ML methods for capacity degradation modeling typically use online data from the system of interest. Bayesian filters, such as Kalman filters and particle filters, allow the estimation and updating of the fitting parameters of degradation models during the operation phase [20].

Furthermore, ML methods, such as Artificial Neural Networks (ANN) and Support Vector Machines (SVM), rely on training data to tune the models before being applied to online data of the system of interest. Algorithms like Recurrent Neural Networks (RNN) and Long Short-Term Memory (LSTM) networks have also demonstrated superior capability in capturing long-term dependencies and mapping high-dimensional aging features [15, 20, 23]. However, pure ML methods tend to not provide a direct algebraic link between external stress factors and capacity fade, which makes them challenging to integrate into mathematical scheduling methods and optimization strategies.

2.4.2 Advanced Predictive Frameworks

To address the limitations of purely black-box data-driven methods, GPR has gained significant traction for RUL prediction. Unlike deterministic neural networks, GPR provides a probabilistic, non-parametric framework, offering not only high-accuracy regression but also strict confidence intervals and uncertainty quantification for its predictions. The authors in [26] demonstrated that employing specific mean functions combined with compositional kernels allows GPR to incorporate prior empirical knowledge of cell degradation, substantially improving long-term forecasting accuracy.

This adaptability makes GPR exceptionally well-suited for developing hybrid semi-empirical models. By pairing semi-empirical baseline equations with GPR, it becomes possible to algebraically link physical stress factors to degradation while allowing the GPR to learn and compensate for the nonlinear, unmodeled residuals from the data. Furthermore, predicting battery lifetime accurately before significant capacity fade is observed remains a monumental challenge [27].

2.5 AGING-AWARE OPERATIONS AND PROGNOSTICS

The ultimate objective of degradation modeling and prognostics is to inform decision-making, shifting from passive monitoring to active aging-aware operation [1]. Because the battery represents the primary capital expenditure in energy storage projects, optimizing its operational profile to extend its lifespan directly impacts economic viability [1, 28].

2.5.1 Operational Optimization

Aging-aware strategies balance the trade-off between maximizing immediate technical utility (e.g., generating revenue from energy arbitrage or frequency regulation) and minimizing degradation [1]. To actively internalize battery degradation into the scheduling method, optimization frameworks explicitly incorporate aging costs into their objective functions. Mathematically, the scheduling algorithm aims to maximize the profit $\mathbb{P}$ of the system over a set of time steps T, while accounting for the cost of degradation $\mathbb{C}^{\text{aging}}$. An exemplary objective function can be formulated in its general form, as shown in Equation 2.1.

$$\max \sum_{t \in T} \left(\mathbb{P}_t - \mathbb{C}_t^{\text{aging}} \right) \tag{2.1}$$

The specific aging cost at time step t, $\mathbb{C}_t^{\text{aging}}$, is defined as a penalty factor derived from the capacity fade change. This generally encompasses both calendar aging ($\Delta Q_{\text{loss},t}^{\text{cal}}$) and cyclic aging ($\Delta Q_{\text{loss},t}^{\text{cyc}}$). These capacity loss components are then multiplied by a specific monetary aging cost per unit of capacity loss, c_{aging}, as formulated in Equation 2.2.

$$\mathbb{C}_t^{\text{aging}} = \left(\Delta Q_{\text{loss},t}^{\text{cal}} + \Delta Q_{\text{loss},t}^{\text{cyc}}\right) * c_{\text{aging}} \quad \forall t \in T \tag{2.2}$$

Because degradation behavior relative to the system's operational states is inherently nonlinear, integrating these exact models directly into exact solution approaches can be computationally prohibitive. To address this, algorithms such as Mixed Integer Linear Programming (MILP) frequently employ piecewise linearization techniques. By partitioning the nonlinear degradation curves into sets of linear functions, the optimization problem effectively bounds the capacity fade constraints without explicitly defining the underlying stress factors in the primary equations. This formulation ensures the solver actively penalizes and avoids operating conditions that accelerate degradation, leading to significantly different and more economically sound power dispatch strategies compared to models that ignore degradation costs [10].

2.5.2 System Sizing and Planning

The implications of aging-aware operation extend naturally into the initial planning and sizing phases of battery energy storage systems. Because optimal dispatch strategies restrict the operational envelope—such as penalizing extreme SoC or limiting the DoD to mitigate degradation—the effective usable capacity of the battery dynamically differs from its nominal capacity [1]. Consequently, ignoring capacity fade and these operational constraints during the dimensioning of BESS for microgrids or renewable energy integration inevitably leads to under-sizing and an inability to meet future load demands [29].

To address this gap, modern optimization frameworks increasingly co-optimize both scheduling and system sizing. For instance, sizing models can introduce lifetime energy throughput limits derived directly from semi-empirical aging models, using target lifespans and EOL capacity thresholds as baseline constraints for the solver [1]. Moreover, environmental variables play a crucial role in these planning stages. Ambient temperature variations significantly alter capacity fade rates and operating efficiencies [30, 31].

Therefore, optimal configuration models must integrate dynamic temperature constraints, detailed degradation penalties, and rigorous load forecasting. This holistic approach ensures accurate determination of the required energy capacity, reliable prediction of replacement intervals, and the true lifecycle profitability of the investment [30, 31]. Ultimately, integrating advanced data science methodologies into full lifespan management—spanning from initial system sizing and operational dispatch to eventual second-life reutilization—represents the frontier of modern BMS [3].

2.6 SUMMARY

This chapter provided a comprehensive review of the theoretical and state-of-the-art foundations regarding lithium-ion battery degradation. The literature underscores that battery aging is a multi-physics phenomenon driven primarily by microscopic mechanisms such as SEI growth and lithium plating [13, 4]. These processes are highly sensitive to operational stress factors, including temperature, SoC, and DoD [1, 6].

A critical analysis of existing modeling strategies reveals a persistent trade-off: while physicochemical models offer high fidelity, they are computationally prohibitive for real-time applications [18]. Conversely, empirical and pure machine learning methods, despite their flexibility and efficiency, often lack physical consistency and fail to generalize outside their training domain [20, 19].

Building upon the context and motivation established in Chapter 1, this review highlights that the integration of semi-empirical foundations with GPR offers a promising path to overcome these limitations [26]. By leveraging the probabilistic nature of GPR and the structural stability of physics-based equations, it is possible to develop models that are both accurate and consistent. This theoretical background provides the necessary justification for the hybrid frameworks proposed in this work, which will be detailed in the methodology presented in the following chapter.

3 METHODOLOGY

This chapter details the methodology developed to predict the capacity fade of the Samsung INR21700-50E lithium-ion batteries. It outlines the systematic approach taken, from the initial data processing and feature extraction to the mathematical formulation of the baseline Semi-Empirical Model, the proposed Hybrid GPR frameworks, and the computational tools utilized for simulation and modeling. Finally, it describes the validation strategy used to evaluate the predictive performance and physical consistency of the developed models.

3.1 PROPOSED FRAMEWORK OVERVIEW

The proposed modeling framework is illustrated in Figure 1. The process begins with the consolidation of raw experimental data obtained from both calendar and cycling aging tests. This dataset undergoes a preprocessing stage, which includes feature extraction and data cleaning to ensure input consistency.

Figure 1 – Proposed methodological framework for the development and assessment of hybrid semi-empirical degradation models.

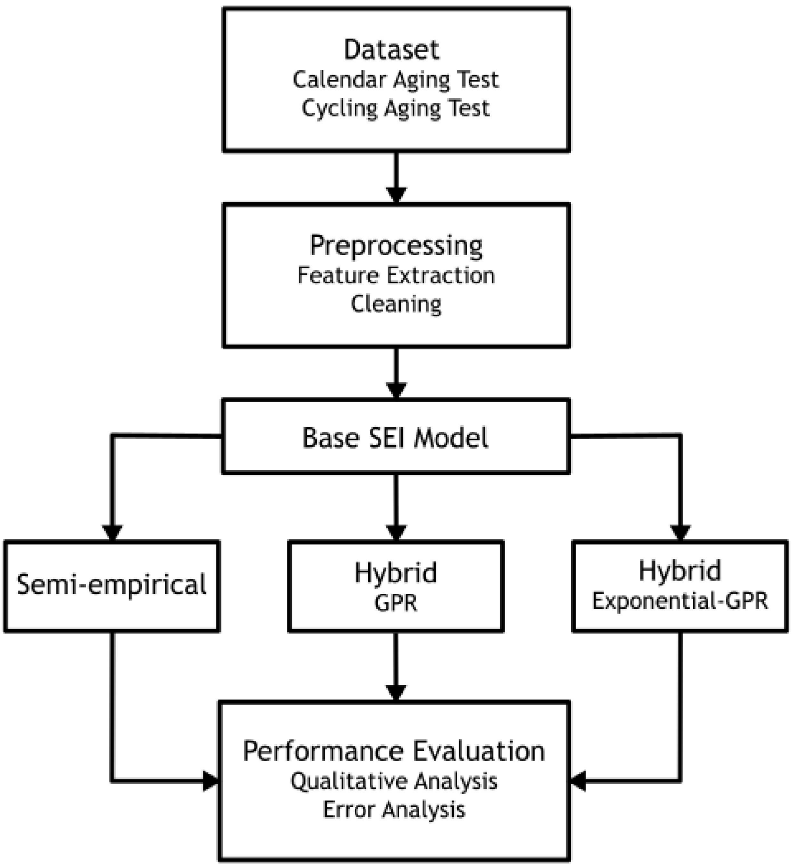

Source: Elaborated by the author.

Central to the methodology is the definition of a Base SEI Model, which establishes the physics-based governing SEI growth. From this theoretical foundation, three distinct modeling approaches are derived and compared:

- The Semi-Empirical Model originally proposed by [6];
- A Hybrid GPR Model, combining the Base SEI Model with GPR;
- A Hybrid Exponential-GPR Model, incorporating an exponentiation stage prior to the GPR to accurately reflect the degradation dynamics.

Finally, the models undergo a comprehensive performance evaluation. This assessment begins with a qualitative analysis of the models' interpolation and extrapolation behavior to ensure physical consistency beyond the training data, followed by a quantitative goodness-of-fit metric calculated over the available samples.

3.2 DATASET

To validate the proposed models, this study utilizes a comprehensive, high-density aging dataset recently published in [22]. This dataset was selected due to its extensive coverage of aging conditions.

The experimental campaign was conducted on 279 commercially available Samsung INR21700-50E lithium-ion battery cells, which are high-energy cylindrical cells with a rated capacity of 4.9 Ah. The dataset encompasses a total of 71 distinct aging conditions. The experiments were divided into two stages: a first exploratory stage utilizing a non-model-based DoE to determine baseline degradation behavior, and a second optimized stage employing a model-based parameter individual Optimal Experimental Design (pi-OED) to refine specific dependencies [22].

The study was conducted across three distinct laboratories in Germany: Siemens in Erlangen, Intilion (which transitioned to Hoppecke during the project) in Zwickau, and the University of Applied Sciences Munich in Munich. Despite the distributed nature of the testing, each facility adhered to a strictly standardized experimental setup and identical test protocols to guarantee consistency across all results [22].

The experimental design strategy was specifically tailored to address the differing dimensionality of the aging modes. For the calendar aging study, a Full Factorial (FF) motivated design was employed to systematically map the dependencies. In contrast, for the cycle aging study, the high number of degrees of freedom—encompassing temperature, SoC, DoD, and C-rate—resulted in an extensive combination of potential test conditions. Consequently, a conditioned Latin Hypercube (cLH) sampling strategy was chosen to efficiently allocate test points to the available equipment. This approach ensures a space-filling distribution of data points, which is critical for capturing the degradation behavior across a high-dimensional parameter space without the prohibitive cost of a FF design [22].

The cells were subjected to both calendar and cycle aging under tightly controlled environmental conditions, with ambient temperatures constrained to 10°C, 23°C, 35°C, and 45°C to simulate realistic operational scenarios for stationary battery energy storage systems. Cycle aging protocols involved varying charge and discharge C-rates ranging from 0.05 C to 1 C for charging and up to 2 C for discharging. Additionally, the DoD and maximum SoC were controlled as key experimental variables. These parameters were specifically restricted to maintain the operational SoC generally between 20% and 80%, ensuring the avoidance of constant voltage phases and maintaining consistent constant current profiles throughout the aging cycles. Throughout the campaign, the remaining capacity was tracked through Reference Performance Tests (RPTs) conducted at regular intervals [22].

As shown in Figure 1, prior to the modeling phase, a dedicated feature extraction and data cleaning process was executed. Feature extraction was performed to aggregate the raw data from the periodic RPTs into a structured dataset suitable for regression analysis. The key parameters extracted and their specific definitions for this study are detailed below:

- **Normalized Capacity (Q):** The remaining capacity was selected as the primary indicator of SoH. To ensure comparability across different cells, all capacity values were normalized relative to the specific initial capacity of each cell, establishing a uniform baseline of 100% at the beginning of the tests.
- **Time (t):** The cumulative number of days elapsed from the start of the test to the specific RPT.
- **Temperature (T):** For the calendar aging dataset, the ambient chamber temperature was utilized as the model input, under the valid assumption of thermal equilibrium due to the absence of current flow. In contrast, for the cycle aging dataset, the input was defined as the mean surface temperature of the cell measured throughout the cycles, thereby accounting for internal heat generation.
- **State of Charge (SoC):** This parameter represents the fixed storage level for calendar test points. For cycling tests, the mean operational SoC was calculated over the charge/discharge window.

- **Cycle Count (N) and Depth of Discharge (DoD):** For cycling conditions, the total number of cycles accumulated up to the RPT and the specific DoD were extracted directly.
- **C-rate (C):** Although the experimental protocol applied distinct current magnitudes for charging and discharging, this study synthesized the current stressor by computing the arithmetic mean of the charge and discharge C-rates.

Following feature extraction, a cleaning procedure was applied to address specific irregularities. As documented in the dataset reports, certain test points or individual cells exhibited inconsistencies due to known incidents such as equipment malfunctions, sensor errors, or procedural deviations during testing. These inconsistent data points were identified and purged to ensure the robustness and reliability of the training data. A detailed table cataloging all specific modifications and exclusions applied to the raw dataset is presented in the Appendix A.

To visualize the structure of the processed dataset, representative aging trajectories are presented in Figures 2 and 3. Figure 2 illustrates the capacity fade over time for a specific calendar aging condition (T=45°C, SoC=65%), while Figure 3 depicts the degradation evolution against the accumulated cycle count for a cycling test point.

Figure 2 – Representative calendar aging trajectory for cells stored at 45.0°C and 65.0% SoC.

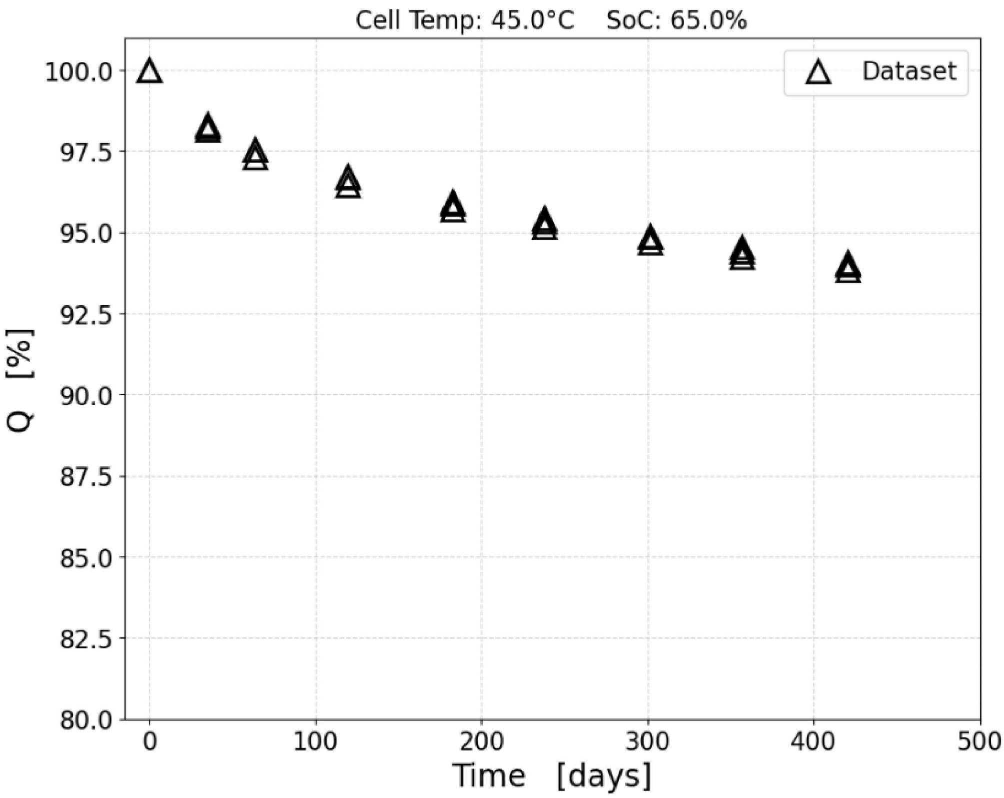

Source: Elaborated by the author.

Figure 3 – Representative cycle aging trajectory for cells cycled at 56.3°C, 52.5% SoC, 15% DoD, and 1.40 C.

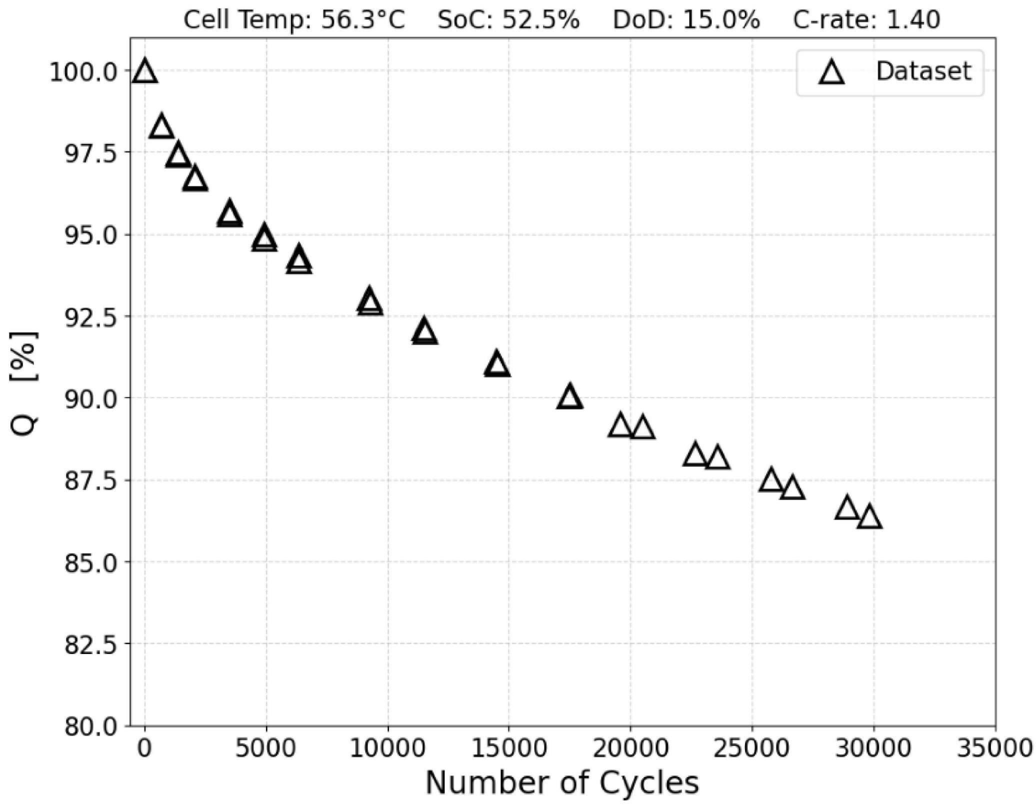

Source: Elaborated by the author.

A distinct characteristic observed in these plots is the presence of multiple data points clustered at specific time or cycle intervals. This pattern arises because the experimental design involved testing multiple cells under identical operating conditions to ensure statistical reliability. Consequently, at each RPT, the graphs display a dispersion of capacity values rather than a single point. This clustering reflects the inherent cell-to-cell variability within the batch, providing the necessary data variance to train the probabilistic components of the proposed models.

3.3 BASE SEI MODEL

To model battery degradation, the Semi-Empirical Model from [6] was chosen, using its fundamental formulation shown in Equation (3.1).

$$Q = \alpha_{\text{sei}} e^{-\beta_{\text{sei}} f_d} + (1 - \alpha_{\text{sei}}) e^{-f_d} \tag{3.1}$$

where the parameters α_{sei} and β_{sei} govern the nonlinearity of the degradation process, while f_d is the degradation factor associated with stressors. The two-exponential structure allows for the modeling of two separate degradation time constants: a fast initial one linked to quick SEI layer formation during early cycling, and a slower, sustained one that reflects the cell's long-term aging [1].

Figure 4 presents a graphical representation of a li-ion battery's performance degradation.

Figure 4 – Li-ion battery degradation profile showing the range of model applicability and the End of Life.

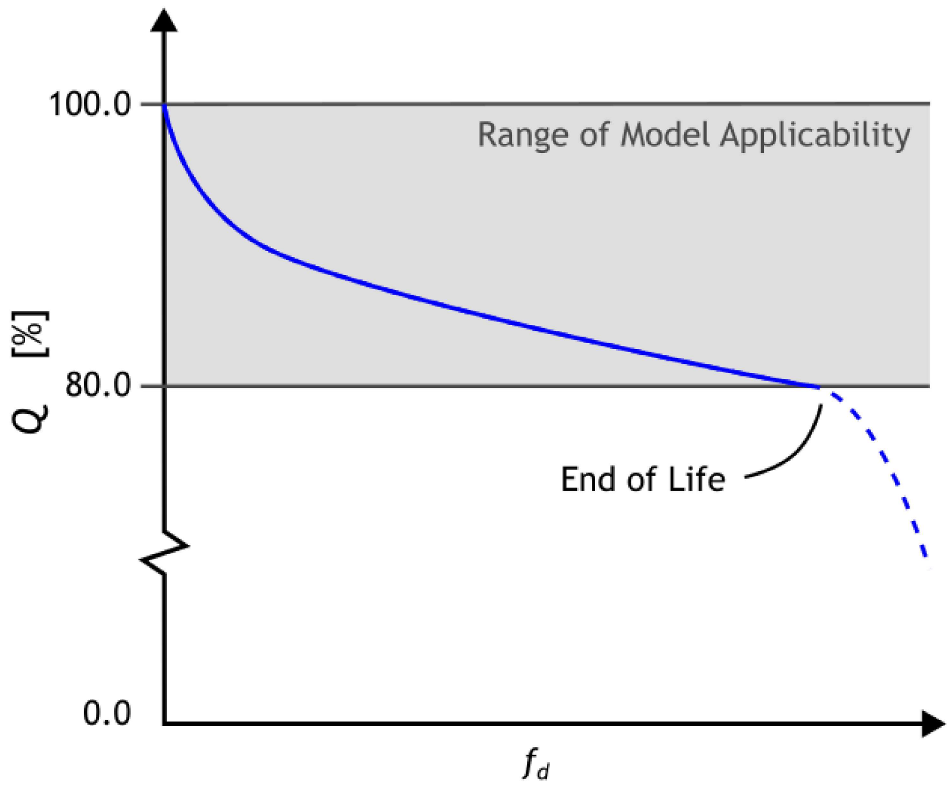

Source: Elaborated by the author.

This graph shows Q against the degradation factor (f_d). The shaded area delineates the range of model applicability (100% down to 80% capacity). The battery reaches its EOL criterion at 80%, beyond which the model's accuracy is no longer guaranteed (dashed line).

The degradation function f_d is defined in Equation (3.2).

$$f_d = \sum_{i=1}^{t} t_i \cdot f_{d,\mathrm{cal}}(T_i, SoC_i) + \sum_{j=1}^{N} n_j \cdot f_{d,\mathrm{cyc}}(T_j, SoC_j, DoD_j, C_j) \tag{3.2}$$

where:

t_i: time interval;

t**:** total number of intervals;

n_j**:** cycle weight (1 for a full cycle, 0.5 for a half cycle);

N**:** total number of cycles;

$f_{d,\mathbf{cal}}$**:** degradation factor due to calendar aging;

$f_{d,\mathbf{cyc}}$**:** degradation factor due to cycling aging;

T**:** cell temperature;

SoC**:** state of charge;

DoD**:** depth of discharge;

C**:** C-rate.

Equation (3.2) therefore decomposes the overall degradation into a purely temporal component, $f_{d,\text{cal}}$, plus a sum of per-cycle contributions, $f_{d,\text{cyc}}$, weighted by n_j. The weighting factor n_j, assigned to each cycle i, originates from the Rainflow algorithm, a well-established method for cycle counting in fatigue and degradation analyses. In the context of battery aging, the Rainflow algorithm enables the identification and classification of irregular and non-uniform cycles, which are common in real-world operation profiles [6]. It assigns a value of 1.0 to full cycles and 0.5 to half cycles, allowing partial load fluctuations to be appropriately accounted for in the degradation model.

To apply this general framework to specific experimental conditions, the model can be simplified. For calendar aging tests, the cycle-dependent term vanishes as no current cycling occurs. Furthermore, since a calendar aging test point maintains constant stress factors (temperature and SoC) throughout the experiment, the degradation factor $f_{d,\text{cal}}(T_i, SoC_i)$ becomes a constant scalar, $f_{d,\text{cal}}$, which can be factored out of the summation. Consequently, the summation of the time intervals t_i simply aggregates to the total elapsed aging time t. This simplification yields the specific degradation function for calendar aging presented in Equation (3.3).

$$f_d = \sum_{i=1}^{t} t_i \cdot f_{d,\text{cal}}(T_i, SoC_i) = f_{d,\text{cal}}(T, SoC) \sum_{i=1}^{t} t_i = f_{d,\text{cal}} \cdot t \tag{3.3}$$

Substituting this linear time dependence back into the fundamental SEI model results in Equation (3.4).

$$Q = \alpha_{\text{sei}} e^{-\beta_{\text{sei}} f_{d,\text{cal}} t} + (1 - \alpha_{\text{sei}}) e^{-f_{d,\text{cal}} t} \tag{3.4}$$

In this formulation, α_{sei}, β_{sei}, and the specific degradation rate $f_{d,\text{cal}}$ are treated as model constants to be fitted against the experimental data, with time t serving as the independent variable.

In the case of cycle aging tests, degradation corresponds to a superposition of cyclic stress and the inevitable passage of time. Since environmental and operational parameters (temperature, SoC, DoD, and C-rate) remain constant for a specific test point, the degradation factors $f_{d,\text{cal}}$ and $f_{d,\text{cyc}}$ are treated as constants and factored out of their respective summations. Additionally, by assuming uniform full cycles throughout the test ($n_j = 1$), the sum of cycle weights simplifies to the total cycle count N. The derivation of the specific degradation function is detailed in Equation (3.5).

$$\begin{aligned}
f_d &= f_{d,\text{cal}}(T, SoC) \sum_{i=1}^{t} t_i + f_{d,\text{cyc}}(T, SoC, DoD, C) \sum_{j=1}^{N} n_j \\
&= f_{d,\text{cal}}(T, SoC) \cdot t + f_{d,\text{cyc}}(T, SoC, DoD, C) \cdot N \\
&= \left[f_{d,\text{cal}}(T, SoC) \frac{t}{N} + f_{d,\text{cyc}}(T, SoC, DoD, C) \right] N \\
&= \left[f_{d,\text{cal}}(T, SoC) t_{\text{cyc}} + f_{d,\text{cyc}}(T, SoC, DoD, C) \right] N \\
&= f^{*}_{d,\text{cyc}} N
\end{aligned} \tag{3.5}$$

As shown in the derivation, the term t/N represents the constant average duration of a single cycle, denoted as t_{cyc}. This substitution leads to the definition of the aggregated cycle degradation factor, $f^{*}_{d,\text{cyc}}$.

It is crucial to distinguish this parameter from the pure cycle factor $f_{d,\text{cyc}}$; while $f_{d,\text{cyc}}$ accounts solely for the mechanical and electrochemical stress of cycling, $f^{*}_{d,\text{cyc}}$ encapsulates the total degradation incurred during a single cycle, explicitly adding the calendar aging component accumulated during the cycle's duration t_{cyc}.

Finally, substituting this aggregated factor into the base model expresses the remaining capacity as a function of the cycle number N. Similar to the calendar model, α_{sei}, β_{sei}, and $f^{*}_{d,\text{cyc}}$ serve as the model constants to be fitted for each specific cycle test point. This relationship is expressed in Equation (3.6).

$$Q = \alpha_{\text{sei}} e^{-\beta_{\text{sei}} f^{*}_{d,\text{cyc}} N} + (1 - \alpha_{\text{sei}}) e^{-f^{*}_{d,\text{cyc}} N} \tag{3.6}$$

To finalize the parameterization of the Base SEI Model, both calendar and cycle aging datasets are utilized. By applying the specific formulations derived in Equations (3.4) and (3.6) to their respective test points, the coefficients α_{sei} and β_{sei} are extracted. It is important to note that while this initial fitting process inevitably yields a specific degradation factor ($f_{d,\text{cal}}$ or $f^*_{d,\text{cyc}}$) for each condition, only the SEI-related constants are retained at this stage. This work diverges from the methodology employed by the original authors in [6], who relied on a single arbitrary test condition for calibration. Instead, this study leverages the full extent of the experimental campaign. The model is fitted individually to every available test condition, and the final global parameters are defined as the median of the resulting distribution. To assess the reliability of this approach, a bootstrap analysis is conducted to establish confidence intervals, quantifying the uncertainty associated with these base model parameters.

Subsequently, once the global parameters α_{sei} and β_{sei} are established, a second optimization pass is conducted across all test points. In this step, the SEI coefficients are held constant, constraining the optimization to exclusively solve for the specific degradation factors $f_{d,\text{cal}}$ and $f^*_{d,\text{cyc}}$.

Consequently, this stage of the methodology yields a complete parameter set: the fixed global constants α_{sei} and β_{sei}, and the degradation factors $f_{d,\text{cal}}$ and $f^*_{d,\text{cyc}}$ for each cell at all test points. With these factors isolated, it becomes possible to analyze their sensitivity to variations in operating conditions. This analysis serves as the foundation for defining the explicit stress-dependent models $f_{d,\text{cal}}(T, SoC)$ and $f_{d,\text{cyc}}(T, SoC, DoD, C)$, which are developed and discussed in the following Sections.

Equation (3.5) can be rearranged to obtain Equation (3.7).

$$f_d = f^*_{d,\text{cyc}} N$$

$$\frac{f_d}{N} = f^*_{d,\text{cyc}}$$

$$\frac{f_{d,\text{cal}} t + f_{d,\text{cyc}} N}{N} = f^*_{d,\text{cyc}}$$

$$f_{d,\text{cal}} t_{\text{cyc}} + f_{d,\text{cyc}} = f^*_{d,\text{cyc}}$$

$$f_{d,\text{cyc}} = f^*_{d,\text{cyc}} - f_{d,\text{cal}} t_{\text{cyc}} \tag{3.7}$$

Thus, the derived calendar aging model, $f_{d,\text{cal}}(T, SoC)$, becomes a prerequisite for isolating the cyclic effects. By evaluating the calendar model under the specific environmental conditions of each cycle test, the time-dependent contribution is quantified and subtracted from the aggregated factor $f^{*}_{d,\text{cyc}}$. This operation successfully recovers the pure cycle degradation factor, $f_{d,\text{cyc}}$, yielding the specific dataset required to model the stress dependencies in the function $f_{d,\text{cyc}}(T, SoC, DoD, C)$.

3.3.1 Operationalizing the Base SEI Model for Aging-Aware Operation

Once the Base SEI Model is fully parameterized, it can be used as a predictive framework for aging-aware operation. The fundamental advantage of the formulation presented in Equation (3.1) and the linear additivity of the degradation factor f_d is that the battery's current SoH can be entirely decoupled from its specific historical stress path.

In a practical operational scenario, the current capacity of the battery, Q_{current}, is typically estimated through onboard SoH monitoring algorithms. Given Q_{current}, the fundamental model can be inverted to determine the initial accumulated degradation factor, $f_{d,\text{init}}$, which represents the battery's current aging state prior to a new operational cycle, as shown in Equation (3.8).

$$Q_{\text{current}} = \alpha_{\text{sei}} e^{-\beta_{\text{sei}} f_{d,\text{init}}} + (1 - \alpha_{\text{sei}}) e^{-f_{d,\text{init}}} \tag{3.8}$$

Because the Base SEI Model relies on a two-exponential structure, an analytical isolation of $f_{d,\text{init}}$ is not straightforward. However, since the function is monotonically decreasing within the application range, $f_{d,\text{init}}$ can be reliably and efficiently resolved using standard numerical methods.

Crucially, $f_{d,\text{init}}$ encapsulates the totality of the battery's degradation up to that exact moment, regardless of whether the historical aging originated from calendar or cyclic stresses. With this initial baseline defined, the incremental aging expected from any planned future operation can be calculated. Equation (3.9) shows that, by predicting the specific stress factors (temperature, SoC, DoD, and C-rate) of the intended operational profile, the planned degradation increment, $\Delta f_{d,\text{plan}}$, is computed using the derived stress-dependent functions.

$$\Delta f_{d,\text{plan}} = \sum_{i=1}^{t_{\text{plan}}} t_i \cdot f_{d,\text{cal}}(T_i, SoC_i) + \sum_{j=1}^{N_{\text{plan}}} n_j \cdot f_{d,\text{cyc}}(T_j, SoC_j, DoD_j, C_j) \tag{3.9}$$

This incremental factor is then simply added to the initial degradation state to determine the total future degradation factor, $f_{d,\text{future}}$, at the end of the planned operation, as shown in Equation (3.10).

$$f_{d,\text{future}} = f_{d,\text{init}} + \Delta f_{d,\text{plan}} \tag{3.10}$$

Finally, substituting $f_{d,\text{future}}$ back into the fundamental Base SEI Model yields Equation (3.11), where the predicted future capacity, Q_{future}, after the planned operation is executed, is obtained.

$$Q_{\text{future}} = \alpha_{\text{sei}} e^{-\beta_{\text{sei}} f_{d,\text{future}}} + (1 - \alpha_{\text{sei}}) e^{-f_{d,\text{future}}} \tag{3.11}$$

This mathematical framework operationalizes the model for aging-aware strategies. By evaluating $\Delta f_{d,\text{plan}}$ and the resulting Q_{future} across different prospective operating profiles, control systems can optimize dispatch schedules to actively minimize the incremental aging of the battery system while meeting operational demands.

The upcoming Sections will detail different methodological approaches used to determine the functions modeling the stress-dependent degradation factors. Nevertheless, the incremental degradation framework formulated above is inherently versatile; it can be implemented regardless of the specific mathematical structure or the underlying technique used to derive the f_d functions.

3.4 SEMI-EMPIRICAL DEGRADATION FACTOR MODEL

The degradation factor modeling approach presented here is fundamentally based on the structure proposed in [6]. However, certain modifications in presentation and term arrangement have been introduced to streamline the derivation and ensure consistency with the subsequent hybrid modeling steps. Where these divergences are structurally significant, explicit disclaimers are provided to clarify the rationale.

For calendar aging, the specific degradation factor $f_{d,\text{cal}}$ is modeled as the product of two independent stress functions, S_T and S_{SoC}, which depend exclusively on temperature and SoC, respectively, as defined in Equation (3.12).

$$f_{d,\text{cal}}(T, SoC) = S_T(T) S_{SoC}(SoC) \tag{3.12}$$

Similarly, the cycle aging degradation factor $f_{d,\text{cyc}}$ is expressed as the multiplicative combination of four distinct functions, as presented in Equation (3.13). In addition to the thermal and SoC dependencies, it incorporates the effects of DoD (S_{DoD}) and C-rate (S_C):

$$f_{d,\text{cyc}} = S_T(T) S_{SoC}(SoC) S_{DoD}(DoD) S_C(C) \tag{3.13}$$

By substituting these definitions back into the general degradation framework, the expression for the total degradation factor f_d becomes Equation (3.14).

$$f_d = \sum_{i=1}^{t} t_i \cdot S_T(T_i)\, S_{SoC}(SoC_i) + \sum_{j=1}^{N} n_j \cdot S_T(T_j)\, S_{SoC}(SoC_j)\, S_{DoD}(DoD_j)\, S_C(C_j) \tag{3.14}$$

A critical assumption of this model is that the functional forms and parameters for the thermal (S_T) and SoC (S_{SoC}) dependencies are identical for both calendar and cycle aging mechanisms. Consequently, the parameter identification follows a sequential process: the calendar aging dataset is first employed to determine S_T and S_{SoC}. These identified functions are then applied to the cycle aging dataset, allowing for the isolation and determination of the remaining cyclic-specific factors, S_{DoD} and S_C.

It is worth noting a structural modification regarding the time dependence compared to the original publication [6]. The original authors defined a distinct time-dependent function $S_t(t) = k_t \cdot t$. In the formulation presented here, the linear time dependence is inherent to the summation of time intervals ($\sum t_i$), and the proportionality constant k_t has been absorbed into the S_{SoC} function without altering the model's physical behavior.

This rearrangement aligns the mathematical structure of calendar aging with that of cycle aging: the former is driven by a summation of time intervals, while the latter is driven by a summation of cycle counts. This unified linear structure not only simplifies the interpretation but also ensures compatibility with the advanced modeling sections that follow. It allows the specific analytical forms of $f_{d,\text{cal}}$ and $f_{d,\text{cyc}}$ to be substituted with data-driven models while preserving the fundamental layout of the Base SEI Model.

To isolate the dependency of the degradation factor on temperature, a normalization procedure is applied to the calendar aging data. An arbitrary reference temperature, T_{ref}, is selected, at which the thermal stress function is defined as unity ($S_T(T_{\text{ref}}) = 1$).

Analytically, by comparing the degradation factor at any variable temperature T against the rate at this reference temperature—while holding the SoC fixed at a specific level SoC_A—the dependency on SoC is mathematically eliminated. This procedure is presented in Equation (3.15).

$$S_T(T) S_{SoC}(SoC_A) = f_{d,\text{cal}}(T, SoC_A)$$

$$\frac{S_T(T) S_{SoC}(SoC_A)}{S_T(T_{\text{ref}}) S_{SoC}(SoC_A)} = \frac{f_{d,\text{cal}}(T, SoC_A)}{f_{d,\text{cal}}(T_{\text{ref}}, SoC_A)}$$

$$S_T(T) = \frac{f_{d,\text{cal}}(T, SoC_A)}{f_{d,\text{cal}}(T_{\text{ref}}, SoC_A)} \tag{3.15}$$

Based on this theoretical relationship, the experimental data is processed to generate the target values for curve fitting. In the following expression, square brackets $[\cdot]$ are employed to denote discrete experimental observations from the dataset, distinguishing them from the continuous model functions denoted by parentheses $(\cdot)$. The normalized experimental data points, $\tilde{S}_T$, are calculated in Equation (3.16).

$$\tilde{S}_T = \frac{f_{d,\text{cal}}[T, SoC_A]}{\overline{f}_{d,\text{cal}}[T_{\text{ref}}, SoC_A]} \tag{3.16}$$

Here, the denominator is defined as the arithmetic mean of the degradation factors observed in the reference group ($\overline{f}_{d,\text{cal}}[T_{\text{ref}}, SoC_A]$). Conversely, the numerator utilizes the individual degradation factors of each cell tested at T and SoC_A. Since multiple cells were tested under identical conditions at each test point, this operation preserves the experimental variability, resulting in a distribution of $\tilde{S}_T$ values rather than a single aggregated point. These normalized points serve as the input dataset for fitting the continuous function $S_T(T)$.

Following the establishment of the thermal model $S_T(T)$, the SoC dependency is isolated using Equation (3.17).

$$\tilde{S}_{SoC} = \frac{f_{d,\text{cal}}[T_A, SoC]}{S_T(T_A)} \tag{3.17}$$

In this procedure, the experimental degradation factors $f_{d,\text{cal}}[T_A, SoC]$, obtained at a fixed temperature T_A across the full range of SoC levels, are divided by the specific value of the thermal stress function evaluated at that same temperature, $S_T(T_A)$.

A fundamental distinction in this derivation, compared to the previous thermal analysis, is the absence of normalization by a reference state. By avoiding a relative ratio, the resulting data points $\tilde{S}_{SoC}$ retain the absolute magnitude of the degradation factors. The proportionality constant that dictates the absolute speed of aging over time is inherently absorbed into the magnitude of the $\tilde{S}_{SoC}$ values.

With the thermal function $S_T(T)$ and the SoC function $S_{SoC}(SoC)$ fully parameterized from the calendar aging analysis, the specific calendar contribution during the cycling tests can be quantified. By substituting these fitted continuous functions into the framework established in Equation (3.7), the pure cycle degradation rates for each experimental test point are isolated as presented in Equation (3.18).

$$f_{d,\text{cyc}}[T, SoC, DoD, C] = f^*_{d,\text{cyc}}[T, SoC, DoD, C] - S_T(T)S_{SoC}(SoC)t_{\text{cyc}} \tag{3.18}$$

Having isolated the pure cycle degradation factor $f_{d,\text{cyc}}$, the specific dependencies on C-rate and DoD are determined sequentially. First, the effect of the C-rate is characterized using a normalization strategy. Data points sharing identical fixed conditions for temperature (T_A), mean SoC (SoC_A), and DoD (DoD_A), but varying in C-rate, are selected. These are normalized against the average response observed at a reference C-rate (C_{ref}), yielding the target values $\tilde{S}_C$ for curve fitting. Following a procedure similar to the thermal analysis, this relationship is expressed in Equation (3.19).

$$\tilde{S}_C = \frac{f_{d,\text{cyc}}[T_A, SoC_A, DoD_A, C]}{\overline{f}_{d,\text{cyc}}[T_A, SoC_A, DoD_A, C_{\text{ref}}]} \tag{3.19}$$

Once the continuous function $S_C(C)$ is fitted, the contributions of all known stressors—temperature, SoC, and C-rate—can be factored out from the pure cycle degradation data as shown in Equation (3.20).

$$\tilde{S}_{DoD} = \frac{f_{d,\text{cyc}}[T_A, SoC_A, DoD, C_A]}{S_T(T_A)S_{SoC}(SoC_A)S_C(C_A)} \tag{3.20}$$

While the precise parameterization of the stress functions depends on the empirical trends, the choice of their functional forms is grounded in physical principles. The thermal dependence $S_T(T)$, for instance, typically follows an Arrhenius-type expression [6], mathematically described by Equation (3.21).

$$S_T(T) = A \cdot e^{\left(\frac{B}{T}\right)} \tag{3.21}$$

where A and B are the coefficients of the function.

In general terms, the Arrhenius-type expression takes the form of Equation (3.22).

$$S_T(T) = e^{\left[P_1\left(\frac{1}{T}\right)\right]} \tag{3.22}$$

where P_1 represents a one-degree polynomial of the inverse temperature.

Consistent with the literature, where stress factors are typically modeled as exponentials, the remaining stress functions (S_{SoC}, S_{DoD}, and S_C) follow the general formulation of Equation (3.23).

$$S_x(x) = e^{[P_n(x)]} \tag{3.23}$$

where x represents the specific stressor and P_n denotes a polynomial of degree n. The degree n is selected based on the complexity of the degradation behavior: for stressors exhibiting smooth, monotonic trends, a first-degree polynomial (resulting in a simple exponential) is typically sufficient. Conversely, for factors displaying non-monotonic or highly nonlinear dynamics, higher-degree polynomials are employed. The definitive selection of the polynomial degree and the specific coefficients for each stressor are detailed in the results analysis in Chapter 4.

3.5 HYBRID GPR MODEL

To overcome the limitations of rigid parametric functions and capture complex, multi-dimensional dependencies in aging behavior, this study incorporates GPR. GPR is a non-parametric, Bayesian approach to regression that differs fundamentally from classical curve fitting. Instead of assuming a specific functional form (such as polynomial or Arrhenius) defined by a finite set of parameters, a GP defines a probability distribution over all possible functions that fit the data.

The core of a GP is defined by its mean function and a covariance function, also known as the kernel. The kernel dictates the properties of the function, such as smoothness and periodicity, and determines how the correlation between data points decays as the distance between input variables increases [32]. A key advantage of this method is its probabilistic nature; for every prediction, the GPR provides not only the estimated mean value but also a variance, offering a quantifiable measure of the model's uncertainty.

In the proposed hybrid framework, the deterministic stress functions of the semi-empirical baseline model are replaced by two distinct GP models, as formulated in Equation (3.24).

$$f_d = \sum_{i=1}^{t} t_i \cdot GP_{\text{cal}}(T_i, SoC_i) + \sum_{j=1}^{N} n_j \cdot GP_{\text{cyc}}(T_j, SoC_j, DoD_j, C_j) \tag{3.24}$$

Here, GP_{cal} and GP_{cyc} represent the learned mapping from the operating conditions to the degradation factors. Unlike the baseline approach, which assumes that stress factors are independent and separable (e.g., $S_T(T) \cdot S_{SoC}(SoC)$), the GPR formulation treats the inputs as a joint multi-dimensional space. This allows the model to naturally capture complex interaction effects between variables—such as the synergistic acceleration of aging when high temperature coincides with high SoC—without requiring explicit interaction terms to be manually derived or hard-coded. Despite this data-driven core, the model remains hybrid by preserving the physics-informed structure of the Base SEI Model, the linear damage accumulation (summation over time and cycles) and the distinct separation between calendar and cycle aging mechanisms.

The predictive performance of a GP is fundamentally determined by the choice of its kernel, $k(\mathbf{x}, \mathbf{x}')$, where the input vectors $\mathbf{x}$ and $\mathbf{x}'$ represent distinct sets of operating conditions (e.g., Temperature, SoC). While the Radial Basis Function (RBF) is a common default, it assumes infinite differentiability, often imposing excessive smoothness that can mask rapid changes in degradation trends. To address this, the Matérn 5/2 kernel was selected as the primary component for this study, augmented by a White Noise kernel to account for experimental stochasticity.

The specific choice of the Matérn kernel with the parameter $\nu = 5/2$ provides a crucial advantage for modeling battery aging: it assumes that the underlying function is only twice differentiable. This relaxation of the smoothness constraint allows the model greater flexibility to capture sharper nonlinearities and local irregularities in the stress-response surface. Furthermore, to account for the distinct physical scales and sensitivities of the input variables (e.g., Temperature vs. SoC), the kernel employs Automatic Relevance Determination (ARD). This implies that a distinct length-scale parameter is learned for each dimension. The composite kernel structure is defined as presented in Equation (3.25).

$$k(\mathbf{x}, \mathbf{x}') = \overbrace{\sigma_m^2 \left(1 + \sqrt{5} d_{\mathbf{l}} + \frac{5}{3} d_{\mathbf{l}}^2\right) \exp\left(-\sqrt{5} d_{\mathbf{l}}\right)}^{\text{Matérn 5/2 (ARD)}} + \overbrace{\sigma_n^2 \delta(\mathbf{x}, \mathbf{x}')}^{\text{White Noise}} \tag{3.25}$$

where σ_m^2 is the signal variance of the Matérn kernel, σ_n^2 represents the noise variance, δ is the Kronecker delta. The term $d_{\mathbf{l}}$, with a bold subscript $\mathbf{l}$ to denote the vector of length-scales, represents the anisotropic Euclidean distance derived from the specific length-scale parameter l_k of each input dimension k, as given by Equation (3.26).

$$d_{\mathbf{l}}(\mathbf{x}, \mathbf{x}') = \sqrt{\sum_{k=1}^{D} \frac{(x_k - x_k')^2}{l_k^2}} \tag{3.26}$$

Consistent with the sequential parameterization strategy adopted for the baseline semi-empirical model, the training of the hybrid framework begins with the calendar aging component. The calendar GPR model (GP_{cal}) is trained using the discrete experimental degradation rates $f_{d,\text{cal}}[T, SoC]$ derived directly from the calendar aging tests.

Subsequently, this trained model serves as the baseline to decouple the aging mechanisms in the cycle dataset, as presented in Equation (3.27).

$$f_{d,\text{cyc}}[T, SoC, DoD, C] = f_{d,\text{cyc}}^{*}[T, SoC, DoD, C] - GP_{\text{cal}}(T, SoC) t_{\text{cyc}} \tag{3.27}$$

The resulting dataset $f_{d,\text{cyc}}$ is then utilized to fit the cycle GPR model (GP_{cyc}).

3.6 HYBRID EXPONENTIAL-GPR MODEL

This third modeling strategy incorporates prior physical knowledge regarding the functional form of degradation into the ML framework. Electrochemical aging processes, particularly those driven by temperature and voltage stress, typically exhibit exponential dependencies, such as the Arrhenius law for thermal activation. To leverage this intrinsic behavior, the GPR models in this architecture are designed to estimate the exponent of the degradation function rather than the factor itself. Equation (3.28) mathematically expresses this strategy, defining the total degradation factor through these exponentiated GPR outputs.

$$f_d = \sum_{i=1}^{t} t_i \cdot e^{GP_{\mathrm{cal}}\left(\frac{1}{T_i}, SoC_i\right)} + \sum_{j=1}^{N} n_j \cdot e^{GP_{\mathrm{cyc}}\left(\frac{1}{T_j}, SoC_j, DoD_j, C_j\right)} \tag{3.28}$$

In this formulation, a critical feature engineering step is applied to the input space: the absolute temperature T is transformed into its reciprocal form $1/T$. This transformation linearizes the Arrhenius dependency within the input space of the GP.

To support this exponential structure, the kernel composition is specifically adapted to capture both the dominant global exponential trends and the local nonlinear deviations. The kernel defined in Equation (3.29) is a sum of a Dot-Product kernel, a Matérn 5/2 kernel, and a White Noise kernel.

$$\begin{aligned} k(\mathbf{x}, \mathbf{x}') = & \overbrace{\sigma_d^2 \left(\sigma_0^2 + \mathbf{x} \cdot \mathbf{x}'\right)}^{\text{Dot-Product}} \\ & + \overbrace{\sigma_m^2 \left(1 + \sqrt{5} d_{\mathrm{l}} + \frac{5}{3} d_{\mathrm{l}}^2\right) \exp\left(-\sqrt{5} d_{\mathrm{l}}\right)}^{\text{Matérn 5/2 (ARD)}} \\ & + \underbrace{\sigma_n^2 \delta(\mathbf{x}, \mathbf{x}')}_{\text{White Noise}}, \end{aligned} \tag{3.29}$$

where $\mathbf{x} \cdot \mathbf{x}'$ denotes the dot product between input vectors, σ_0^2 is the inhomogeneity parameter (or bias variance), and σ_d^2 is the signal variance (or scaling factor) of the Dot-Product kernel.

In this composite structure, the Dot-Product term models the global trend. Since the GPR output is exponentiated, the linear hyperplane fitted by this kernel in the logarithmic space corresponds to a global exponential behavior in the degradation space. Simultaneously, the Matérn 5/2 component captures local nonlinearities and complex interactions that deviate from this ideal exponential trend, providing the necessary flexibility to correct the physical approximation.

Due to the exponential formulation of the model, the target variables are transformed into the logarithmic domain. Consequently, the calendar GPR (GP_{cal}) is trained using the natural logarithm of the experimental degradation factors, $\ln(f_{d,\mathrm{cal}}[T, SoC])$.

Subsequently, the trained model is employed to decouple the pure cycle effect from the aggregated observations according to Equation (3.30)

$$f_{d,\mathrm{cyc}}[T, SoC, DoD, C] = f_{d,\mathrm{cyc}}^{*}[T, SoC, DoD, C] - e^{GP_{\mathrm{cal}}\left(\frac{1}{T}, SoC\right)} \cdot t_{\mathrm{cyc}} \tag{3.30}$$

The resulting values are then log-transformed ($\ln(f_{d,\mathrm{cyc}})$) to serve as the training targets for the cycle GPR model (GP_{cyc}).

3.7 MODEL EVALUATION FRAMEWORK

The assessment of the proposed degradation models is conducted in two complementary stages. Initially, a qualitative analysis of the interpolation and extrapolation capabilities is performed as the stress functions are fitted. Given the constraints of a limited experimental dataset, this visual inspection is crucial to verify if the models exhibit physically consistent behavior outside the training points—such as monotonic degradation trends—serving as a preliminary validation to support the goodness-of-fit discussion.

For the quantitative validation, the fully parameterized stress models—Semi-Empirical, Hybrid GPR, and Hybrid Exponential-GPR—are integrated back into the governing Q equations. Using the global parameters α_{sei} and β_{sei} determined in the baseline analysis, the predicted capacity fade is calculated using the respective model formulations (Equations (3.4) and (3.6)). The predictive accuracy is then evaluated against both the calendar aging dataset and the cycle aging dataset.

To quantify the performance, the Normalized Root Mean Square Error (nRMSE) is adopted as the primary metric. The global error is calculated using Equation (3.31).

$$\text{nRMSE} = \frac{1}{Q_{\text{range}}}\sqrt{\frac{1}{N}\sum_{i=1}^{N}(Q_{\text{exp},i} - Q_{\text{pred},i})^2} \cdot 100\% \tag{3.31}$$

where Q_{exp} and Q_{pred} are the experimental and predicted capacity values, respectively. N is the number of data points, and Q_{range} represents the functional capacity window of interest. For this study, Q_{range} is defined as the span between 100% and 80%, which corresponds to the useful life of the battery.

The selection of the nRMSE metric is driven by two specific methodological advantages:

1. Sensitivity to Outliers: By squaring the residuals, the RMSE component inherently penalizes larger deviations more severely than smaller ones. This is particularly important for degradation modeling, where stability and reliability are paramount, and large local errors are undesirable.

2. Contextual Interpretation: By normalizing the error against the specific 20% operational window (100%–80%) rather than the total capacity, the metric provides a direct percentage of the usable life error. This offers a more practical understanding of the model's precision relative to the application's EOL criteria.

3.8 COMPUTATIONAL FRAMEWORK AND SIMULATION TOOLS

All simulations, data processing, and model implementations conducted in this study were developed using the Python programming language. The computational framework leveraged a robust ecosystem of open-source libraries, following a systematic sequence of computational steps to ensure reproducibility:

- **Data Processing:** Initial feature extraction, data filtering, and data cleaning were performed utilizing the *Pandas* and *NumPy* libraries.
- **Primary Parameter Identification:** To determine the global constants α_{sei} and β_{sei} a nonlinear least squares optimization was executed using the `curve_fit` function from the `scipy.optimize` module.
- **Secondary Degradation Factors:** Following the determination of α_{sei} and β_{sei}, a subsequent round of optimization using `curve_fit` was applied to the dataset to extract the specific calendar and cycling degradation factors, namely $f_{d,\mathrm{cal}}$ and $f^*_{d,\mathrm{cyc}}$.
- **Semi-Empirical Parametric Fitting:** The parameters for the parametric functions of the Semi-Empirical Model were fitted utilizing the *Statsmodels* library, specifically via Ordinary Least Squares regression (`statsmodels.api.OLS`). Since the underlying empirical functions are structured as exponentials of polynomials, the natural logarithm of the target values was applied prior to the polynomial fitting. This module was particularly selected because it inherently computes and provides the statistical confidence intervals for all estimated parameters.
- **Hybrid GPR Implementation:** The data-driven models, encompassing both the Hybrid GPR and the Hybrid Exponential-GPR, were implemented using the *Scikit-learn* library (`sklearn`). Specifically, the `GaussianProcessRegressor` class from the `sklearn.gaussian_process` module was utilized. This module provides a highly flexible framework that allows for the combination of distinct kernel functions, automatic hyperparameter tuning via Maximum Likelihood Estimation (MLE), and the analytical computation of both the predictive mean and the predictive uncertainty (standard deviation) simultaneously.
- **Performance Evaluation and Error Metrics:** To quantify the goodness-of-fit of the models, their generated outputs were systematically compared against the experimental dataset. The evaluation methodology was designed to be highly flexible, allowing the nRMSE to be calculated across various data granularities. Depending on the analysis requirement, the error could be assessed for a specific isolated test point (e.g., constant stress factors over time), broader subsets comprising exclusively calendar or cycling aging data, or the entire comprehensive dataset. All statistical error metrics were computed utilizing the `sklearn.metrics` module.

- **Data Visualization and Analysis:** Finally, all data visualization, and plotting of simulation results were generated utilizing the *Matplotlib* library.

3.9 SUMMARY

In summary, this chapter presented a comprehensive methodological framework designed to address the limitations of purely empirical and purely data-driven battery degradation models. By establishing a deterministic Semi-Empirical base, the physics of the aging process are preserved. Subsequently, the introduction of the Hybrid GPR and the Hybrid Exponential-GPR models provides a structured mechanism to capture the complex, nonlinear residuals that traditional parametric equations fail to map.

The careful selection of the composite kernel architecture and the definition of a rigorous validation strategy ensure that the models are evaluated not only on their fitting accuracy but also on their physical consistency during extrapolation. Furthermore, the definition of a robust Python-based computational framework ensures the reproducibility and efficiency of all developed simulations. With the methodological foundations mathematically defined and the experimental dataset properly structured, the following chapter will present the application of these models and deeply analyze their predictive performance.

4 RESULTS

This chapter presents the results obtained from applying the proposed modeling framework to the aging dataset. The analysis is organized into three main stages:

- **Base SEI Model Identification:** Identification of global parameters to establish a common foundation for all modeling approaches.
- **Model Parameterization and Training:** Presentation of the training results for the Semi-Empirical, Hybrid GPR, and Hybrid Exponential-GPR models.
- **Comparative Performance Evaluation:** Assessment of physical consistency and predictive accuracy. The quantitative analysis covers three scopes:
  - **Calendar Aging Assessment:** Isolated evaluation using the calendar test set to determine specific nRMSE metrics.
  - **Cycle Aging Assessment:** Isolated evaluation using cycling tests to measure performance under dynamic degradation.
  - **Global Assessment:** A combined evaluation of both datasets to establish overall global error metrics.

4.1 BASE SEI MODEL

As outlined in the methodology, the parameters α_{sei} and β_{sei} were first estimated individually for every specific test condition available in the experimental campaign. This approach prevents the bias associated with selecting a single arbitrary condition for calibration and captures the distribution of parameter estimates across the entire operational space.

To define the global model constants, the median of the resulting distributions was selected. This estimator was chosen due to its robustness against outliers, which are expected in large-scale experimental campaigns due to cell-to-cell variability and measurement noise. The determined global parameters are: $\alpha_{\text{sei}} = 0.0182$ and $\beta_{\text{sei}} = 219.77$.

To assess the reliability of these estimates and quantify the uncertainty associated with the median, a bootstrap analysis was performed. The procedure involved generating $B = 5000$ bootstrap samples by resampling the original parameter distributions with replacement. For each resampled dataset, the median was re-calculated, generating an empirical distribution of the estimator.

The 95% confidence intervals (CI) were derived using the percentile method, yielding the bounds within which the true median is expected to lie with 95% probability. The analysis resulted in a CI of $[0.0149, 0.0199]$ for α_{sei} and $[189.3, 244.0]$ for β_{sei}. These narrow intervals, particularly for the α_{sei} parameter which governs the split between the fast and slow aging dynamics, confirm the stability of the global parameterization strategy.

4.2 SEMI-EMPIRICAL DEGRADATION FACTOR MODEL

The parameterization of the semi-empirical model begins with the isolation of the thermal stress function, $S_T(T)$. As detailed in the methodology, the normalized degradation factors derived from the calendar aging dataset were analyzed to determine the temperature dependency, establishing the reference temperature (T_{ref}) at 23 °C.

The experimental data exhibits a distinct Arrhenius behavior. Figure 5 illustrates this relationship, showing how the natural logarithm of the normalized stress factor ($\ln(S_T)$) varies with the inverse of the absolute temperature ($1/T$) while maintaining the SoC constant at 50%. In this plot, the solid blue line represents the linear fit ($P_1(1/T)$) to the log-transformed data, while the shaded region indicates the 95% confidence interval.

Figure 5 – Arrhenius plot characterizing the thermal stress function $S_T(T)$ at a constant SoC of 50%.

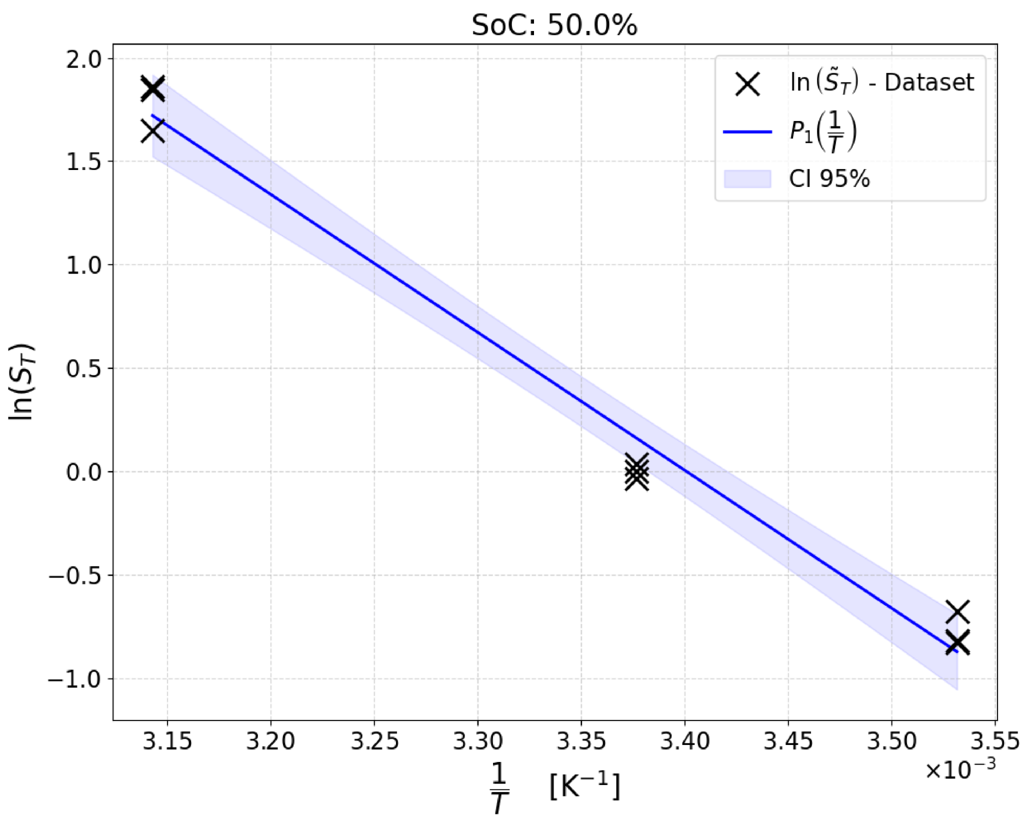

Source: Elaborated by the author.

Therefore, the thermal stress function is mathematically modeled as expressed in Equation (4.1).

$$S_T(T) = \exp\left(p_0 + \frac{p_1}{T}\right) . \tag{4.1}$$

Table 2 summarizes the fitted parameters, including the intercept (p_0) and the slope (p_1), alongside their respective 95% confidence intervals (CI).

Table 2 – Fitted parameters for the thermal stress function $S_T(T)$.

Parameter	**Value**	**[0.025**	**0.975]**
p_0	22.71	20.18	25.25
p_1	-6677.77	-7433.45	-5922.09

Source: Elaborated by the author.

Following the thermal analysis, the dependency on SoC was characterized. This was achieved by analyzing the calendar aging dataset while holding the temperature constant at 23°C, thereby isolating the electrochemical stress associated exclusively with the storage SoC.

Figure 6 presents the $\tilde{S}_{SoC}$ values extracted from the experimental data. A visual inspection reveals a highly nonlinear and non-monotonic relationship.

Figure 6 – Degradation factor as a function of SoC at 23°C.

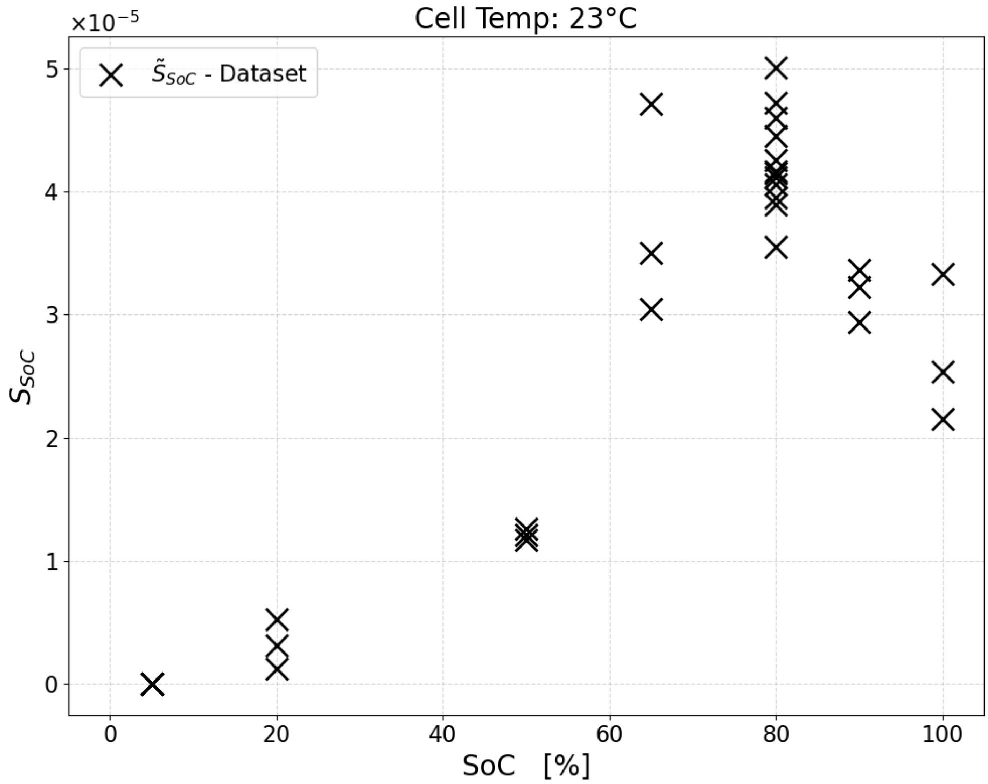

Source: Elaborated by the author.

This observed complexity contrasts significantly with the original semi-empirical framework proposed by [6], which approximated the SoC dependency using a simple monotonic exponential function. As evidenced by the data, such a simplification is insufficient for capturing the specific aging dynamics of the INR21700-50E chemistry under study.

To accurately model this behavior, polynomial functions of varying degrees were evaluated within the logarithmic space. Figure 7 illustrates the fit of the selected function. Third, fourth, and fifth-degree polynomials were tested to find the optimal balance between complexity and fidelity. The selection was driven by the coefficient of determination (R^2), which yielded values of 0.953, 0.985, and 0.993, respectively. Consequently, the fifth-degree polynomial was selected as it provides the most accurate representation of the degradation features.

Figure 7 – Fit of the 5th-degree polynomial function $P_5(SoC)$ to the log-transformed data.

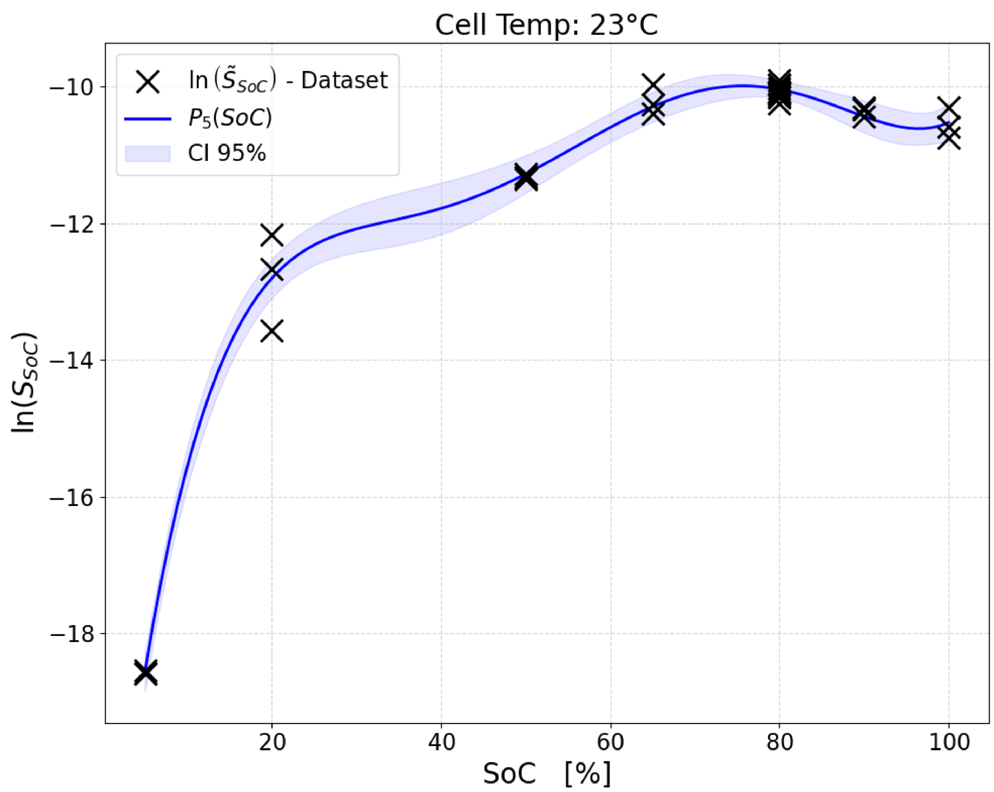

Source: Elaborated by the author.

Equation (4.2) shows the form of $S_{SoC}(SoC)$.

$$S_{SoC}(SoC) = \exp\Big(p_5 SoC^5 + p_4 SoC^4 + p_3 SoC^3 + p_2 SoC^2 + p_1 SoC + p_0\Big) \tag{4.2}$$

The fitted coefficients for this polynomial are detailed in Table 3, including their 95% confidence intervals.

Table 3 – Fitted parameters for the SoC stress function $S_{SoC}(SoC)$.

Parameter	**Value**	**[0.025**	**0.975]**
p_0	-23.30	-24.11	-22.49
p_1	116.04	97.70	134.39
p_2	-470.76	-586.80	-354.71
p_3	920.11	632.60	1207.62
p_4	-833.79	-1137.53	-530.05
p_5	281.17	166.30	396.04

Source: Elaborated by the author.

With the calendar aging effects (S_T and S_{SoC}) fully characterized, the analysis proceeds to the cycle aging dataset. The first dynamic stressor evaluated is the C-rate (S_C).

Unlike the calendar aging study, the cycle aging experiments were not conducted using a full factorial design. Consequently, strictly isolating the effect of C-rate by holding all other variables constant was not feasible. To mitigate this, a specific region of the experimental space was selected to maximize the density of distinct C-rate data points while keeping other stressors within a controlled tolerance. The selected window was defined by a cell temperature of 50.6 ± 5.0°C, a SoC of $50.0 \pm 5.0\%$, and a DoD of $60.0 \pm 5.0\%$. Figure 8 displays the normalized degradation factors $\tilde{S}_C$ within this region.

Figure 8 – Normalized degradation factor as a function of C-rate.

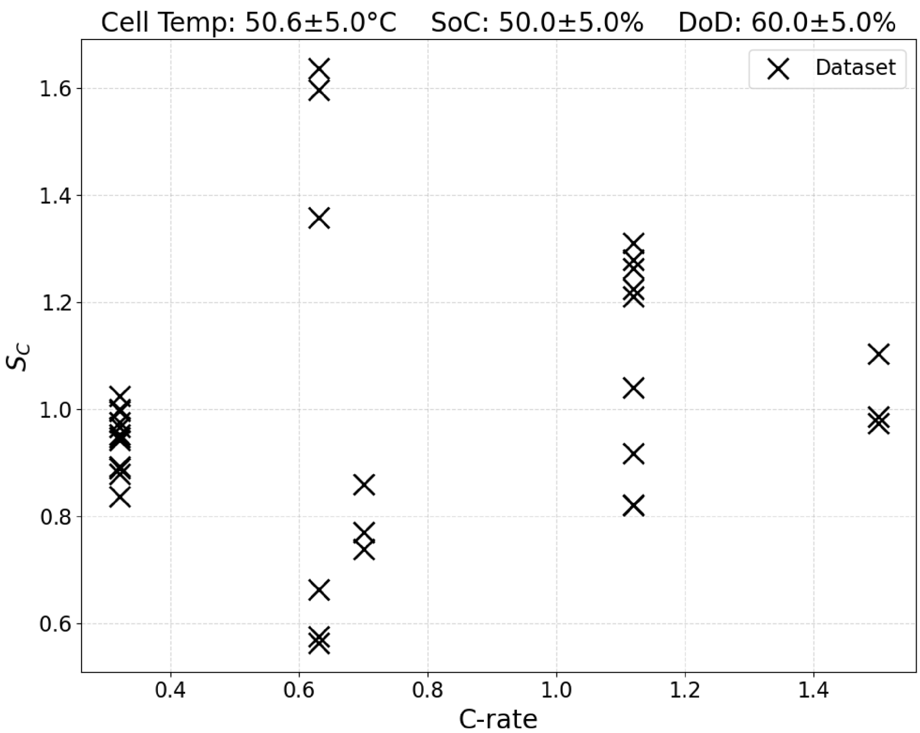

Source: Elaborated by the author.

A visual inspection reveals the absence of a clear functional trend relating degradation magnitude to C-rate. Notably, for specific C-rates such as 0.63 C, there is a significant dispersion in the degradation values. This variability is attributed to the unavoidable minor fluctuations of the other stress factors (T, SoC, DoD) within the allowed tolerance window, rather than the current magnitude itself.

This behavior reinforces the hypothesis presented by the original authors of the semi-empirical model [6], who explicitly excluded C-rate from their degradation function. Their rationale posited that the primary impact of higher C-rates is the elevation of the cell's internal temperature—an effect already captured by the thermal stress function $S_T(T)$—rather than a direct electrochemical degradation mechanism driven by the current flux. The data presented here supports this view, exhibiting a behavior that is essentially constant ($\ln(S_C) \approx 0$, implying $S_C \approx 1$).

For the sake of completeness and to maintain the consistency of the mathematical framework, an exponential function with a linear polynomial argument was fitted to the log-transformed data, as shown in Figure 9.

Figure 9 – Fit of the linear polynomial function $P_1(C)$ to the log-transformed C-rate data.

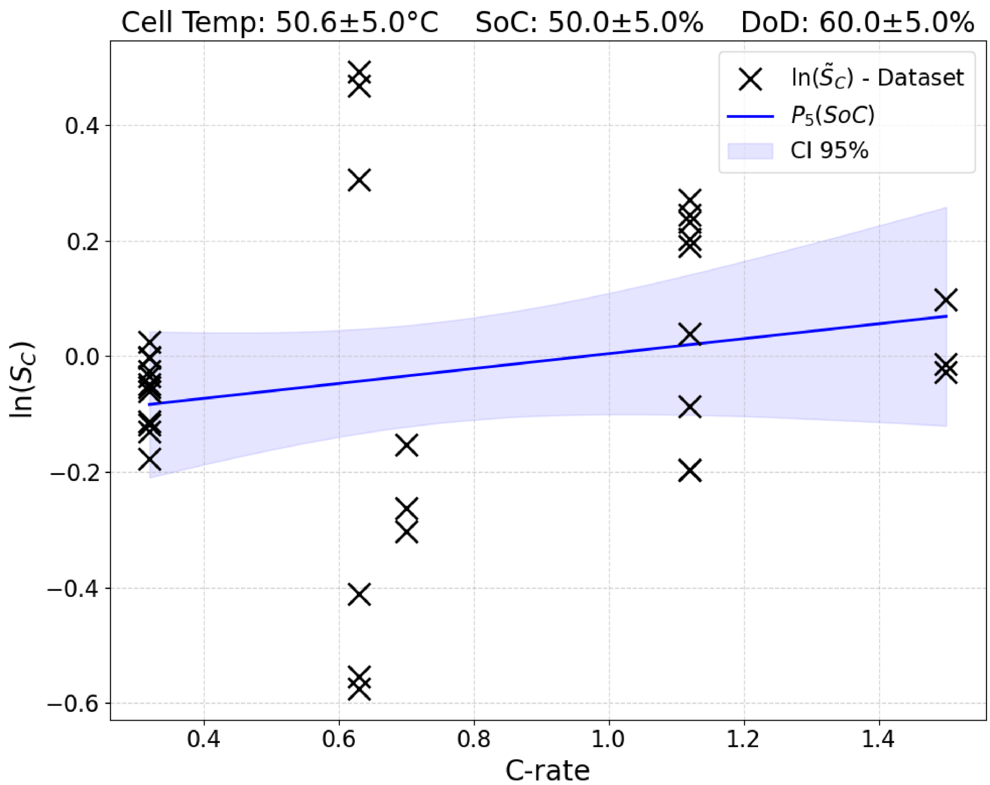

Source: Elaborated by the author.

This relationship is mathematically formalized in Equation (4.3).

$$S_C(C) = \exp\left(p_1 C + p_0\right) \tag{4.3}$$

The fitted parameters are listed in Table 4. As anticipated from the visual analysis, the slope (p_1) is small, and its confidence interval crosses zero, statistically confirming that the C-rate does not act as a significant independent driver of degradation in this model.

Table 4 – Fitted parameters for the C-rate stress function $S_C(C)$.

Parameter	**Value**	**[0.025**	**0.975]**
p_0	-0.1248	-0.309	0.059
p_1	0.1291	-0.090	0.349

Source: Elaborated by the author.

Finally, the impact of DoD (S_{DoD}) was evaluated. Leveraging the previous finding that the C-rate exerts negligible influence on the degradation factor ($S_C \approx 1$), the constraint on current magnitude was relaxed for this analysis. Consequently, the dataset was expanded to include test points across all C-rates within the sampling region defined by a temperature of 41.0 ± 5.0°C and a SoC of 45.0 ± 5.0%. This approach significantly increased the density of available data points, ensuring a more robust fit.

Figure 10 presents the normalized degradation factors plotted against DoD in the logarithmic domain.

Figure 10 – Fit of the linear polynomial function $P_1(DoD)$ to the log-transformed data.

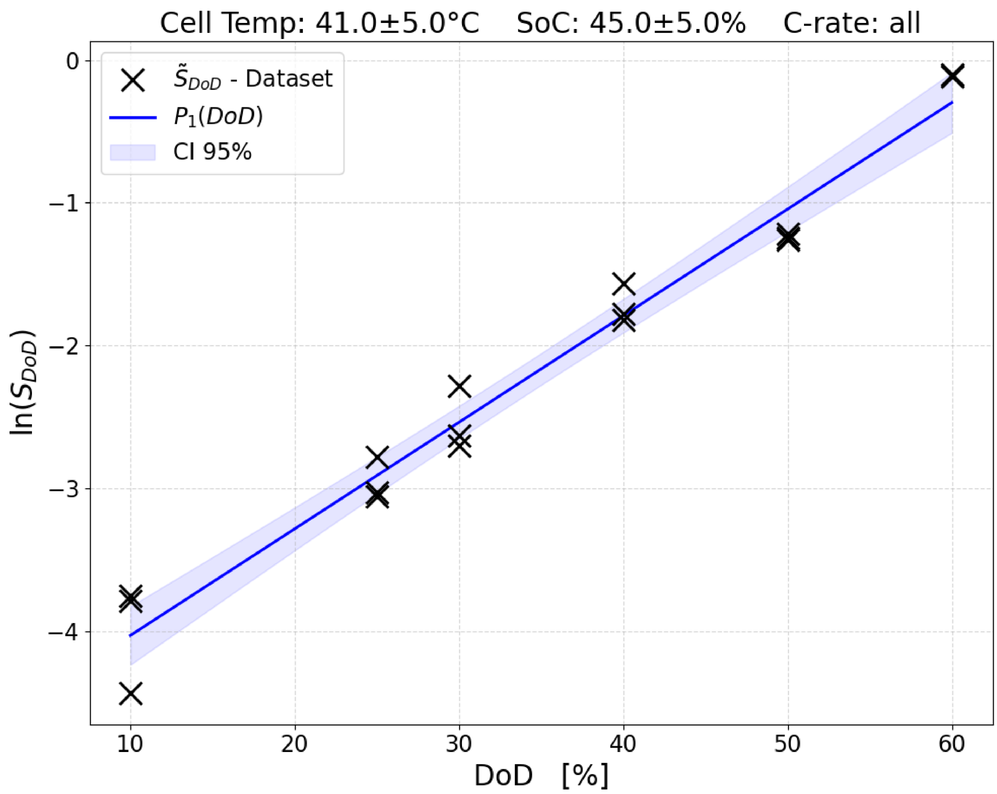

Source: Elaborated by the author.

The data exhibits a distinct linear trend, confirming that the degradation severity grows exponentially with the depth of the cycle. Accordingly, a first-degree polynomial was fitted to the log-transformed data, yielding the stress model presented in Equation (4.4).

$$S_{DoD}(DoD) = \exp\left(p_1 DoD + p_0\right) \tag{4.4}$$

The specific coefficients determined for this function are listed in Table 5. The narrow confidence intervals for the slope (p_1) confirm the strong statistical significance of the DoD influence, in marked contrast to the C-rate analysis.

Table 5 – Fitted parameters for the DoD stress function $S_{DoD}(DoD)$.

Parameter	**Value**	**[0.025**	**0.975]**
p_0	-4.7778	-5.044	-4.511
p_1	7.4640	6.760	8.168

Source: Elaborated by the author.

4.3 HYBRID GPR MODEL

Following the definition of the hybrid framework in Equation (3.24), the calendar GPR model, $GP_{\text{cal}}(T, SoC)$, was trained to learn the mapping between the stressors and the degradation factor $f_{d,\text{cal}}$.

The resulting optimized parameters are detailed in Table 6.

Table 6 – Optimized hyperparameters of the GP_{cal} in the Hybrid GPR Model.

Kernel Component	**Hyperparameter**	**Value**
Matérn 5/2	Signal Amplitude (σ_m)	1.030
	Length-scale: Temperature (l_T)	1.570
	Length-scale: SoC (l_{SoC})	0.422
White Noise	Noise Variance (σ_n^2)	0.012

Source: Elaborated by the author.

A notable feature of the optimization is the difference between the length-scales. The length-scale for temperature ($l_T = 1.57$) is larger than that for the SoC ($l_{SoC} = 0.422$). In the context of GPs, a larger length-scale implies a smoother function where correlation decays slowly with distance, whereas a smaller length-scale allows for more rapid variations. This data-driven finding aligns perfectly with the physical phenomena observed in the semi-empirical analysis: the thermal dependency is a smooth, monotonic Arrhenius trend, whereas the SoC dependency is complex and highly variable.

The predictive behavior of the trained GP_{cal} model is visualized in Figures 11 and 12.

Figure 11 displays the model's response to temperature variations while the SoC is held constant at 50%. The model successfully learns the nonlinear, monotonic increase in degradation rates associated with thermal effect. The 95% CI (shaded red region) remains relatively uniform across the temperature range, reflecting the consistent behavior of the degradation trend in this dimension.

Figure 11 – Response of the GP_{cal} model as a function of temperature (fixed SoC = 50%).

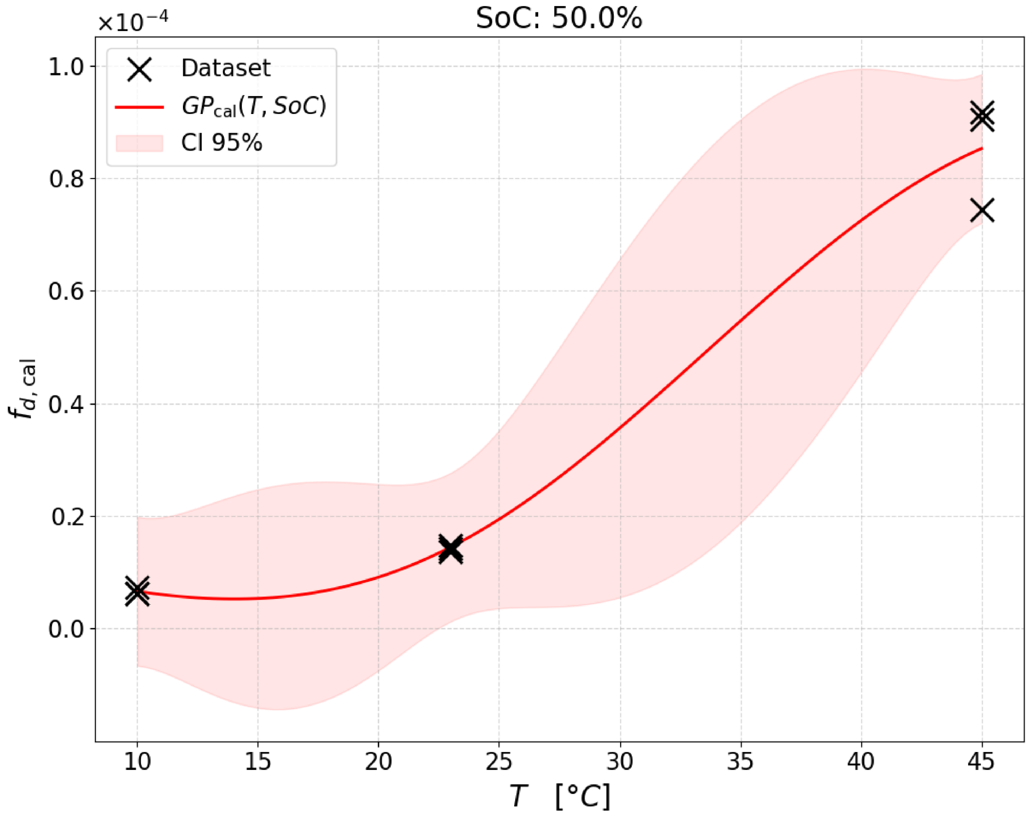

Source: Elaborated by the author.

In contrast, Figure 12 illustrates the model's behavior across the SoC range at a fixed temperature of 23°C. Here, the flexibility of the non-parametric approach is evident. The mean function (solid red line) accurately traces the non-monotonic local maxima and minima, without forcing a simplified exponential shape.

Crucially, this plot also demonstrates the probabilistic nature of the GPR. In regions where experimental data is sparse—specifically the intervals between 20%–50% SoC—the confidence intervals expand significantly. This behavior indicates that the model correctly identifies and quantifies the lack of information in these untrained regions, preventing overconfident predictions in areas of high uncertainty.

Subsequently, the cycle GPR model, $GP_{\text{cyc}}(T, SoC, DoD, C)$, was trained using

Figure 12 – Response of the GP_{cal} model as a function of SoC (fixed T = 23°C).

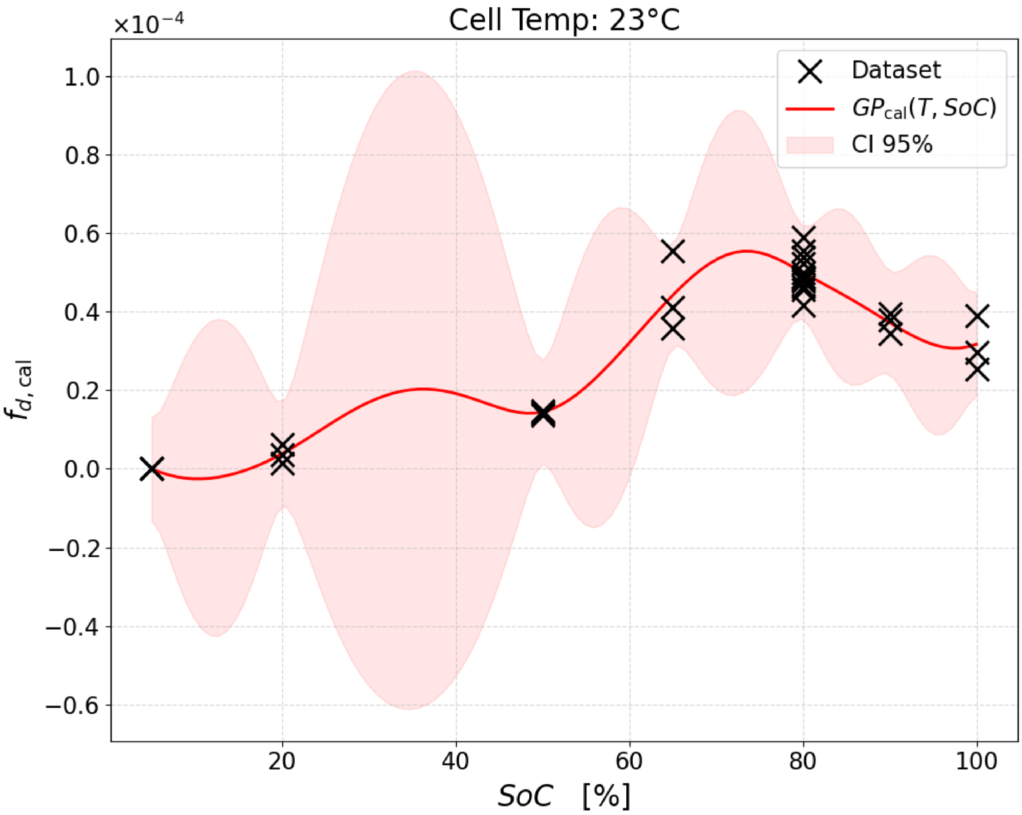

Source: Elaborated by the author.

the pure cycle degradation factors isolated via Equation (3.27). The hyperparameters optimized for this four-dimensional input space are presented in Table 7.

Table 7 – Optimized hyperparameters of the GP_{cyc} in the Hybrid GPR Model.

Kernel Component	**Hyperparameter**	**Value**
Matérn 5/2	Signal Amplitude (σ_m)	2.100
	Length-scale: Temperature (l_T)	8.330
	Length-scale: SoC (l_{SoC})	7.220
	Length-scale: DoD (l_{DoD})	2.640
	Length-scale: C-rate (l_C)	1.22×10^5
White Noise	Noise Variance (σ_n^2)	0.092

Source: Elaborated by the author.

A significant finding from this optimization lies in the length-scale associated with the C-rate (l_C). The optimizer converged to an extremely large value (1.22×10^5), which is orders of magnitude higher than those for the other dimensions. A length-scale approaching infinity implies that the correlation between data points does not decay with distance along that specific axis. Consequently, the GP views the degradation function as effectively constant with respect to C-rate.

This data-driven result provides statistical corroboration of the semi-empirical analysis. Without any manual feature selection or forced exclusion, the GPR independently determined that the C-rate is a negligible driver of degradation for this specific dataset, while correctly identifying DoD ($l_{DoD} = 2.64$) as a highly relevant stressor.

The practical implication of this parameterization is visualized in Figure 13. The model prediction is a flat line, confirming the lack of sensitivity to current magnitude. The wide confidence intervals reflect the high noise variance ($\sigma_n^2 = 0.092$) inherent to the cycle dataset, which arises from the non-factorial nature of the experimental design.

Figure 13 – Response of the GP_{cyc} model as a function of C-rate.

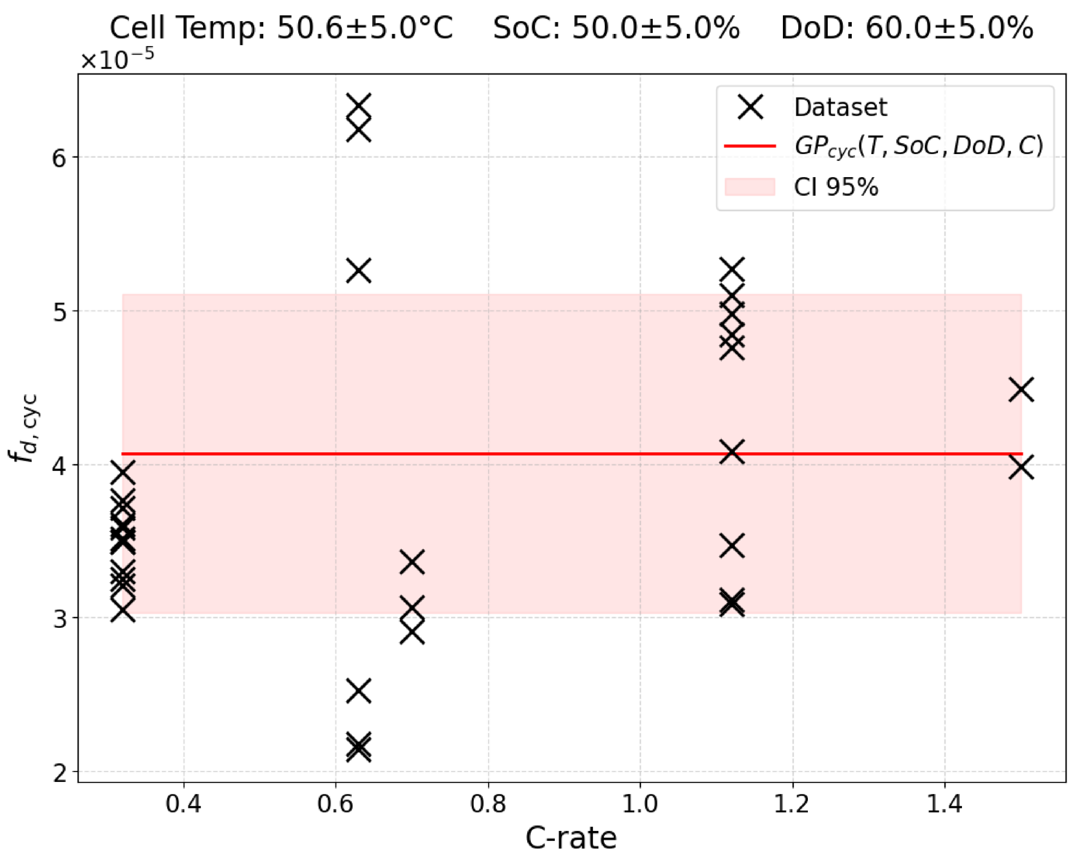

Source: Elaborated by the author.

Conversely, Figure 14 illustrates the model's behavior regarding DoD. Here, the model captures a clear increasing trend, validating the physical expectation that deeper cycles induce greater degradation. However, the high uncertainty (wide confidence bands) highlights the sparsity of training data, alerting the user to potential lower reliability when extrapolating.

Figure 14 – Response of the GP_{cyc} model as a function of DoD.

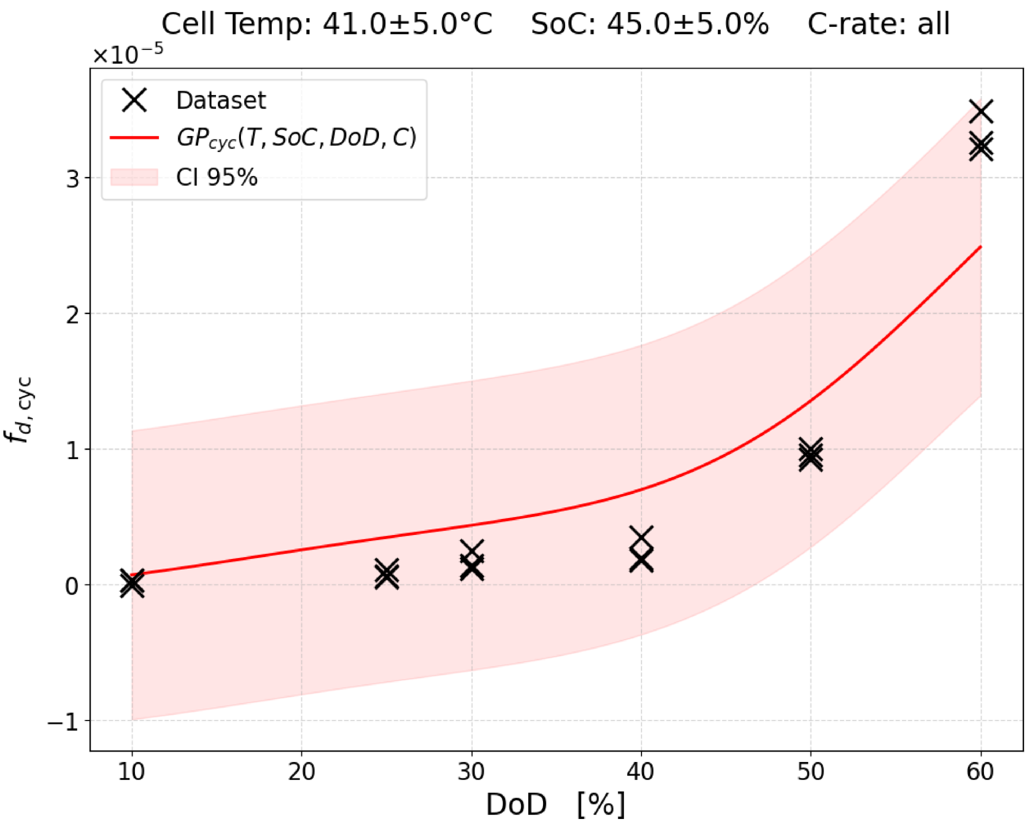

Source: Elaborated by the author.

4.4 HYBRID EXPONENTIAL-GPR MODEL

The third modeling strategy incorporates the physical knowledge of degradation directly into the regression structure. As defined in Equation (3.28), the GP_{cal} model is trained to predict the natural logarithm of the degradation factor, $\ln(f_{d,\mathrm{cal}})$, utilizing the inverse temperature ($1/T$) and SoC as inputs.

The hyperparameters for the composite kernel—comprising a Dot-Product kernel to capture global trends and a Matérn 5/2 kernel for local nonlinearities—were optimized as shown in Table 8.

A critical result of this optimization is the value of the length-scale associated with temperature (l_T) in the Matérn component. The optimizer converged to a large length-scale (2.54×10^8), effectively rendering the Matérn kernel insensitive to the temperature dimension.

This behavior has a profound physical interpretation. It indicates that the Dot-Product kernel, which models a linear plane in the feature space, is fully sufficient to describe the thermal dependency. Since the input space transforms temperature as $1/T$ and the target is logarithmic, a linear relationship here corresponds exactly to the Arrhenius

Table 8 – Optimized hyperparameters of the GP_{cal} in the Hybrid Exponential-GPR Model.

Kernel Component	**Hyperparameter**	**Value**
Dot-Product	Signal Amplitude (σ_d)	0.518
	Inhomogeneity (σ_0)	2.54×10^{-7}
Matérn 5/2	Signal Amplitude (σ_m)	0.685
	Length-scale: Temp (l_T)	2.54×10^{8}
	Length-scale: SoC (l_{SoC})	0.420
White Noise	Noise Variance (σ_n^2)	0.045

Source: Elaborated by the author.

structure. The fact that the nonlinear Matérn component became inactive confirms that there are no significant deviations from the theoretical Arrhenius behavior in the dataset.

This is visually confirmed in Figure 15. The model prediction (green line) forms a perfect straight line in the plot, demonstrating that the Exponential-GPR successfully enforces the physically correct decay rate, which is crucial for plausible extrapolation beyond the tested temperature range.

Figure 15 – Response of the Hybrid Exponential-GPR Model as a function of inverse temperature.

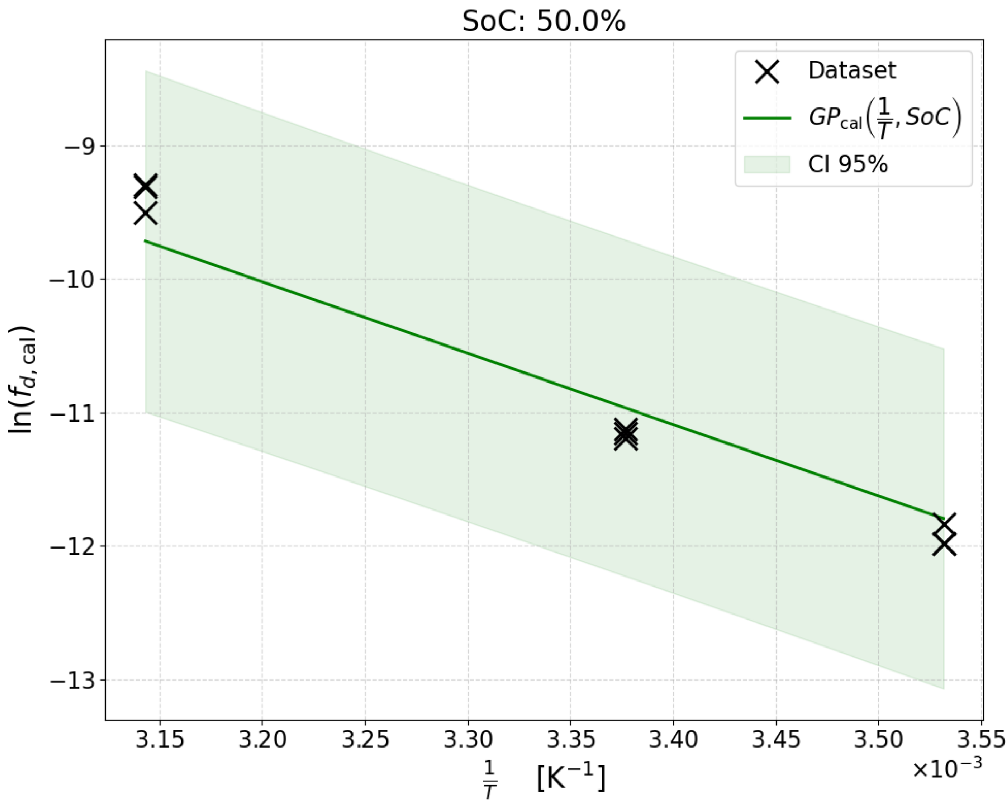

Source: Elaborated by the author.

Conversely, the Matérn kernel in the SoC remains highly active with a short length-scale ($l_{SoC} = 0.420$). As shown in Figure 16, this allows the model to superimpose the complex, nonlinear effects onto the global trend. The result is a model that is smooth and physics-compliant in the temperature dimension, yet flexible and data-driven in the SoC dimension.

Figure 16 – Response of the Hybrid Exponential-GPR Model as a function of SoC.

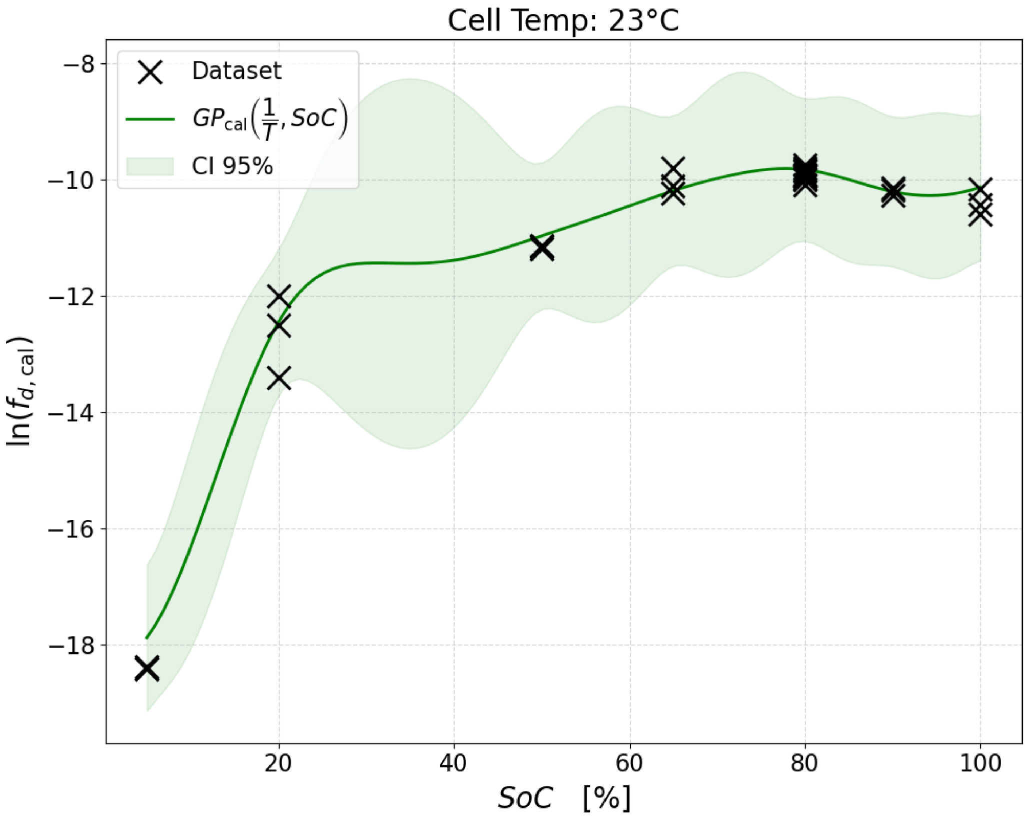

Source: Elaborated by the author.

Finally, the cycle GPR model for the exponential framework, $GP_{\text{cyc}}(1/T, SoC, DoD, C)$, was trained on the log-transformed pure cycle degradation factors. The optimized hyperparameters are presented in Table 9.

Table 9 – Optimized hyperparameters of the GP_{cyc} in the Hybrid Exponential-GPR Model.

Kernel Component	**Hyperparameter**	**Value**
Dot-Product	Signal Amplitude (σ_d)	0.373
	Inhomogeneity (σ_0)	6.23×10^{-10}
Matérn 5/2	Signal Amplitude (σ_m)	0.873
	Length-scale: Temp (l_T)	2.26
	Length-scale: SoC (l_{SoC})	1.22
	Length-scale: DoD (l_{DoD})	6.37×10^{4}
	Length-scale: C-rate (l_C)	3.69×10^{3}
White Noise	Noise Variance (σ_n^2)	0.041

Source: Elaborated by the author.

In this case, the length-scales associated with DoD ($l_{DoD} = 6.34 \times 10^4$) and C-rate ($l_C = 3.69 \times 10^3$) are orders of magnitude larger than those for temperature and SoC. Once again, considering the composite kernel architecture, such high length-scales imply that the Matérn component is effectively inactive for these two dimensions. Consequently, the model relies almost exclusively on the Dot-Product kernel to describe the dependencies.

For the C-rate, this behavior confirms the previous findings regarding its negligible impact. As shown in Figure 17, the model predicts a nearly flat linear response in the logarithmic space. Mathematically, the exponential of a constant (or near-constant) value results in a constant degradation factor ($e^c \approx k$). Thus, despite the exponential structure of the model framework, the data-driven optimization correctly identifies that the C-rate does not drive an exponential increase in aging, yielding a physically consistent constant response compatible with the results of the other modeling strategies.

Figure 17 – Response of the Hybrid Exponential-GPR Model as a function of C-rate.

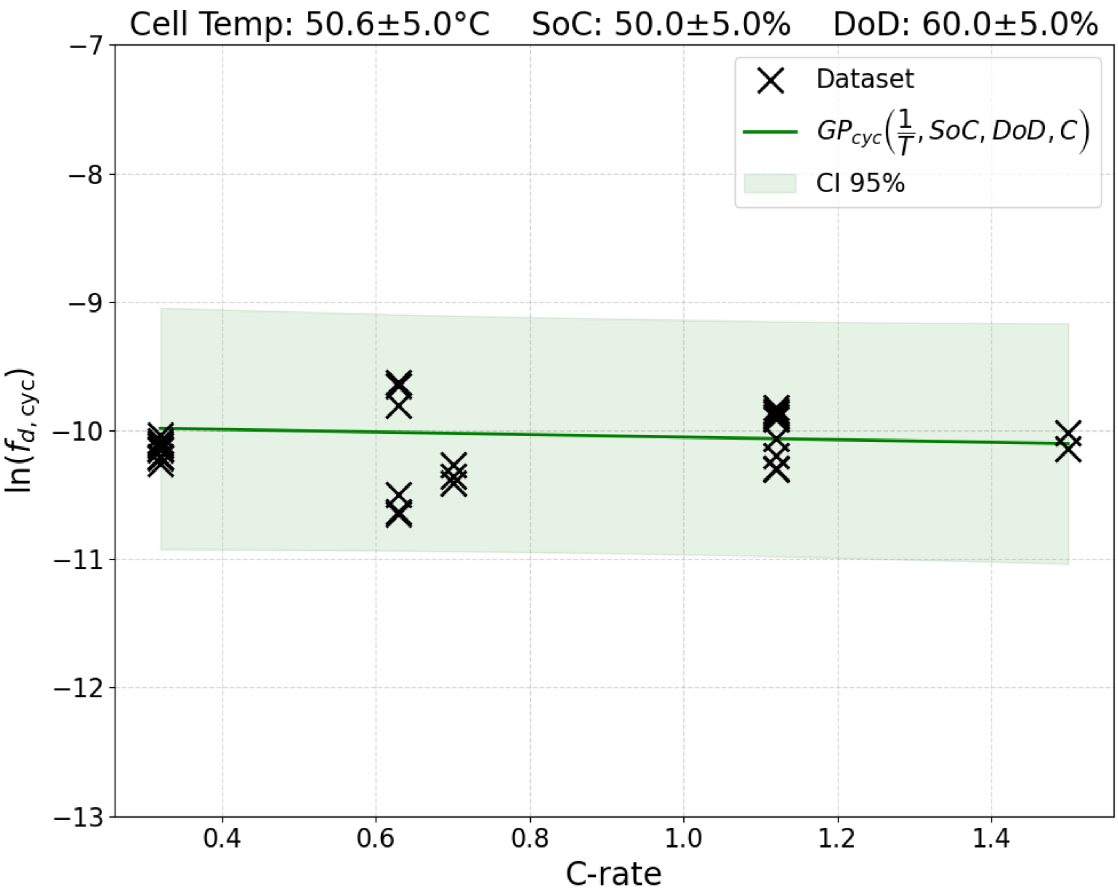

Source: Elaborated by the author.

Conversely, for DoD, the dominance of the Dot-Product kernel validates the physical assumption. Figure 18 illustrates a linear trend in the logarithmic domain. When transformed back to the physical domain by the model's exponential output function, this log-linear relationship corresponds to an exponential acceleration of aging ($e^{k \cdot DoD}$). This confirms that the Hybrid Exponential-GPR successfully captures the expected degradation without requiring the manual prescription of the functional form.

Figure 18 – Response of the Hybrid Exponential-GPR model as a function of DoD.

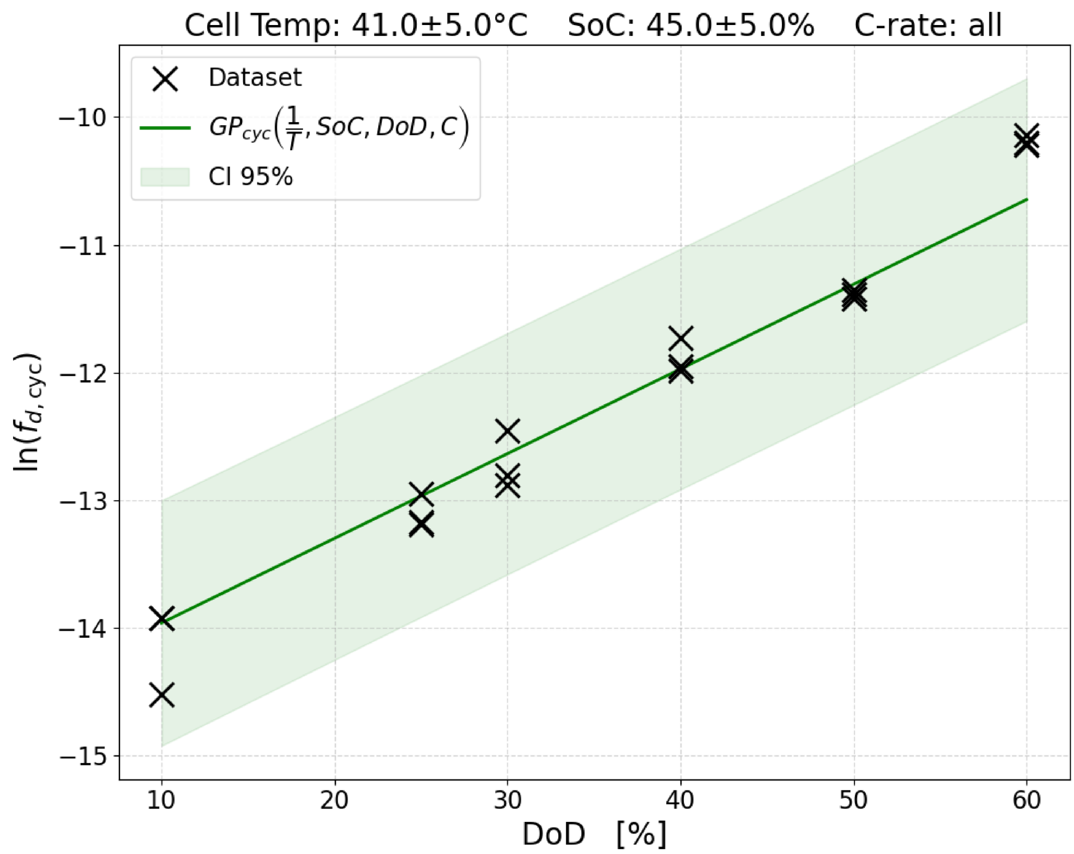

Source: Elaborated by the author.

4.5 QUALITATIVE ANALYSIS

Before quantifying the global error metrics, a qualitative assessment of the models' physical consistency is essential. This analysis focuses on the ability of each framework to capture governing degradation trends (interpolation) and strictly adhere to physical laws outside the training domain (extrapolation).

Figure 19 compares the predicted calendar degradation factor ($f_{d,\mathrm{cal}}$) as a function of temperature, with the SoC fixed at 50%. This specific slice of the operational space highlights the fundamental structural differences between the three modeling strategies.

The Semi-Empirical Model (blue line) exhibits a smooth, monotonic exponential growth. This behavior is expected, as the 50% SoC condition was the specific dataset used to fit the Arrhenius parameters for the S_T function. Consequently, the model aligns well with the experimental data points.

Figure 19 – Comparison of the predicted degradation factor $f_{d,\text{cal}}$ as a function of temperature (fixed SoC = 50%). The vertical dashed line marks the limit of the training data (45°C).

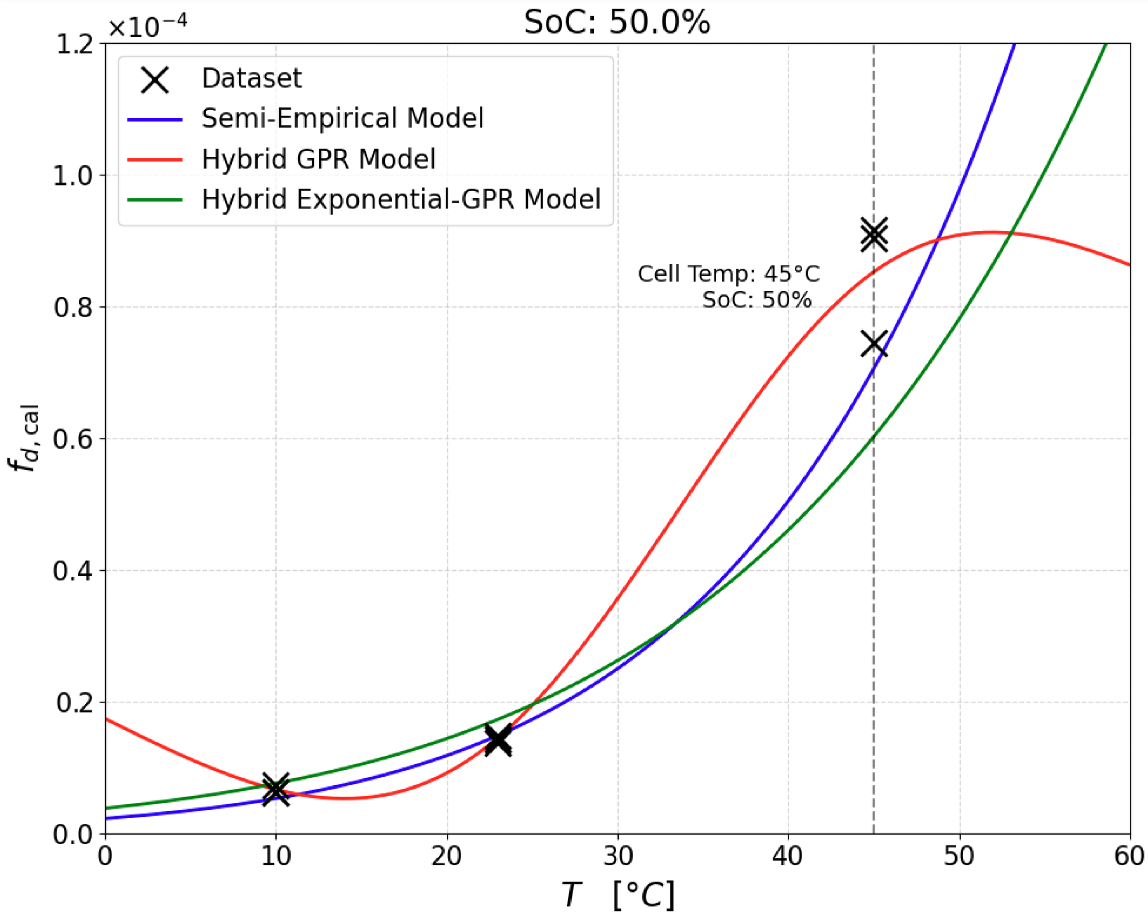

Source: Elaborated by the author.

The Hybrid GPR Model (red line) demonstrates the highest flexibility, passing almost perfectly through the experimental observations at 10°C, 23°C, and 45°C. However, this flexibility introduces physical inconsistencies. In the interpolation region, the curve exhibits oscillatory behavior. More critically, in the extrapolation region ($T > 45$°C), the degradation rate paradoxically decreases. This phenomenon is a characteristic artifact of the Matérn kernel: in the absence of data, the GP tends to revert to its prior mean. While statistically valid, this behavior is thermodynamically impossible, as degradation reactions invariably accelerate with temperature.

Conversely, the Hybrid Exponential-GPR Model (green line) prioritizes physical structure over local precision. At the 45°C test point, it notably underestimates the degradation factor compared to the other models. However, it maintains a strict exponential trajectory throughout the entire domain. This robustness is a direct result of the composite kernel architecture; the large value of the Matérn length-scale forces the model to rely on the Dot-Product kernel, ensuring that the Arrhenius law is preserved even in extrapolation.

The practical consequence of these differences is validated in the time-domain simulation shown in Figure 20. This plot presents the capacity fade for the specific test condition of 45°C and 50% SoC.

Figure 20 – Capacity fade simulation and error metrics for the specific condition of 45°C and 50% SoC.

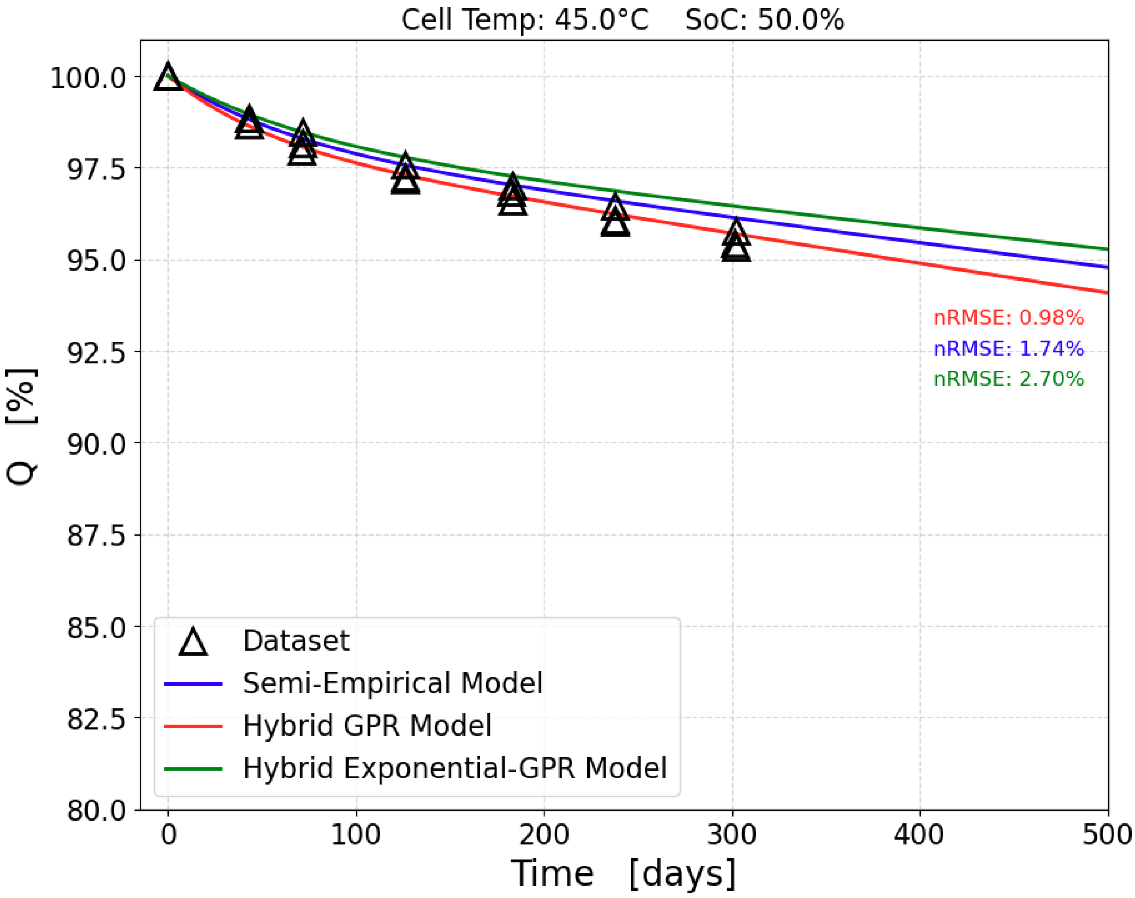

Source: Elaborated by the author.

The behavior of the capacity curves directly mirrors the magnitude of the degradation factors observed in Figure 19. The Hybrid GPR, which estimated the highest $f_{d,\mathrm{cal}}$ value at 45°C, predicts the steepest capacity decline. Since this prediction passes directly through the validation data points (triangles), it yields the lowest local error (nRMSE = 0.98%).

The Semi-Empirical Model follows with a moderate degradation rate and a slightly higher error (nRMSE = 1.74%). Finally, the Hybrid Exponential-GPR, which underestimated the degradation factor at this specific coordinate, predicts a slower aging trajectory, resulting in the highest local error (nRMSE = 2.70%).

To evaluate the robustness of the models away from the calibration baseline, the analysis is extended to a different operating point: a fixed SoC of 65%. Figure 21 presents the degradation factor behavior across the temperature domain for this condition.

Figure 21 – Comparison of the predicted degradation factor $f_{d,\mathrm{cal}}$ as a function of Temperature at an off-baseline condition ($SoC = 65\%$).

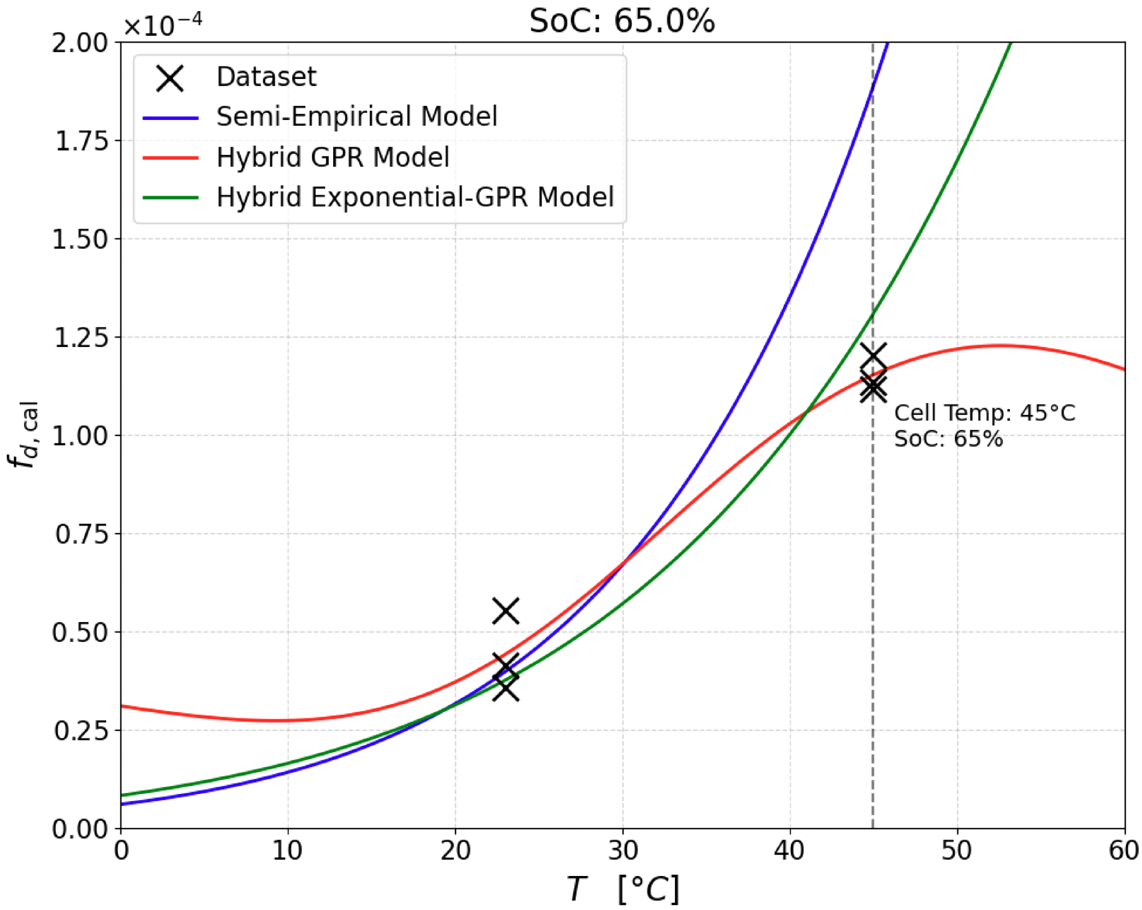

Source: Elaborated by the author.

A critical divergence is observed in the Semi-Empirical Model. Unlike the previous case (SoC=50%) where it aligned well with the data, here it significantly overestimates the degradation rate, particularly at higher temperatures. This error exposes a fundamental limitation of the traditional semi-empirical framework: the assumption that stress factors are uncorrelated and their effects are strictly multiplicative ($S_T(T) \cdot S_{SoC}(SoC)$). Because the thermal stress function S_T was calibrated at the reference SoC of 50%, the model implicitly assumes that the thermal effect remains identical at 65% SoC. The deviation seen in Figure 21 suggests that these stressors are coupled; the pure thermal effect derived at one SoC level does not perfectly extrapolate to another, causing the prediction accuracy to deteriorate as the operating point shifts away from the calibration baseline.

In contrast, both hybrid models demonstrate superior adaptability. The Hybrid GPR once again captures the local nonlinearities with high precision, passing closest to the experimental validation points at 45°C. More importantly, the Hybrid Exponential-GPR exhibits a marked improvement over the Semi-Empirical baseline. By learning the surface across the joint input space $(1/T, SoC)$ rather than assuming fixed separability, it achieves a more accurate representation of the degradation magnitude while preserving the physically correct exponential shape.

The impact of these behaviors on the remaining capacity prediction is quantified in Figure 22.

Figure 22 – Capacity fade simulation for 45°C and 65% SoC.

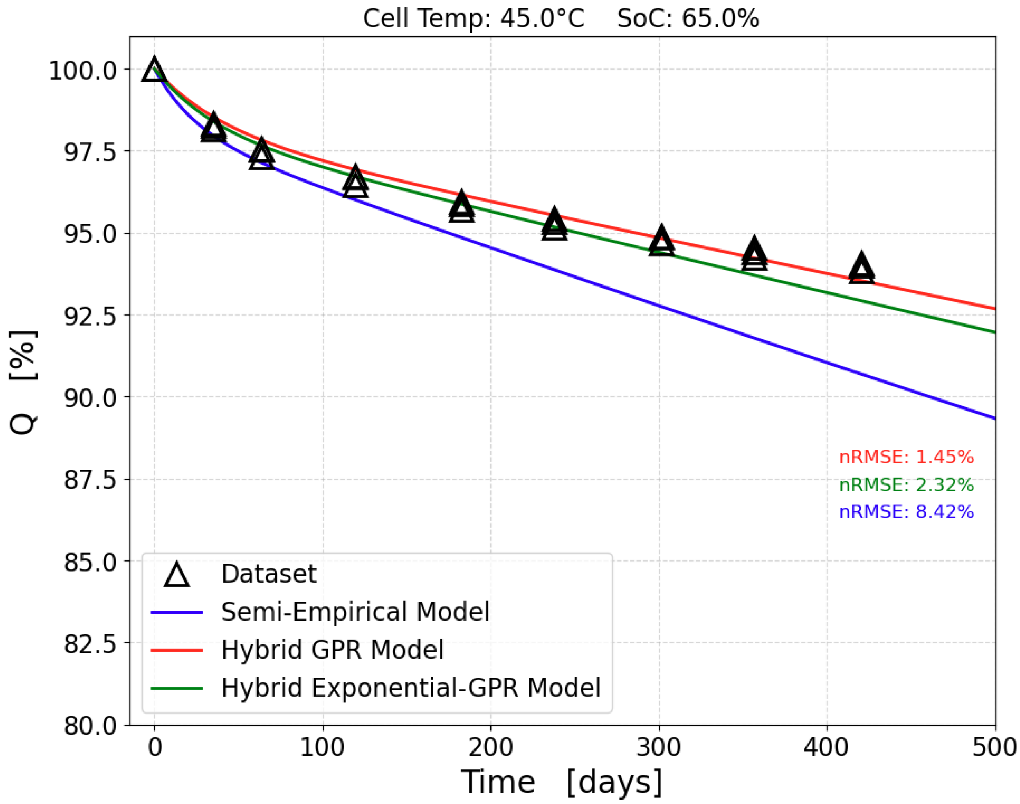

Source: Elaborated by the author.

The consequences of the Semi-Empirical Model's overestimation are evident in the steep capacity drop, resulting in a substantial prediction error (nRMSE = 8.42%). The Hybrid GPR maintains its dominance in local accuracy, yielding the lowest error (nRMSE = 1.45%). With an nRMSE of 2.32%, the Hybrid Exponential-GPR significantly outperforms the Semi-Empirical Model.

The qualitative assessment extends to the cycle aging domain. A crucial methodological distinction must be made regarding the comparison in this regime. As defined in Equation (3.7), the pure cycle degradation factor $f_{d,\text{cyc}}$ is obtained by subtracting the calendar aging contribution from the total observed degradation ($f_{d,\text{cyc}} = f^*_{d,\text{cyc}} - f_{d,\text{cal}} \cdot t_{\text{cyc}}$). Since each modeling framework predicts a slightly different value for $f_{d,\text{cal}}$, the experimental target values for cycle aging also differ slightly between models. Consequently, Figure 23 displays distinct datasets for each model (represented by blue, red, and green markers).

Figure 23 illustrates the dependency of the degradation factor on DoD. It is

Figure 23 – Predicted cycle degradation factor $f_{d,\text{cyc}}$ as a function of DoD.

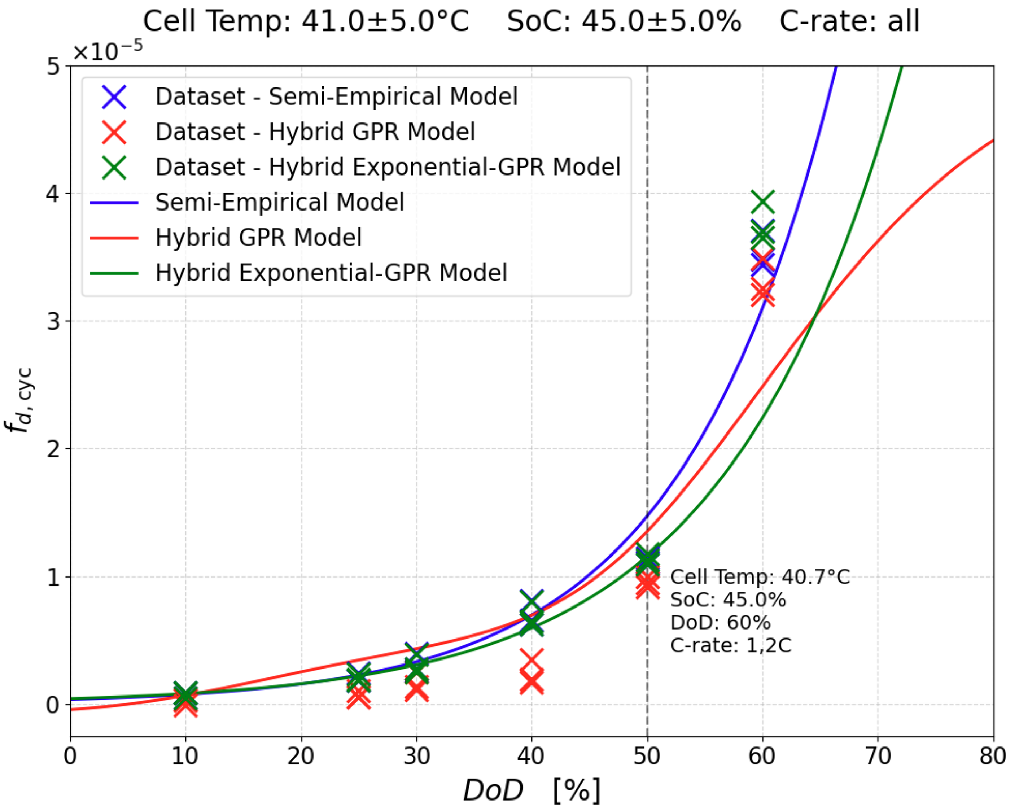

Source: Elaborated by the author.

important to note that, unlike the controlled calendar tests, these data points represent a sampling region within the multidimensional space rather than a single fixed condition. Small variations in temperature and SoC within the tolerance window contribute to the dispersion of the points, making a precise visual error assessment challenging.

The Semi-Empirical Model demonstrates a strong fit to its respective data points. This result is expected, as this specific region of the experimental space was utilized to calibrate the stress function S_{DoD} in the baseline methodology.

Surprisingly, the Hybrid GPR exhibits considerable deviation in this region. Beyond simply underestimating the degradation at higher DoDs, the model reveals a critical physical fragility: the prediction of negative degradation factors ($f_d < 0$) in low-stress regions. Since f_d represents cumulative damage, a negative value implies the physical impossibility of capacity recovery. This inconsistency arises from the unconstrained nature of the standard GP; when the estimated calendar aging component ($f_{d,\text{cal}}$) used in the subtraction equation marginally exceeds the total aggregated degradation due to statistical noise, the resulting pure cycle factor becomes negative—a flaw the model fails to suppress.

The Hybrid Exponential-GPR, however, effectively mitigates this issue. By enforcing a positive-definite exponential structure, it maintains a consistent, physically valid trajectory across the entire range ($f_d > 0$). While it shows some deviation at the 60% DoD cluster, its global stability is superior. The practical benefit of this approach becomes evident when evaluating the capacity fade for a specific validation point, where the exact values of all stressors are known.

Figure 24 presents the validation for a cell cycled at 40.7°C, 45% SoC, 50% DoD, and 1.20 C.

Figure 24 – Capacity fade simulation for a cycling condition (40.7°C, 45% SoC, 50% DoD, and 1.20 C).

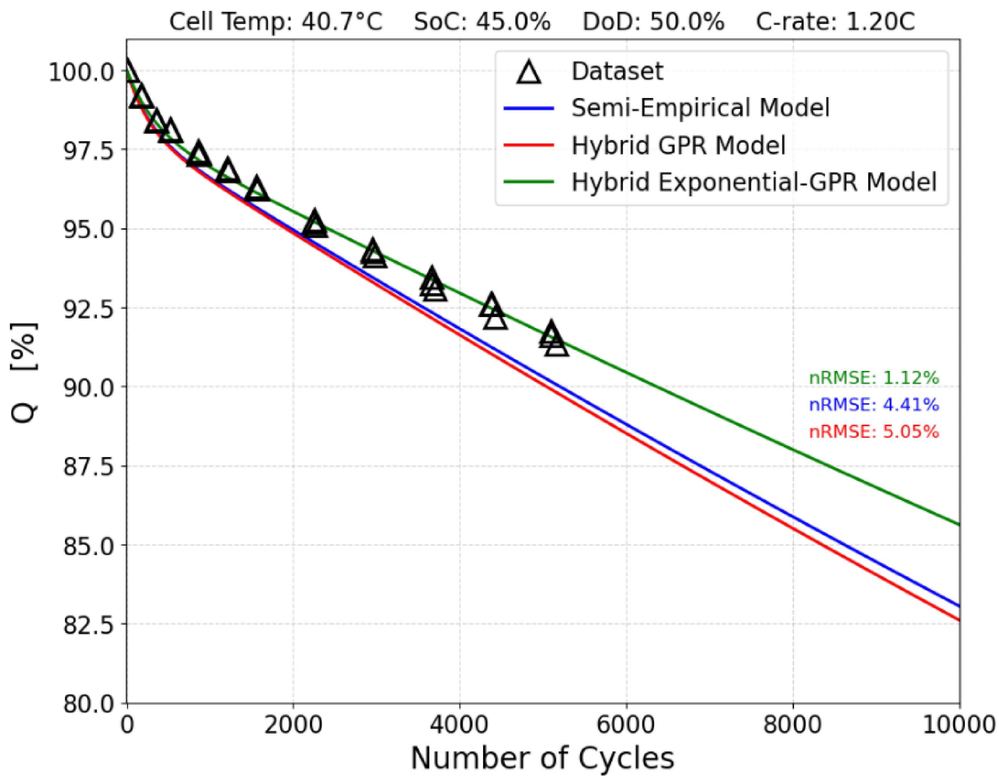

Source: Elaborated by the author.

In this precise comparison, the Hybrid Exponential-GPR demonstrates remarkable accuracy, achieving an nRMSE of just 1.12%. It follows the experimental decay almost perfectly, significantly outperforming the Semi-Empirical Model (nRMSE = 4.41%) and the standard Hybrid GPR (nRMSE = 5.05%). This result underscores the efficacy of the proposed architecture: by enforcing a global exponential structure via the Dot-Product kernel, the model effectively filters the noise inherent in the cycle extraction process and robustly interpolates across regions of data sparsity, resulting in a predictor that is both physically consistent and numerically superior.

4.6 ERROR ANALYSIS

Following the qualitative inspection of the degradation trends, a quantitative assessment was performed to measure the accuracy of each framework. As defined in the methodology, nRMSE was calculated for the capacity fade trajectory of each individual test point in the dataset.

The analysis begins with the calendar aging evaluation. Table 10 summarizes the global performance of the models, aggregating the errors across all 19 available calendar aging test conditions.

Table 10 – Global error metrics for the calendar aging dataset.

Model Architecture	**nRMSE**
Semi-Empirical Model	2.74%
Hybrid GPR Model	**1.20%**
Hybrid Exponential-GPR Model	1.54%

Source: Elaborated by the author.

The Semi-Empirical Model serves as the baseline, yielding a global nRMSE of 2.74%. While reasonably accurate, this error level reflects the limitations observed in the qualitative analysis, specifically the model's inability to account for the coupled effects of temperature and SoC outside the calibration reference point.

The Hybrid GPR Model achieves the highest accuracy, reducing the global error by more than half to 1.20%. This result highlights the power of the non-parametric approach in capturing the complex, non-monotonic electrochemical features.

The Hybrid Exponential-GPR Model delivers a performance comparable to the standard hybrid approach, with an nRMSE of 1.54%. Although slightly higher than the unconstrained GPR, this value represents a significant improvement over the semi-empirical baseline. The marginal increase in error relative to the standard GPR is a calculated trade-off: the model sacrifices a degree of local flexibility (by enforcing the Dot-Product kernel's exponential structure) to guarantee the physical consistency and extrapolation safety demonstrated in the previous section.

To understand how these global averages translate to specific test conditions, Figure 25 presents the frequency distribution of the nRMSE values calculated for each individual test point.

The histogram reveals a distinct skew in the performance of the Semi-Empirical Model (blue bars). While it performs adequately for conditions near the calibration point (low error bars), it exhibits a long tail of high-error outliers (nRMSE $>$ 4% and up to 8%). These outliers correspond to the operating points where the assumption of uncorrelated

Figure 25 – Histogram of nRMSE values for the 19 calendar aging test conditions.

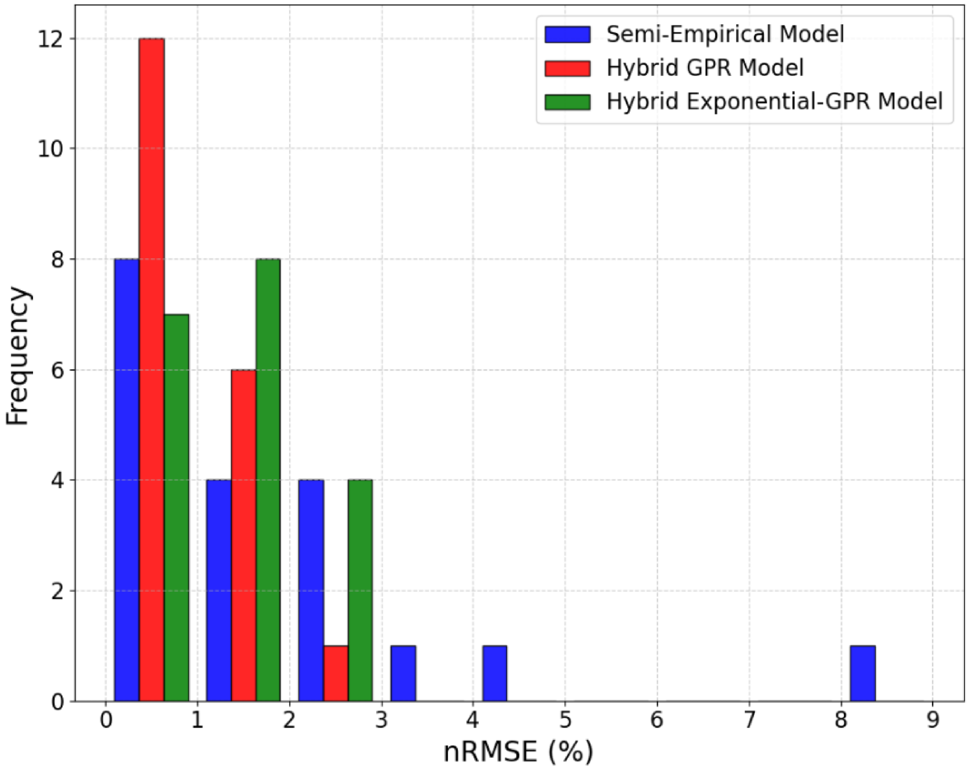

Source: Elaborated by the author.

stressors breaks down.

Conversely, the Hybrid GPR (red bars) is densely clustered in the lowest error bin ($0.5\% - 1.0\%$), confirming its superior capability across the entire experimental space. The Hybrid Exponential-GPR (green bars) follows a similar distribution. Ideally, it avoids the high-error outliers present in the semi-empirical results while maintaining a distribution shape similar to the standard GPR, confirming that the exponential architecture does not significantly compromise the model's ability to fit the experimental data.

The evaluation proceeds to the cycle aging dataset. As detailed in the methodology, this stage presents a higher degree of complexity due to the cLH sampling strategy, which distributes test points sparsely across the multi-dimensional stress space rather than in convenient factorial grids. Table 11 presents the aggregated error metrics for the cycle aging conditions.

A stark contrast in performance is observed compared to the calendar aging results. The Semi-Empirical Model exhibits a substantial global error of 16.80%. This performance degradation is intrinsic to the model's reliance on sequentially isolating stress factors (S_{DoD}, S_C). In a cLH design, variables are changed simultaneously, preventing the clean isolation of single-factor dependencies. Consequently, the rigid functional fits fail to capture the degradation surface accurately, leading to severe prediction errors in regions of the design

Table 11 – Global error metrics for the cycle aging dataset.

Model Architecture	**Global nRMSE**
Semi-Empirical Model	16.80%
Hybrid GPR Model	3.72%
Hybrid Exponential-GPR Model	**2.67%**

Source: Elaborated by the author.

space that deviate from the specific slices used for parameterization.

Conversely, the Hybrid Exponential-GPR Model emerges as the superior architecture, achieving the lowest nRMSE of 2.67%. This result suggests that the composite kernel structure is particularly advantageous in sparse, non-fatorial data regimes. By enforcing a global exponential trend via the Dot-Product component, the model effectively filters the noisy data, while the Matérn component handles the local nuances of the cLH samples without overfitting.

The standard Hybrid GPR follows with an nRMSE of 3.72%. While significantly better than the semi-empirical baseline, it falls short of the exponential variant, likely due to the issues identified in the qualitative analysis. The distribution of these errors is visualized in Figure 26.

Figure 26 – Histogram of nRMSE values for the cycle aging test conditions.

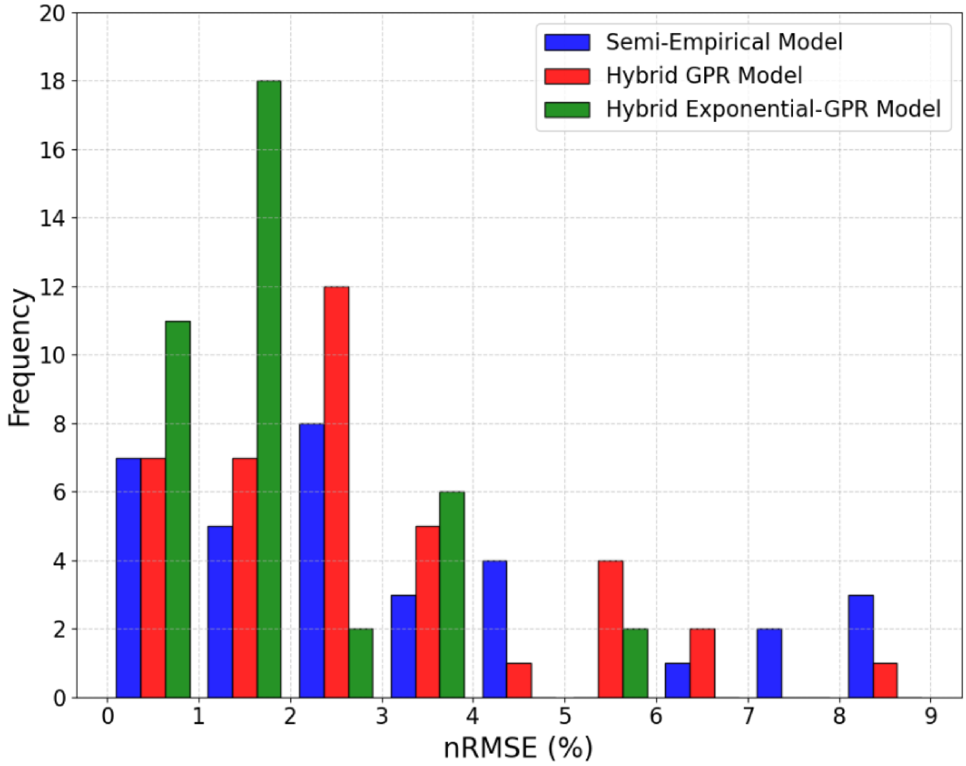

Source: Elaborated by the author.

The histogram corroborates the metric table. The Hybrid Exponential-GPR is tightly clustered on the left, indicating consistent reliability. The Semi-Empirical Model, however, shows a highly dispersed distribution. It is important to note that this histogram is truncated for clarity; the Semi-Empirical Model produced extreme outliers with nRMSE values significantly exceeding the displayed range. These outliers, which heavily penalize the global nRMSE metric, correspond to test conditions where the combined stress factors pushed the model far outside its calibrated linear validity. The complete table with the errors for every individual test point is provided in the Appendix B.

Finally, Table 12 consolidates the results from both calendar and cycle aging datasets to provide a holistic view of model performance.

Table 12 – Overall global performance (calendar and cycle datasets).

Model Architecture	**Global nRMSE**
Semi-Empirical Model	14.78%
Hybrid GPR Model	3.31%
Hybrid Exponential-GPR Model	**2.45%**

Source: Elaborated by the author.

Since the experimental campaign contains a larger number of cycle test conditions than calendar points, the global metric is heavily weighted by the cycling performance. Consequently, the Hybrid Exponential-GPR Model is identified as the most robust overall solution, with a global nRMSE of 2.45%.

While the standard Hybrid GPR proved slightly superior in the strictly controlled environment of calendar aging, the exponential variant demonstrates the best generalized performance. It successfully balances the data-driven flexibility required to correct nonlinear electrochemical behaviors (such as SoC) with the structural rigidity needed to ensure physical consistency and robustness in sparse, multi-dimensional cycling datasets.

4.7 SUMMARY

The empirical analyses conducted in this chapter confirm a clear trade-off between standard modeling techniques. The results demonstrated that while the traditional Semi-Empirical Model provides a stable and physically safe baseline, it lacks the flexibility to fully map the complex degradation profiles observed in the dataset. Conversely, the standard Hybrid GPR, despite showing excellent fitting metrics in training regions, failed to maintain consistency during extrapolation.

The performance metrics and extrapolation tests validate that the Hybrid Exponential-GPR successfully resolves this conflict. By mathematically constraining the data-driven learning process, it delivered the most robust performance. These quantitative findings confirm the viability of the proposed methodology and provide the necessary basis for the final overarching conclusions of this work, discussed in the next chapter.

5 FINAL CONSIDERATIONS

This dissertation presented a comprehensive modeling framework for the Samsung INR21700-50E lithium-ion battery, addressing the critical challenge of balancing predictive accuracy with physical consistency in aging estimation. By integrating a vast experimental dataset encompassing 250 years of accumulated aging time, this study systematically compared a traditional Semi-Empirical baseline against two novel data-driven architectures: a Hybrid GPR and a Hybrid Exponential-GPR model.

Reflecting upon the specific objectives established at the beginning of this work, all proposed goals were successfully achieved with a high degree of satisfaction. The baseline Semi-Empirical Model was effectively parameterized to map fundamental aging physics, which subsequently paved the way for the successful development of the standard Hybrid GPR and the Hybrid Exponential-GPR architectures. Through the utilization of the comprehensive aging dataset, it was possible to thoroughly evaluate and compare these frameworks, explicitly addressing their data fitting accuracies and physical consistencies.

The investigation yielded several key insights regarding both the degradation mechanisms of the cell and the mathematical limitations of existing modeling approaches:

1. **Verification of Non-Monotonic SoC Dependencies:** The study verified that calendar aging exhibits complex, nonlinear, and non-monotonic fluctuations with respect to SoC. Since this degradation profile is highly specific and can vary significantly between different battery models, traditional modeling becomes challenging. While the Semi-Empirical framework is limited by the strict requirement to define an appropriate functional form a priori—often forcing simplified approximations—the Hybrid approaches demonstrated the intrinsic ability to naturally adapt to these specific electrochemical irregularities without relying on pre-defined equations.

2. **Data-Driven Confirmation of C-rate Insensitivity:** Through the Automatic Relevance Determination inherent to the GPR kernels, the study provided rigorous statistical confirmation that the C-rate is a negligible independent stressor for this specific high-energy cell chemistry. This validates the physical hypothesis that current-induced degradation is primarily thermal-driven, allowing for model simplification without loss of fidelity.

3. **Limitations of Pure Data-Driven Approaches:** While the standard Hybrid GPR achieved the lowest error in the controlled calendar aging dataset (nRMSE = 1.20%), it exhibited critical physical inconsistencies during extrapolation. Specifically, it predicted thermodynamically impossible phenomena, such as negative degradation rates (capacity recovery), highlighting the risks of deploying unconstrained ML models in safety-critical BESS applications.

The most significant contribution of this work is the development and validation of the Hybrid Exponential-GPR framework. By incorporating a composite kernel architecture—combining a Dot-Product kernel to enforce global exponential trends with a Matérn kernel for local flexibility—this model effectively bridged the gap between physics-based and data-driven methods.

Quantitative validation demonstrated that the Hybrid Exponential-GPR provides the most robust generalization capability. It outperformed the Semi-Empirical baseline by a wide margin, reducing the global nRMSE from 14.78% to 2.45%. Crucially, it demonstrated superior performance in the sparse, multi-dimensional cLH cycle aging dataset, proving its ability to decouple complex stress interactions that the Semi-Empirical approach could not resolve.

In conclusion, the Hybrid Exponential-GPR Model offers a physics-guided solution while retaining the flexibility to learn complex electrochemical features from data. This makes it an ideal candidate for integration into real-time BESS controllers, enabling more reliable lifetime prediction, safer operation, and optimized economic dispatch strategies.

5.1 FUTURE WORK

Building upon the findings and the methodological framework developed in this study, several avenues for future research are proposed to further enhance battery degradation modeling and its practical applications:

- **C-rate and Temperature Gradient Correlation for Operational Planning:** This study demonstrated that battery degradation is fundamentally insensitive to the C-rate as an isolated stress factor; rather, its impact is physically manifested through the elevation of the cell temperature due to internal heat generation. In the context of aging-awareness, operators can design cycling profiles and control ambient temperatures; yet, accurately predicting the cell temperature during the planning stage is a challenge. Therefore, future work should focus on establishing a robust correlation between the planned operational C-rate and the expected temperature gradient (the difference between the cell and ambient temperatures). By developing a model that predicts the cell temperature elevation directly from the planned C-rate, it will be possible to accurately assess the thermal impact of different dynamic load profiles, thereby drastically improving the fidelity of degradation predictions during the operational planning phase.
- **Validation Across Diverse Chemistries and Formats:** To confirm the generalizability and robustness of the proposed Hybrid Exponential-GPR framework, subsequent studies should test the architecture using different lithium-ion battery chemistries (e.g., Lithium Iron Phosphate or various Nickel Manganese Cobalt blends)

and varying cell formats. Applying the model to diverse datasets will verify its inherent flexibility and help identify any necessary structural adaptations when the dominant physical degradation mechanisms differ from those of the cells analyzed in this research.

- **Integration into Aging-Aware Optimization Frameworks:** A highly promising practical application of this research is the implementation of the developed model within an optimization framework for aging-aware operation. Given its consistent reliability and capability to capture complex nonlinear stress interactions, the Hybrid Exponential-GPR model can be embedded into a BMS. By utilizing the model's capacity fade predictions in the objective function, optimization algorithms could dynamically schedule loads, adjust charging protocols, or manage grid dispatch strategies to minimize degradation and extend the battery lifespan without compromising performance demands. Ultimately, this ensures that large-scale BESS can be operated reliably and economically, linking physical battery limits with real-time operational management.

Bibliography

[1] COLLATH, N., TEPE, B., ENGLBERGER, S., JOSSEN, A., HESSE, H., "Aging aware operation of lithium-ion battery energy storage systems: A review", *Journal of Energy Storage*, v. 55, 2022.

[2] HU, X., FENG, F., LIU, K., ZHANG, L., XIE, J., LIU, B., "State estimation for advanced battery management: Key challenges and future trends", *Renewable and Sustainable Energy Reviews*, v. 114, 2019.

[3] LIU, K., WANG, Y., LAI, X., *Data Science-Based Full-Lifespan Management of Lithium-Ion Battery. Green Energy and Technology*, Springer Cham, 2022.

[4] BARRÉ, A., DEGUILHEM, B., GROLLEAU, S., GÉRARD, M., SUARD, F., RIU, D., "A review on lithium-ion battery ageing mechanisms and estimations for automotive applications", *Journal of Power Sources*, v. 241, pp. 680–689, 2013.

[5] RENIERS, J. M., MULDER, G., HOWEY, D. A., "Review and performance comparison of mechanical-chemical degradation models for lithium-ion batteries", *Journal of The Electrochemical Society*, v. 166, n. 14, pp. A3189–A3200, 2019.

[6] XU, B., OUDALOV, A., ULBIG, A., ANDERSSON, G., KIRSCHEN, D. S., "Modeling of Lithium-Ion Battery Degradation for Cell Life Assessment", *IEEE Transactions on Smart Grid*, v. 9, n. 2, pp. 1131–1140, 2018.

[7] KEIL, P., SCHUSTER, S. F., WILHELM, J., TRAVI, J., HAUSER, A., KARL, R. C., JOSSEN, A., "Calendar aging of lithium-ion batteries: I. Impact of the graphite anode on capacity fade", *Journal of The Electrochemical Society*, v. 163, n. 9, pp. A1872–A1880, 2016.

[8] SARASKETA-ZABALA, E., GANDIAGA, I., RODRIGUEZ-MARTINEZ, L. M., VILLARREAL, I., "Calendar ageing analysis of a LiFePO4/graphite cell with dynamic model validations: Towards realistic lifetime predictions", *Journal of Power Sources*, v. 272, pp. 45–57, 2014.

[9] CHEN, Y., HE, Y., LI, Z., CHEN, L., "A Combined Multiple Factor Degradation Model and Online Verification for Electric Vehicle Batteries", *Energies*, v. 12, 2019.

[10] CHEN, Z., LI, Z., CHEN, G., "Optimal configuration and operation for user-side energy storage considering lithium-ion battery degradation", *International Journal of Electrical Power & Energy Systems*, v. 145, 2023.

[11] SARASKETA-ZABALA, E., GANDIAGA, I., MARTINEZ-LASERNA, E., RODRIGUEZ-MARTINEZ, L. M., VILLARREAL, I., "Cycle ageing analysis of a LiFePO4/graphite cell with dynamic model validations: Towards realistic lifetime predictions", *Journal of Power Sources*, v. 275, pp. 573–587, 2015.

[12] NAUMANN, M., SCHIMPE, M., KEIL, P., HESSE, H. C., JOSSEN, A., "Analysis and modeling of calendar aging of a commercial LiFePO4/graphite cell", *Journal of Energy Storage*, v. 17, pp. 153–169, 2018.

[13] VETTER, J., NOVÁK, P., WAGNER, M. R., VEIT, C., MÖLLER, K.-C., BESENHARD, J. O., WINTER, M., WOHLFAHRT-MEHRENS, M., VOGLER, C., HAMMOUCHE, A., "Ageing mechanisms in lithium-ion batteries", *Journal of Power Sources*, v. 147, pp. 269–281, 2005.

[14] WALDMANN, T., WILKA, M., KASPER, M., FLEISCHHAMMER, M., WOHLFAHRT-MEHRENS, M., "Temperature dependent ageing mechanisms in Lithium-ion batteries–A Post-Mortem study", *Journal of Power Sources*, v. 262, pp. 129–135, 2014.

[15] ZHANG, J., LEE, J., "A review on prognostics and health monitoring of Li-ion battery", *Journal of Power Sources*, v. 196, n. 15, pp. 6007–6014, 2011.

[16] EDGE, J. S., O'KANE, S., PROSSER, R., KIRKALDY, N. D., PATEL, A. N., HALES, A., GHOSH, A., AI, W., CHEN, J., YANG, J., LI, S., PANG, M. C., DIAZ, L. B., TOMASZEWSKA, A., MARZOOK, M. W., RADHAKRISHNAN, K. N., WANG, H., PATEL, Y., WU, B., OFFER, G. J., "Lithium-ion battery degradation: what you need to know", *Physical Chemistry Chemical Physics*, v. 23, pp. 8200–8221, 2021.

[17] LIU, K., LI, K., PENG, Q., ZHANG, C., "A brief review on key technologies in the battery management system of electric vehicles", *Frontiers of Mechanical Engineering*, v. 14, n. 1, pp. 47–64, 2018.

[18] HU, X., FENG, F., LIU, K., ZHANG, L., XIE, J., LIU, B., "State estimation for advanced battery management: Key challenges and future trends", *Renewable and Sustainable Energy Reviews*, v. 114, pp. 109334, 2019.

[19] XIONG, R., LI, L., TIAN, J., "Towards a smarter battery management system: A critical review on battery state of health monitoring methods", *Journal of Power Sources*, v. 405, pp. 18–29, 2018.

[20] LI, Y., LIU, K., FOLEY, A. M., ZÜLKE, A., BERECIBAR, M., NANINI-MAURY, E., VAN MIERLO, J., HOSTER, H. E., "Data-driven health estimation and lifetime prediction of lithium-ion batteries: A review", *Renewable and Sustainable Energy Reviews*, v. 113, pp. 109254, 2019.

[21] SCHMALSTIEG, J., KÄBITZ, S., ECKER, M., SAUER, D. U., "A holistic aging model for Li(NiMnCo)O2 based 18650 lithium-ion batteries", *Journal of Power Sources*, v. 257, pp. 325–334, 2014.

[22] STROEBL, F., PETERSOHN, R., SCHRICKER, B., SCHAEUFL, F., BOHLEN, O., PALM, H., "A multi-stage lithium-ion battery aging dataset using various experimental design methodologies", *Sci Data*, v. 11, n. 1020, 2024.

[23] HANNAN, M., LIPU, M., HUSSAIN, A., MOHAMED, A., "A review of lithium-ion battery state of charge estimation and management system in electric vehicle applications: Challenges and recommendations", *Renewable and Sustainable Energy Reviews*, v. 78, pp. 834–854, 2017.

[24] BERECIBAR, M., GANDIAGA, I., VILLARREAL, I., OMAR, N., VAN MIERLO, J., VAN DEN BOSSCHE, P., "Critical review of state of health estimation methods

of Li-ion batteries for real applications", *Renewable and Sustainable Energy Reviews*, v. 56, pp. 572–587, 2016.

[25] WAAG, W., FLEISCHER, C., SAUER, D. U., "Critical review of the methods for monitoring of lithium-ion batteries in electric and hybrid vehicles", *Journal of Power Sources*, v. 258, pp. 321–339, 2014.

[26] RICHARDSON, R. R., OSBORNE, M. A., HOWEY, D. A., "Gaussian process regression for forecasting battery state of health", *Journal of Power Sources*, v. 357, pp. 209–219, 2017.

[27] SEVERSON, K. A., ATTIA, P. M., JIN, N., PERKINS, N., JIANG, B., YANG, Z., CHEN, M. H., AYKOL, M., HERRING, P. K., FRAGGEDAKIS, D., BAZANT, M. Z., HARRIS, S. J., CHUEH, W. C., BRAATZ, R. D., "Data-driven prediction of battery cycle life before capacity degradation", *Nature Energy*, v. 4, n. 5, pp. 383–391, 2019.

[28] HESSE, H. C., SCHIMPE, M., KUCEVIC, D., JOSSEN, A., "Lithium-ion battery storage for the grid—A review of stationary battery storage system design tailored for applications in modern power grids", *Energies*, v. 10, n. 12, pp. 2107, 2017.

[29] YANG, Y., BREMNER, S., MENICTAS, C., KAY, M., "Battery energy storage system size determination in renewable energy systems: A review", *Renewable and Sustainable Energy Reviews*, v. 91, pp. 109–125, 2018.

[30] APRIBOWO, C. H. B., SARJIYA, S., HADI, S. P., WIJAYA, F. D., "Optimal Planning of Battery Energy Storage Systems by Considering Battery Degradation due to Ambient Temperature: A Review, Challenges, and New Perspective", *Batteries*, v. 8, n. 12, pp. 290, 2022.

[31] WU, Y., XU, T., MENG, H., WEI, W., CAI, S., GUO, L., "Energy storage capacity allocation for distribution grid applications considering the influence of ambient temperature", *IET Energy Systems Integration*, v. 4, n. 1, pp. 143–156, 2022.

[32] RASMUSSEN, C. E., WILLIAMS, C. K. I., *Gaussian Processes for Machine Learning*. The MIT Press, 2006.

APPENDIX A – DATASET MODIFICATIONS AND EXCLUSIONS

This appendix provides a comprehensive record of the specific modifications and exclusions applied to the raw battery aging dataset prior to the modeling phase. As outlined in Chapter 3, these interventions were necessary to address localized inconsistencies, such as logging errors, equipment malfunctions, or procedural deviations documented during the original experimental campaign. Table 13 catalogs each identified issue along with the corresponding corrective action taken to ensure the integrity and robustness of the training data.

Table 13 – Summary of specific modifications and exclusions applied to the raw dataset.

Stage	TP/Serial	Identified Inconsistency	Action Taken
1	TP_z01_01	TP_z01_01_02_ZYK_meta has an incorrect date.	Date replaced with a more compatible date: From 21/09/2021 to 30/09/2021 - The date 21/09/2021 was incorrect since the ET ended on 30/09/2021.
1	TP_z01_01	TP_z01_01_22_ZYK_meta has an incorrect date.	Date replaced with a more compatible date: From 06/03/2022 to 06/04/2022 - The date 06/03/2021 was incorrect as the month does not make sense. The previous CU ended on 05/04/2022.
1	TP_z01_01	TP_z01_01_24_ZYK_meta has an incorrect date.	Date replaced with a more compatible date: From 24/05/2022 to 04/05/2022 - The date 24/05/2022 was incorrect since the previous CU ends on 03/05/2022, the subsequent CU begins on 31/05/2022, and the ZYK in question lasted 26 days.

Continued on next page

Table 13 – continued from previous page

Stage	TP/Serial	Identified Inconsistency	Action Taken
1	TP_z01_02	Duplicate and incompatible meta files: TP_z01_02_15_CU_meta and TP_z01_02_15_exCU_meta	Deleted file TP_z01_02_15_exCU_meta, as the test CSV was TP_z01_02_15_CU
1	TP_z02_02	TP_z02_02_16_ZYK wrong date (wrong year)	Corrected the date from 19/01/2021 to 19/01/2022 This date was based on the dates for TP_z02_01 and TP_z02_03, which have the same dates.
1	TP_z04_01	Data with large deviation when compared to z04_02 and z04_03	Data from test TP_z04_01 were not considered for training the model.
1	TP_z04_02	TP_z04_02 has two repeated CUs - TP_z04_02_11_CU and TP_z04_02_12_CU	Data used up to TP_z04_02_11_CU
1	TP_z04_03	TP_z04_03 has two repeated CUs - TP_z04_03_11_CU and TP_z04_03_12_CU	Data used up to TP_z04_03_11_CU
1	TP_z04_03	TP_z04_03_11_CU with highly discrepant capacity value.	Data used only up to 09_CU.
1	TP_z06_01	Incompatible dates: TP_z06_01_16_ZYK, TP_z06_01_17_CU, TP_z06_01_18_ZYK	Adjusted dates to correct the order and align with previous and subsequent tests.
1	TP_z06_02	Incompatible dates: TP_z06_02_16_ZYK, TP_z06_02_17_CU, TP_z06_02_18_ZYK	Adjusted dates to correct the order and align with previous and subsequent tests.

Continued on next page

Table 13 – continued from previous page

Stage	TP/Serial	Identified Inconsistency	Action Taken
1	TP_z06_03	Incompatible dates: TP_z06_03_16_ZYK, TP_z06_03_17_CU, TP_z06_03_18_ZYK	Adjusted dates to correct the order and align with previous and subsequent tests.
1	TP_z09_02	TP_z09_02_21_CU with incompatible date	Changed date from 02/05/2022 to 18/07/2022 This date was based on the dates of TP_09_01 and TP_z09_03, which have the same dates.
1	TP_z12_03	TP_z12_03_07_exCU with wrong date: xx/12/2021	Date replaced with the correct date: 05/12/2021 This date was based on the dates of TP_z12_01 and TP_z12_02, which have the same dates.
1	TP_z13_01	Data with large deviation when compared to z13_02 and z13_03	Data from test TP_z13_01 were not considered for training the model.
1	TP_z13_02	TP_z13_02_25_AT_T10, TP_z13_02_25_AT_T23 and TP_z13_02_25_AT_T45 with incorrect dates.	Date replaced with a more compatible date: TP_z13_02_25_AT_T10 -> From 06/09/2022 to 06/10/2022 TP_z13_02_25_AT_T45 -> From 09/09/2022 to 06/10/2022 TP_z13_02_25_AT_T23 -> From 12/09/2022 to 06/10/2022 These new dates were based on TP_z13_01, which has identical dates but has the correct AT test dates.

Continued on next page

Table 13 – continued from previous page

Stage	TP/Serial	Identified Inconsistency	Action Taken
1	TP_z13_03	TP_z13_03_25_AT_T10, TP_z13_03_25_AT_T23 and TP_z13_03_25_AT_T45 with incorrect dates.	Date replaced with a more compatible date: TP_z13_03_25_AT_T10 -> From 06/09/2022 to 06/10/2022 TP_z13_03_25_AT_T45 -> From 09/09/2022 to 06/10/2022 TP_z13_03_25_AT_T23 -> From 12/09/2022 to 06/10/2022 These new dates were based on TP_z13_01, which has identical dates but has the correct AT test dates.
1	TP_z14_01	TP_z14_01_25_AT_T10, TP_z14_01_25_AT_T23 and TP_z14_01_25_AT_T45 with incorrect dates.	Date replaced with a more compatible date: TP_z14_01_25_AT_T10 -> From 06/09/2022 to 06/10/2022 TP_z14_01_25_AT_T45 -> From 09/09/2022 to 06/10/2022 TP_z14_01_25_AT_T23 -> From 12/09/2022 to 06/10/2022 These new dates were based on TP_z13_01, which has identical dates but has the correct AT test dates.

Continued on next page

Table 13 – continued from previous page

Stage	TP/Serial	Identified Inconsistency	Action Taken
1	TP_z14_02	TP_z14_02_25_AT_T10, TP_z14_02_25_AT_T23 and TP_z14_02_25_AT_T45 with incorrect dates.	Date replaced with a more compatible date: TP_z14_02_25_AT_T10 -> From 06/09/2022 to 06/10/2022 TP_z14_02_25_AT_T45 -> From 09/09/2022 to 06/10/2022 TP_z14_02_25_AT_T23 -> From 12/09/2022 to 06/10/2022 These new dates were based on TP_z13_01, which has identical dates but has the correct AT test dates.
1	TP_z14_03	TP_z14_03_25_AT_T10, TP_z14_03_25_AT_T23 and TP_z14_03_25_AT_T45 with incorrect dates.	Date replaced with a more compatible date: TP_z14_03_25_AT_T10 -> From 06/09/2022 to 06/10/2022 TP_z14_03_25_AT_T45 -> From 09/09/2022 to 06/10/2022 TP_z14_03_25_AT_T23 -> From 12/09/2022 to 06/10/2022 These new dates were based on TP_z13_01, which has identical dates but has the correct AT test dates.

Continued on next page

Table 13 – continued from previous page

Stage	**TP/Serial**	**Identified Inconsistency**	**Action Taken**
1	TP_z15_01	TP_z15_01_25_AT_T10, TP_z15_01_25_AT_T23 and TP_z15_01_25_AT_T45 with incorrect dates.	Date replaced with a more compatible date: TP_z15_01_25_AT_T10 -> From 06/09/2022 to 06/10/2022 TP_z15_01_25_AT_T45 -> From 09/09/2022 to 06/10/2022 TP_z15_01_25_AT_T23 -> From 12/09/2022 to 06/10/2022 These new dates were based on TP_z13_01, which has identical dates but has the correct AT test dates.
1	TP_z15_02	TP_z15_02_25_AT_T10, TP_z15_02_25_AT_T23 and TP_z15_02_25_AT_T45 with incorrect dates.	Date replaced with a more compatible date: TP_z15_02_25_AT_T10 -> From 06/09/2022 to 06/10/2022 TP_z15_02_25_AT_T45 -> From 09/09/2022 to 06/10/2022 TP_z15_02_25_AT_T23 -> From 12/09/2022 to 06/10/2022 These new dates were based on TP_z13_01, which has identical dates but has the correct AT test dates.

Continued on next page

Table 13 – continued from previous page

Stage	TP/Serial	Identified Inconsistency	Action Taken
1	TP_z15_03	TP_z15_03_25_AT_T10, TP_z15_03_25_AT_T23 and TP_z15_03_25_AT_T45 with incorrect dates.	Date replaced with a more compatible date: TP_z15_03_25_AT_T10 -> From 06/09/2022 to 06/10/2022 TP_z15_03_25_AT_T45 -> From 09/09/2022 to 06/10/2022 TP_z15_03_25_AT_T23 -> From 12/09/2022 to 06/10/2022 These new dates were based on TP_z13_01, which has identical dates but has the correct AT test dates.
1	TP_z17_03	From TP_z17_03_17_CU onwards, the capacity value is highly discrepant.	Data used only up to 15_CU.
1	TP_z18_01	From TP_z18_01_17_CU onwards, the capacity value is highly discrepant.	Data used only up to 15_CU.
1	TP_z20_03	From TP_z20_03_17_CU onwards, the capacity value is highly discrepant.	Data used only up to 15_CU.
1	TP_z25_01	Data with large deviation when compared to z25_02 and z25_03	Data from test TP_z25_01 were not considered for training the model.
1	TP_z25_02	TP_z25_02_03_CU with incompatible date	Changed date from 12/10/2021 to 19/10/2021 to align with 02_ZYK and 04_ZYK.
1	TP_z25_03	TP_z25_03_03_CU with incompatible date	Changed date from 12/10/2021 to 19/10/2021 to align with 02_ZYK and 04_ZYK.
2	TP_z01_01	Missing file TP_z01_01_24_ZYK.	Data were considered only up to 23_CU.

Continued on next page

Table 13 – continued from previous page

Stage	TP/Serial	Identified Inconsistency	Action Taken
2	TP_z01_01	Incorrect date for 06_ZYK: 29/02/2023 (the year 2023 is not a leap year)	Corrected date to 01/03/2023.
2	TP_z01_02	Missing file TP_z01_02_24_ZYK.	Data were considered only up to 23_CU.
2	TP_z01_02	Incorrect date for 06_ZYK: 29/02/2023 (the year 2023 is not a leap year)	Corrected date to 01/03/2023.
2	TP_z01_02	Incorrect date for 20_ZYK: 13/17/2023	Corrected date to 13/07/2023.
2	TP_z01_03	Missing file TP_z01_03_24_ZYK.	Data were considered only up to 23_CU.
2	TP_z01_03	Incorrect date for 06_ZYK: 29/02/2023 (the year 2023 is not a leap year)	Corrected date to 01/03/2023.
2	TP_z01_03	Incorrect date for 20_ZYK: 13/17/2023	Corrected date to 13/07/2023.
2	TP_z02_01	Incorrect date for 06_ZYK: 29/02/2023 (the year 2023 is not a leap year)	Corrected date to 01/03/2023.
2	TP_z02_01	From 15_CU onwards, the capacity value is highly discrepant.	Data used only up to 13_exCU.
2	TP_z02_02	Incorrect date for 06_ZYK: 29/02/2023 (the year 2023 is not a leap year)	Corrected date to 01/03/2023.
2	TP_z02_02	From 15_CU onwards, the capacity value is highly discrepant.	Data used only up to 13_exCU.
2	TP_z02_03	Incorrect date for 06_ZYK: 29/02/2023 (the year 2023 is not a leap year)	Corrected date to 01/03/2023.

Continued on next page

Table 13 – continued from previous page

Stage	TP/Serial	Identified Inconsistency	Action Taken
2	TP_z02_03	Incompatible date for 11_CU: 12/04/2024	Corrected date to 04/04/2023. This date was based on the dates of TP_z02_01 and TP_z02_02, which have the same dates.
2	TP_z02_03	Data with large deviation when compared to z02_02 and z02_01	Data from test TP_z02_03 were not considered for training the model.
2	TP_z03_01	Missing file TP_z03_01_24_ZYK.	Data were considered only up to 23_CU.
2	TP_z03_01	Incorrect date for 06_ZYK: 29/02/2023 (the year 2023 is not a leap year)	Corrected date to 01/03/2023.
2	TP_z03_02	Missing file TP_z03_02_24_ZYK.	Data were considered only up to 23_CU.
2	TP_z03_02	Incorrect date for 06_ZYK: 29/02/2023 (the year 2023 is not a leap year)	Corrected date to 01/03/2023.
2	TP_z03_03	Missing file TP_z03_03_24_ZYK.	Data were considered only up to 23_CU.
2	TP_z03_03	Incorrect date for 06_ZYK: 29/02/2023 (the year 2023 is not a leap year)	Corrected date to 01/03/2023.
2	TP_z07_03	The capacity value of 15_CU is highly discrepant.	15_CU excluded from the analysis.
2	TP_z10_01	Data only goes up to 12_ZYK	Data used up to 11_CU
2	TP_z10_02	Data only goes up to 16_ZYK	Data used up to 15_CU
2	TP_z10_03	From 17_CU onwards, the capacity value is highly discrepant.	Data used only up to 15_CU.

Continued on next page

Table 13 – continued from previous page

Stage	TP/Serial	Identified Inconsistency	Action Taken
2	TP_z12_01	Initial date of 09_CU incompatible with end date of 08_ZYK	Changed the date of 09_CU from 22/03/2023 to 23/02/2023
2	TP_z12_01	From 21_CU onwards, the capacity value is incorrect.	Data used only up to 19_exCU.
2	TP_z12_02	Initial date of 09_CU incompatible with end date of 08_ZYK	Changed the date of 09_CU from 22/03/2023 to 23/02/2023
2	TP_z12_02	From 21_CU onwards, the capacity value is incorrect.	Data used only up to 19_exCU.
2	TP_z12_03	Initial date of 09_CU incompatible with end date of 08_ZYK	Changed the date of 09_CU from 22/03/2023 to 23/02/2023
2	TP_z12_03	From 21_CU onwards, the capacity value is incorrect.	Data used only up to 19_exCU.
2	TP_z13_01	Incompatible dates: TP_z13_01_33_AT_T10, TP_z13_01_33_AT_T23, TP_z13_01_33_AT_T45	Changed the dates from 13/02/2024 to 17/02/2024 to align with the other tests.
2	TP_z13_01	Initial date of 09_CU incompatible with end date of 08_ZYK	Changed the date of 09_CU from 22/03/2023 to 23/02/2023
2	TP_z13_01	Missing file TP_z13_01_14_ZYK.	Data were considered only up to 13_exCU.
2	TP_z13_02	Incompatible dates: TP_z13_02_33_AT_T10, TP_z13_02_33_AT_T23, TP_z13_02_33_AT_T45	Changed the dates from 13/02/2024 to 17/02/2024 to align with the other tests.
2	TP_z13_02	Initial date of 09_CU incompatible with end date of 08_ZYK	Changed the date of 09_CU from 22/03/2023 to 23/02/2023
2	TP_z13_02	Missing file TP_z13_02_14_ZYK.	Data were considered only up to 13_exCU.

Continued on next page

Table 13 – continued from previous page

Stage	TP/Serial	Identified Inconsistency	Action Taken
2	TP_z13_03	Incompatible dates: TP_z13_03_33_AT_T10, TP_z13_03_33_AT_T23, TP_z13_03_33_AT_T45	Changed the dates from 13/02/2024 to 17/02/2024 to align with the other tests.
2	TP_z13_03	Initial date of 09_CU incompatible with end date of 08_ZYK	Changed the date of 09_CU from 22/03/2023 to 23/02/2023
2	TP_z13_03	Missing file TP_z13_03_14_ZYK.	Data were considered only up to 13_exCU.
2	TP_z14_01	Incompatible dates: TP_z14_01_33_AT_T10, TP_z14_01_33_AT_T23, TP_z14_01_33_AT_T45	Changed the dates from 13/02/2024 to 17/02/2024 to align with the other tests.
2	TP_z14_01	Initial date of 09_CU incompatible with end date of 08_ZYK	Changed the date of 09_CU from 22/03/2023 to 23/02/2023
2	TP_z14_01	Missing file TP_z14_01_14_ZYK.	Data were considered only up to 13_exCU.
2	TP_z14_02	Incompatible dates: TP_z14_02_33_AT_T10, TP_z14_02_33_AT_T23, TP_z14_02_33_AT_T45	Changed the dates from 13/02/2024 to 17/02/2024 to align with the other tests.
2	TP_z14_02	Initial date of 09_CU incompatible with end date of 08_ZYK	Changed the date of 09_CU from 22/03/2023 to 23/02/2023
2	TP_z14_02	Missing file TP_z14_02_14_ZYK.	Data were considered only up to 13_exCU.
2	TP_z14_03	Incompatible dates: TP_z14_03_33_AT_T10, TP_z14_03_33_AT_T23, TP_z14_03_33_AT_T45	Changed the dates from 13/02/2024 to 17/02/2024 to align with the other tests.
2	TP_z14_03	Initial date of 09_CU incompatible with end date of 08_ZYK	Changed the date of 09_CU from 22/03/2023 to 23/02/2023

Continued on next page

Table 13 – continued from previous page

Stage	TP/Serial	Identified Inconsistency	Action Taken
2	TP_z14_03	Missing file TP_z14_03_14_ZYK.	Data were considered only up to 13_exCU.
2	TP_z15_01	Initial date of 09_CU incompatible with end date of 08_ZYK	Changed the date of 09_CU from 22/03/2023 to 23/02/2023
2	TP_z15_01	Missing file TP_z15_01_14_ZYK.	Data were considered only up to 13_exCU.
2	TP_z15_02	Initial date of 09_CU incompatible with end date of 08_ZYK	Changed the date of 09_CU from 22/03/2023 to 23/02/2023
2	TP_z15_02	Missing file TP_z15_02_14_ZYK.	Data were considered only up to 13_exCU.
2	TP_z15_03	Initial date of 09_CU incompatible with end date of 08_ZYK	Changed the date of 09_CU from 22/03/2023 to 23/02/2023
2	TP_z15_03	Missing file TP_z15_03_14_ZYK.	Data were considered only up to 13_exCU.
2	TP_z16_01	Incompatible dates: TP_z16_01_33_AT_T10, TP_z16_01_33_AT_T23, TP_z16_01_33_AT_T45	Changed the dates from 13/02/2024 to 17/02/2024 to align with the other tests.
2	TP_z16_01	Initial date of 09_CU incompatible with end date of 08_ZYK	Changed the date of 09_CU from 22/03/2023 to 23/02/2023
2	TP_z16_01	Missing file TP_z16_01_14_ZYK.	Data were considered only up to 13_exCU.
2	TP_z16_02	Incompatible dates: TP_z16_02_33_AT_T10, TP_z16_02_33_AT_T23, TP_z16_02_33_AT_T45	Changed the dates from 13/02/2024 to 17/02/2024 to align with the other tests.
2	TP_z16_02	Initial date of 09_CU incompatible with end date of 08_ZYK	Changed the date of 09_CU from 22/03/2023 to 23/02/2023

Continued on next page

Table 13 – continued from previous page

Stage	TP/Serial	Identified Inconsistency	Action Taken
2	TP_z16_02	Missing file TP_z16_02_14_ZYK.	Data were considered only up to 13_exCU.
2	TP_z16_03	Incompatible dates: TP_z16_03_33_AT_T10, TP_z16_03_33_AT_T23, TP_z16_03_33_AT_T45	Changed the dates from 13/02/2024 to 17/02/2024 to align with the other tests.
2	TP_z16_03	Initial date of 09_CU incompatible with end date of 08_ZYK	Changed the date of 09_CU from 22/03/2023 to 23/02/2023
2	TP_z16_03	Missing file TP_z16_03_14_ZYK.	Data were considered only up to 13_exCU.
2	TP_z17_01	Initial date of 09_CU incompatible with end date of 08_ZYK	Changed the date of 09_CU from 22/03/2023 to 23/02/2023
2	TP_z17_01	Missing file TP_z19_01_14_ZYK.	Data were considered only up to 13_exCU.
2	TP_z17_02	Initial date of 09_CU incompatible with end date of 08_ZYK	Changed the date of 09_CU from 22/03/2023 to 23/02/2023
2	TP_z17_02	Missing file TP_z17_02_14_ZYK.	Data were considered only up to 13_exCU.
2	TP_z17_03	Initial date of 09_CU incompatible with end date of 08_ZYK	Changed the date of 09_CU from 22/03/2023 to 23/02/2023
2	TP_z17_03	Missing file TP_z17_03_14_ZYK.	Data were considered only up to 13_exCU.
2	TP_z18_01	Initial date of 09_CU incompatible with end date of 08_ZYK	Changed the date of 09_CU from 22/03/2023 to 23/02/2023
2	TP_z18_01	From 21_CU onwards, the capacity value is incorrect.	Data used only up to 19_exCU.

Continued on next page

Table 13 – continued from previous page

Stage	TP/Serial	Identified Inconsistency	Action Taken
2	TP_z18_02	Initial date of 09_CU incompatible with end date of 08_ZYK	Changed the date of 09_CU from 22/03/2023 to 23/02/2023
2	TP_z18_02	From 21_CU onwards, the capacity value is incorrect.	Data used only up to 19_exCU.
2	TP_z18_03	Initial date of 09_CU incompatible with end date of 08_ZYK	Changed the date of 09_CU from 22/03/2023 to 23/02/2023
2	TP_z18_03	From 21_CU onwards, the capacity value is incorrect.	Data used only up to 19_exCU.
2	TP_z19_01	Incompatible dates: TP_z19_01_33_AT_T10, TP_z19_01_33_AT_T23, TP_z19_01_33_AT_T45	Changed the dates from 13/02/2024 to 17/02/2024 to align with the other tests.
2	TP_z19_01	Incorrect date for TP_z19_01_31_CU: 22.10.222.12.233	Corrected date to 19/01/2024. This date was based on the dates of TP_z19_02 and TP_z19_03, which have the same dates.
2	TP_z19_01	Initial date of 09_CU incompatible with end date of 08_ZYK	Changed the date of 09_CU from 22/03/2023 to 23/02/2023
2	TP_z19_01	Missing file TP_z19_01_14_ZYK.	Data were considered only up to 13_exCU.
2	TP_z19_02	Incompatible dates: TP_z19_02_33_AT_T10, TP_z19_02_33_AT_T23, TP_z19_02_33_AT_T45	Changed the dates from 13/02/2024 to 17/02/2024 to align with the other tests.
2	TP_z19_02	Initial date of 09_CU incompatible with end date of 08_ZYK	Changed the date of 09_CU from 22/03/2023 to 23/02/2023
2	TP_z19_02	Missing file TP_z19_02_14_ZYK.	Data were considered only up to 13_exCU.

Continued on next page

Table 13 – continued from previous page

Stage	TP/Serial	Identified Inconsistency	Action Taken
2	TP_z19_03	Incompatible dates: TP_z19_03_33_AT_T10, TP_z19_03_33_AT_T23, TP_z19_03_33_AT_T45	Changed the dates from 13/02/2024 to 17/02/2024 to align with the other tests.
2	TP_z19_03	Initial date of 09_CU incompatible with end date of 08_ZYK	Changed the date of 09_CU from 22/03/2023 to 23/02/2023
2	TP_z19_03	Missing file TP_z19_03_14_ZYK.	Data were considered only up to 13_exCU.
2	TP_z20_01	From 11_CU onwards, the capacity value is incorrect.	Data used only up to 09_CU.
2	TP_z20_02	From 07_exCU onwards, the capacity value is incorrect.	Data used only up to 05_CU.
2	TP_z20_03	From 11_CU onwards, the capacity value is incorrect.	Data used only up to 09_CU.
2	TP_z21_01	Initial date of 09_CU incompatible with end date of 08_ZYK	Changed the date of 09_CU from 22/03/2023 to 23/02/2023
2	TP_z21_01	From 21_CU onwards, the capacity value is incorrect.	Data used only up to 19_exCU.
2	TP_z21_02	Initial date of 09_CU incompatible with end date of 08_ZYK	Changed the date of 09_CU from 22/03/2023 to 23/02/2023
2	TP_z21_02	From 21_CU onwards, the capacity value is incorrect.	Data used only up to 19_exCU.
2	TP_z21_03	Initial date of 09_CU incompatible with end date of 08_ZYK	Changed the date of 09_CU from 22/03/2023 to 23/02/2023
2	TP_z21_03	From 21_CU onwards, the capacity value is incorrect.	Data used only up to 19_exCU.

Continued on next page

Table 13 – continued from previous page

Stage	TP/Serial	Identified Inconsistency	Action Taken
2	TP_z22_01	Incompatible dates: TP_z22_01_33_AT_T10, TP_z22_01_33_AT_T23, TP_z22_01_33_AT_T45	Changed the dates from 13/02/2024 to 17/02/2024 to align with the other tests.
2	TP_z22_01	Initial date of 09_CU incompatible with end date of 08_ZYK	Changed the date of 09_CU from 22/03/2023 to 23/02/2023
2	TP_z22_01	Missing file TP_z22_01_14_ZYK.	Data were considered only up to 13_exCU.
2	TP_z22_02	Incompatible dates: TP_z22_02_33_AT_T10, TP_z22_02_33_AT_T23, TP_z22_02_33_AT_T45	Changed the dates from 13/02/2024 to 17/02/2024 to align with the other tests.
2	TP_z22_02	Initial date of 09_CU incompatible with end date of 08_ZYK	Changed the date of 09_CU from 22/03/2023 to 23/02/2023
2	TP_z22_02	Missing file TP_z22_02_14_ZYK.	Data were considered only up to 13_exCU.
2	TP_z22_03	Incompatible dates: TP_z22_03_33_AT_T10, TP_z22_03_33_AT_T23, TP_z22_03_33_AT_T45	Changed the dates from 13/02/2024 to 17/02/2024 to align with the other tests.
2	TP_z22_03	Initial date of 09_CU incompatible with end date of 08_ZYK	Changed the date of 09_CU from 22/03/2023 to 23/02/2023
2	TP_z22_03	Missing file TP_z22_03_14_ZYK.	Data were considered only up to 13_exCU.
2	TP_z23_01	From 07_exCU onwards, the capacity value is incorrect.	Data used only up to 05_CU.
2	TP_z23_02	Initial date of 09_CU incompatible with end date of 08_ZYK	Changed the date of 09_CU from 22/03/2023 to 23/02/2023
2	TP_z23_02	From 09_CU onwards, the capacity value is incorrect.	Data used only up to 07_exCU.

Continued on next page

Table 13 – continued from previous page

Stage	TP/Serial	Identified Inconsistency	Action Taken
2	TP_z23_03	Initial date of 09_CU incompatible with end date of 08_ZYK	Changed the date of 09_CU from 22/03/2023 to 23/02/2023
2	TP_z23_03	From 11_CU onwards, the capacity value is incorrect.	Data used only up to 09_CU.
2	TP_z24_01	Incompatible dates: TP_z24_01_33_AT_T10, TP_z24_01_33_AT_T23, TP_z24_01_33_AT_T45	Changed the dates from 13/02/2024 to 17/02/2024 to align with the other tests.
2	TP_z24_01	Missing file TP_z24_01_14_ZYK.	Data were considered only up to 13_exCU.
2	TP_z24_02	Incompatible dates: TP_z24_02_33_AT_T10, TP_z24_02_33_AT_T23, TP_z24_02_33_AT_T45	Changed the dates from 13/02/2024 to 17/02/2024 to align with the other tests.
2	TP_z24_02	Missing file TP_z24_02_14_ZYK.	Data were considered only up to 13_exCU.
2	TP_z24_03	Incompatible dates: TP_z24_03_33_AT_T10, TP_z24_03_33_AT_T23, TP_z24_03_33_AT_T45	Changed the dates from 13/02/2024 to 17/02/2024 to align with the other tests.
2	TP_z24_03	Missing file TP_z24_03_14_ZYK.	Data were considered only up to 13_exCU.

APPENDIX B – COMPLETE TABLE OF ERROR

Table 14 provides the errors (nRMSE) obtained for each individual test point throughout the experimental stages. This detailed tabulation serves to comprehensively map the predictive accuracy of the Semi-Empirical, Hybrid GPR, and Hybrid Exponential-GPR models. The granular data reveal the exact operational points where the standard Semi-Empirical formulation struggles to capture the complex degradation behavior, while simultaneously demonstrating the enhanced robustness and consistent accuracy of the Hybrid Exponential-GPR framework across the testing matrix.

Table 14 – Complete error metrics for every individual test point.

Stage	**TP**	**Semi-Empirical**	**Hybrid GPR**	**Hybrid Exponential-GPR**
1	TP_k01	1.36%	1.39%	1.36%
1	TP_k02	0.69%	0.49%	0.60%
1	TP_k03	2.84%	0.53%	1.25%
1	TP_k04	2.79%	2.79%	2.79%
1	TP_k05	0.23%	0.19%	0.69%
1	TP_k06	0.95%	0.95%	1.56%
1	TP_k07	1.72%	1.73%	1.72%
1	TP_k08	0.86%	0.75%	1.12%
1	TP_k09	1.74%	0.98%	2.70%
1	TP_k10	3.41%	1.98%	2.58%
1	TP_k11	2.15%	1.85%	1.86%
1	TP_z01	4.26%	3.72%	1.12%
1	TP_z02	4.30%	2.77%	1.92%
1	TP_z03	8.76%	2.18%	1.65%
1	TP_z04	2.13%	1.16%	0.87%
1	TP_z05	0.65%	0.55%	0.61%
1	TP_z06	1.37%	2.31%	3.76%
1	TP_z07	1.33%	2.03%	1.28%
1	TP_z08	2.02%	1.81%	1.31%
1	TP_z09	0.69%	0.91%	1.01%

Continued on next page

Table 14 – continued from previous page

Stage	TP	Semi-Empirical	Hybrid GPR	Hybrid Exponential-GPR
1	TP_z10	8.45%	5.88%	1.51%
1	TP_z11	2.61%	0.94%	0.97%
1	TP_z12	0.63%	2.02%	0.71%
1	TP_z13	8.46%	2.15%	2.22%
1	TP_z14	1.00%	2.70%	1.02%
1	TP_z15	4.41%	5.05%	1.12%
1	TP_z16	2.04%	2.53%	1.69%
1	TP_z17	11.96%	5.45%	5.76%
1	TP_z18	30.89%	8.26%	10.10%
1	TP_z19	0.84%	2.24%	0.87%
1	TP_z20	3.21%	3.86%	3.20%
1	TP_z21	1.42%	3.06%	1.56%
1	TP_z22	6.46%	4.47%	1.17%
1	TP_z23	88.56%	6.70%	5.77%
1	TP_z24	9.86%	6.41%	3.24%
1	TP_z25	11.55%	12.35%	3.46%
2	TP_k01	0.80%	0.64%	0.67%
2	TP_k02	2.70%	0.95%	1.64%
2	TP_k03	0.87%	0.85%	0.85%
2	TP_k04	0.88%	0.77%	1.16%
2	TP_k05	0.69%	0.57%	1.02%
2	TP_k06	0.87%	0.95%	0.74%
2	TP_k07	0.60%	0.63%	0.66%
2	TP_k08	1.74%	1.63%	1.89%
2	TP_k09	0.71%	0.53%	0.53%
2	TP_k10	8.42%	1.45%	2.32%
2	TP_k11	4.19%	0.24%	0.39%
2	TP_z01	2.85%	0.61%	3.19%

Continued on next page

Table 14 – continued from previous page

Stage	TP	Semi-Empirical	Hybrid GPR	Hybrid Exponential-GPR
2	TP_z02	25.76%	2.01%	2.02%
2	TP_z03	9.91%	1.83%	1.11%
2	TP_z04	3.27%	1.09%	1.15%
2	TP_z05	0.60%	2.55%	0.77%
2	TP_z06	2.07%	1.94%	0.85%
2	TP_z07	2.14%	1.27%	1.10%
2	TP_z08	7.83%	5.12%	1.73%
2	TP_z09	1.04%	2.16%	0.64%
2	TP_z10	3.36%	2.36%	1.78%
2	TP_z11	14.03%	3.61%	2.81%
2	TP_z12	2.87%	0.83%	0.86%
2	TP_z13	1.00%	0.71%	0.67%
2	TP_z14	0.48%	0.43%	1.26%
2	TP_z15	1.05%	3.41%	3.44%
2	TP_z16	3.62%	1.55%	1.65%
2	TP_z17	6.40%	3.28%	3.36%
2	TP_z18	3.36%	0.73%	0.45%
2	TP_z19	4.14%	1.51%	1.48%
2	TP_z20	18.89%	1.03%	1.05%
2	TP_z21	3.26%	0.61%	0.52%
2	TP_z22	2.15%	0.65%	0.57%
2	TP_z23	13.98%	0.84%	0.84%
2	TP_z24	2.01%	0.51%	0.51%